EFFECTS OF SPIN ON NEUTRON-STAR OBSERVATIONS

by

Michael Bauböck

A Dissertation Submitted to the Faculty of the

DEPARTMENT OF ASTRONOMY

In Partial Fulfillment of the Requirements
For the Degree of

DOCTOR OF PHILOSOPHY

In the Graduate College

THE UNIVERSITY OF ARIZONA

2016

THE UNIVERSITY OF ARIZONA
GRADUATE COLLEGE

As members of the Dissertation Committee, we certify that we have read the dissertation prepared by Michael Bauböck entitled Effects of Spin on Neutron-Star Observations and recommend that it be accepted as fulfilling the dissertation requirement for the Degree of Doctor of Philosophy.

_____   Date: 13 May 2016
  Dimitrios Psaltis

_____   Date: 13 May 2016
  Feryal Özel

_____   Date: 13 May 2016
  Kaitlin Kratter

_____   Date: 13 May 2016
  Nathan Smith

_____   Date: 13 May 2016
  Dan Stark

Final approval and acceptance of this dissertation is contingent upon the candidate's submission of the final copies of the dissertation to the Graduate College.

I hereby certify that I have read this dissertation prepared under my direction and recommend that it be accepted as fulfilling the dissertation requirement.

_____   Date: 13 May 2016
  Dissertation Director: Dimitrios Psaltis

_____   Date: 13 May 2016
  Dissertation Director: Feryal Özel

STATEMENT BY AUTHOR

This dissertation has been submitted in partial fulfillment of requirements for an advanced degree at the University of Arizona and is deposited in the University Library to be made available to borrowers under rules of the Library.

Brief quotations from this dissertation are allowable without special permission, provided that an accurate acknowledgment of the source is made. Requests for permission for extended quotation from or reproduction of this manuscript in whole or in part may be granted by the head of the major department or the Dean of the Graduate College when in his or her judgment the proposed use of the material is in the interests of scholarship. In all other instances, however, permission must be obtained from the author.

SIGNED: Michael Bauböck

TABLE OF CONTENTS

TABLE OF CONTENTS – *Continued*

LIST OF FIGURES

LIST OF FIGURES – *Continued*

LIST OF TABLES

ABSTRACT

Measurements of neutron-star properties provide a natural way to test models of cold dense matter and theories of gravity. In order to correctly interpret these measurements, accurate models taking into account the special and general relativistic effects arising from the strong gravity and fast spin of these sources are necessary. Moreover, for some observables the effects of the rapid spin can dominate the measurement. In this thesis, I develop a ray-tracing algorithm using the Hartle-Thorne metric that allows me to determine the effects of gravity on several observables. I use this algorithm to calculate the bias introduced when observations are interpreted under the common assumption that the source is slowly spinning or not spinning at all. I show that this assumption can lead to errors in mass and radius measurements that are larger than the accuracy needed to distinguish between different models for the equation of state.

CHAPTER 1

Introduction

Neutron stars provide a window into some of the most extreme conditions in the universe. At masses of up to 2 $M_\odot$ and radii $\lesssim$ 15 km, their cores can reach densities of nearly ten times the nuclear saturation density. Moreover, the strong gravity at their surfaces and their rapid rotation cause affect measurements of emission from the stellar surface through the extreme gravitational lensing and frame dragging of the spacetime around the star. Measuring these strong gravitational effects provide a means to test general relativity, while the physical properties of the neutron stars can constrain theories of dense matter.

At their cores, neutron stars are expected to contain matter above the nuclear saturation density. The properties of matter in this regime are poorly constrained by terrestrial experiments. In particular, existing experiments can only probe nucleon interactions at or below nuclear saturation density (see Lattimer 2012) or at temperatures much higher than the Fermi energy. Moreover, extrapolating from symmetric matter found in atomic nuclei to the neutron-rich matter found in neutron star cores is highly uncertain.

Neutron stars, on the other hand, provide ideal laboratories for the study of cold dense matter. The relations between macroscopic properties of a neutron star depend on the details of the equation of state of the matter at their cores. By measuring properties such as the mass, radius, moment of inertia, quadrupole moment, or oblateness to sufficiently high precision, proposed models for the equation of state may be verified or excluded. In principle, a measurement of any two of these parameters can provide a constraint on the equation of state. In practice, the mass and radius are the most straightforward properties to measure (see, however, Raithel et al. 2016 for constraints on the equation of state from moment of inertia measurements).

1.1   Measuring Masses and Radii

Over the past forty years, great effort has been expended to accurately measure neutron-star masses and radii. These efforts have fallen into two broad categories: spectroscopic measurements of uniform emission from the stellar surface and timing measurements of pulse profiles arising from temperature anisotropies on the neutron star.

Thermal emission has been used to constrain neutron-star masses and radii in the context of thermonuclear X-ray bursts since the discovery of bursters in the 1970s (e.g., van Paradijs 1979). These bursts arise from sources that are accreting matter from a nearby main sequence or post main sequence companion. As matter accretes, hydrogen is burnt into helium, which builds up in a layer beneath the surface. When the temperature and pressure in this layer are sufficient, it undergoes a helium flash, and the entire surface of the neutron star undergoes rapid nuclear burning, resulting in X-ray emission that is sometimes greater than the local Eddington limit. This causes the photosphere of the star to expand until the photons diffusing out from the nuclear burning layer are exhausted. As the photosphere cools, it contracts back towards the stellar surface. At the moment the photosphere touches back down on the neutron star, the flux of the thermal emission is related to the mass and radius of the neutron star via the Stefan-Boltzmann law.

A similar method can be used to measure neutron-star masses and radii in sources without thermonuclear bursts. In accreting sources, the accretion itself heats the surface, causing it to emit thermal X-rays even in quiescence. Isolated neutron stars can similarly display thermal emission arising from residual heat from the star's formation. Both quiescent accreting sources (e.g., Heinke et al. 2006, 2014; Webb & Barret 2007; Guillot et al. 2013; Catuneanu et al. 2013) as well as on isolated sources (e.g., Pons et al. 2002; Drake et al. 2002) have yielded mass and radius measurements based on the flux, temperature, and distance of the source.

In addition to thermal emission, atomic features such as absorption lines, emission lines, and edges can also in principle help constrain the neutron-star mass and radius.

Light emitted from the surface of the neutron-star is redshifted as it passes through the strong gravitational field of the star on its way to a distant observer. The amount of redshift of any identifiable line measures the compactness $2GM/Rc^2$ of the neutron star. Moreover, the rapid spin of the neutron star leads to Doppler broadening of the line as different parts of the surface are moving at different velocities relative to the observer. The magnitude of this broadening is related to the spin frequency and radius of the star. As the spin frequency can often be determined independently, a measurement of the line broadening leads directly to a constraint on the neutron-star radius (Özel & Psaltis 2003).

In 2002, Cottam et al. found evidence of narrow absorption lines in the source EXO 0748-676. These observations allowed for a precise determination of the surface redshift, which, when combined with observations of thermonuclear bursts for the same source, provided tight constraints on the mass and radius (Özel 2006). However, subsequent observations failed to confirm the absorption lines (Cottam et al. 2008). Moreover, after Galloway et al. (2010) found burst oscillations in the source at 552 Hz, Lin et al. 2010 argued that the Doppler broadening expected from such a high spin frequency was inconsistent with previous observations. In Chapter 4, I offer a possible resolution to these unexpectedly narrow absorption lines.

An alternative approach to spectroscopic observations relies on timing measurements of brightness oscillations to constrain the mass and radius. These brightness oscillations are caused by a hotspot on the stellar surface going into and out of view as the star rotates. The temperature anisotropy necessary to produce a pulse profile can arise in a variety of ways. In an isolated, rotation-powered pulsar, return currents along open field lines heat the magnetic pole to a higher temperature than the rest of the stellar surface. In accreting sources, the magnetic field can also funnel accretion onto the magnetic pole, creating a local hotspot.

Finally, burst oscillations have been observed during the rise or tail of X-ray bursters. When an X-ray burst ignites on the neutron-star, nuclear burning begins in one location before it spreads across the stellar surface. The timescale for the nuclear burning to engulf the entire star is ~ 1 s, during which time only a fraction

of the surface is burning. Since this timescale is much faster than the ~ 500 Hz spin frequency observed in many burst sources, the flux from the source oscillates as the burning region is alternately hidden and in the line of sight. When the nuclear fuel is exhausted, the neutron star does not cool uniformly across its surface. The excitation of non-radial modes leads some regions of the surface to be higher in temperature than others. These temperature anisotropies again induce brightness oscillations from the source.

The waveform of all these types of brightness oscillations encodes information about the neutron star from which they originate. The usual method of extracting this information is to decompose the pulse profiles into their Fourier modes. The amplitude of the oscillation is related to the compactness of the neutron star due to strong gravitational lensing. A star with a higher compactness experiences greater self-lensing, so a smaller fraction of the surface is hidden from view for an observer. Therefore, the hotspot is visible for a larger fraction of the spin period, and the pulse amplitude is smaller. In the absence of any Doppler shifts, the pulse profile is a perfect sinusoid that encodes only the compactness. However, the Doppler boost as the hotspot moves towards or away from the observer causes the profile to differ from a sinusoid and increases the first Fourier harmonic. The magnitude of the Doppler boost depends on the surface velocity of the star, which is determined by the spin period and the radius. Therefore, measuring the Fourier harmonics of the profile can in principle provide simultaneous constraints on the mass and radius of the star.

1.2   Types and Properties of Neutron-Star Sources

To date, various constraints have been placed on neutron-star masses and radii using the methods outlined above. These measurements have been carried out on neutron stars in low-mass X-ray binaries (either during accretion episodes or during quiescence), on rotation-powered pulsars, or, in a few cases, on accretion-powered pulsars.

These three types of sources differ primarily in the energy sources of their emission. Neutron stars from low-mass X-ray binaries are accreting matter from a nearby
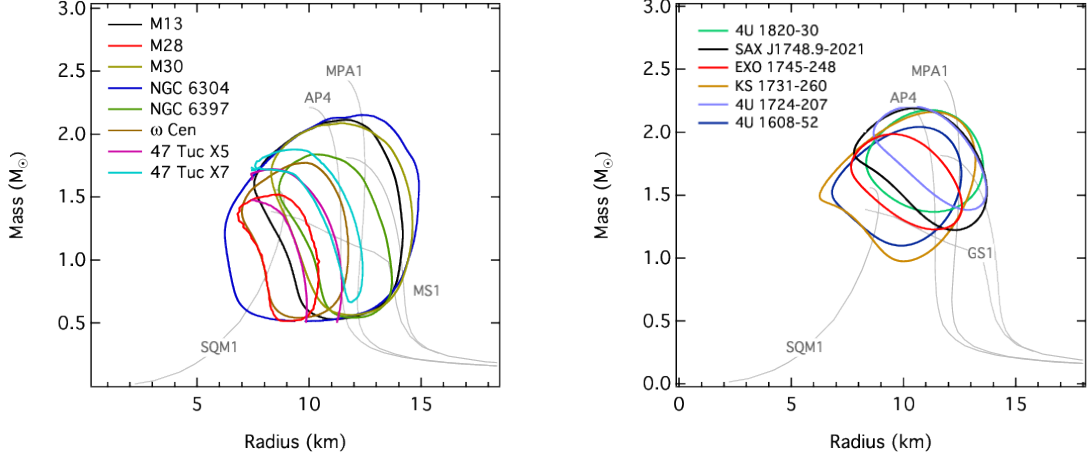
Figure 1.1: Summary of mass and radius constraints from Özel & Freire (2016). The left panel shows constraints from spectroscopic measurements of accreting sources during quiescence. The right panel shows mass and radius constraints from thermonuclear bursts. In both panels, several sample equations of state are plotted.

companion. This accretion heats the surface and causes it to emit in the X-ray. A fraction of neutron stars in low-mass X-ray binaries display X-ray bursts, in which a layer of built-up fuel fuses, further heating the surface of the star. Rotation-powered pulsars, on the other hand, are usually isolated sources whose emission is powered by their decaying spin frequency. These pulsars are primarily detected through their radio dipole emission, but in some cases return currents can sufficiently heat the magnetic pole to emit in the X-ray. Accretion powered pulsars similarly show variable X-ray emission, which is powered by the accretion flow funneled onto the magnetic pole, creating a local hotspot.

In recent years, radius constraints have been derived for bursting sources using high precision *Rossi X-ray Timing Explorer* data (e.g., Özel et al. 2009, 2010; Güver et al. 2010; Güver & Özel 2013; Steiner et al. 2010, 2013; Suleimanov et al. 2011; Poutanen et al. 2014). These studies have been able to constrain neutron star radii to a range of 8–11 km for the sources 4U 1608–52, EXO 1745–248, 4U 1820–30, and KS 1731–260. The right panel of Figure 1.1 shows constraints for these sources as well as several others.

The left panel of Figure 1.1 shows spectroscopic mass and radius constraints from

quiescent sources. In particular, Webb & Barret (2007) place upper limits of 11 km and 10.5 km on the radii of neutron stars in M13 and NGC2808, respectively. Guillot et al. (2011) find a radius of 8.3–9.8 km for the source U24 under the assumption that the neutron-star mass is 1.4 $M_\odot$. In addition, Bogdanov et al. (2016) have constrained the stellar radius for two sources in the globular cluster 47 Tuc.

To date, a handful of sources showing persistent oscillations have been analyzed to determine masses and radii. The constraints from pulse profile analysis are somewhat weaker than those from spectroscopic methods due to the correlated uncertainty between the mass and radius and several geometric parameters related to the size and location of the hotspot. Uncertainties in the radius from these measurements is typically $\gtrsim 5$ km (e.g., Poutanen & Gierlinski 2003, Bogdanov et al. 2007, Leahy et al. 2008). In addition, lower limits have been placed on the radius of several additional sources (e.g., Leahy et al. 2009, 2011; see review in Özel 2013).

All of the spectroscopic measurements discussed above have been made under the assumption that the neutron star is not spinning. This assumption simplifies the conversion between the surface area observed at spatial infinity and proper radius as measured at the stellar surface. It also neglects the changes to the emission due to Doppler shifts, frame dragging, and other consequences of the spin. For mass and radius constraints derived from pulse profiles, a slow rotation approximation is usually made under which the spacetime around the neutron star is unaffected by its spin. By setting the spacetime of the neutron star to be identical to that of a non-spinning, spherical mass, this assumption also neglects effects such as frame dragging, changes in the shape of the star, and the introduction of higher order mass multipole moments.

However, the assumption of slow spin is not appropriate for the majority of sources that have been used for mass and radius measurements. Figure 1.2 shows the distribution of spin frequencies for different types of source. As shown, a significant fraction of neutron stars have "moderate" spins above 300 Hz (in the remainder of this work, I use the term "moderate spin" to indicate a range of spin frequencies that are well below the stellar breakup frequency but nevertheless high enough to
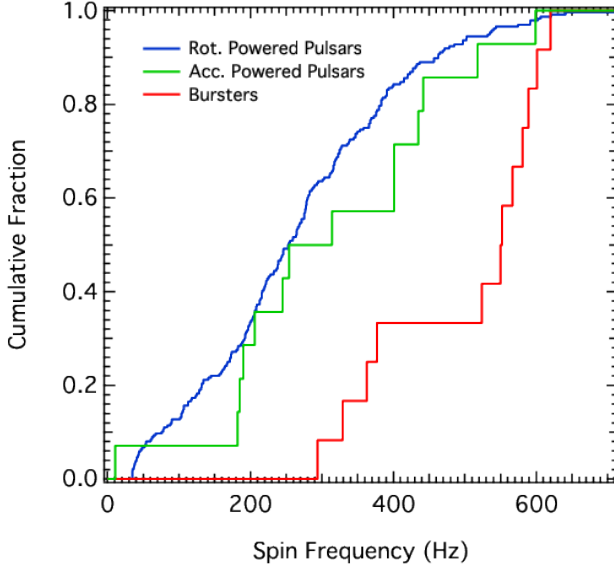
Figure 1.2: Distribution of neutron star spin frequencies for three different types of sources from Özel & Freire 2016. The blue line shows the spin frequencies of isolated, rotation-powered pulsars. The red and green lines show the distribution of spin frequencies for accreting sources, with and without thermonuclear bursts, respectively.

cause a significant change in the neutron-star spacetime). In particular, more than half of rotation-powered pulsars and nearly all X-ray bursters have such moderate spins. As I discuss below, surface geometry as well as the spacetime around such stars is significantly affected by the spin of the star, necessitating corrections to both existing and upcoming mass and radius measurements.

1.3   The *NICER* Mission

In the near future, new constraints on neutron-star masses and radii are expected from timing of rotation-powered pulsars. These sources will be the focus of an upcoming NASA Mission of Opportunity that will be located on the International Space Station. Scheduled to be launched in early 2017, the *Neutron Star Interior Composition Explorer* (*NICER*) aims to accurately measure masses and radii for at least three neutron stars. In particular, *NICER* will enable precise measurements of pulse profiles of rotationally-powered pulsars in the soft X-rays. By modeling the

waveforms of these pulses, the masses and radii of the neutron star can be measured.

The *NICER* satellite is designed to be sensitive in the energy range between 0.2 and 12 keV. This energy range coincides with the expected peak of the thermal emission from hotspots on the neutron star surface. Moreover, *NICER* will enable timing measurements to an accuracy of 300 ns, enabling temporal and spectroscopic resolution of lightcurves. Over the course of its 18 month primary mission lifetime, *NICER* is expected to collect on the order of 10^6 photons from each of three target sources showing brightness oscillations. These observations are expected to allow masses and radii to be constrained within 5% (Arzoumanian et al. 2014).

In order for *NICER* to correctly interpret measurements of pulse profiles, accurate models that take into account the properties of the neutron star are needed. Here I quantify the effects of rapid rotation on pulse profiles and other measurable quantities of neutron-stars.

1.4   Outline of this Work

In this work, I consider the effects of the neutron-star spin on observations of the mass and radius. I calculate the biases introduced in measurements when the assumption is made that the source is not spinning. I also describe several other phenomena arising from rapid rotation.

In Chapter 2, I summarize the properties of the neutron star spacetime including the effects of spin at various orders. I describe the Hartle-Thorne metric, which I use throughout the rest of this work.

In Chapter 3, I calculate the apparent surface areas of moderately-spinning neutron stars. I show that whether a spinning star appears larger or smaller than its non-rotating counterpart depends primarily on its equatorial radius. For stars with relatively small radii ($\sim$10 km), the apparent radius decreases with increasing spin. In contrast, the apparent radius for larger radii($\sim$15 km) increases with spin frequency.

In Chapter 4, I consider the effects of spin on atomic spectral features. I show that line profiles acquire cores that are much narrower than the widths expected

from pure Doppler effects for a large range of observer inclinations. I explore the causes of these unexpectedly narrow spectral features.

In Chapter 5, I describe several empirical and analytic relations between neutron-star parameters. In particular, I find a tight correlation between the compactness, spin angular momentum, and spacetime quadrupole moment of neutron stars regardless of the equation of state. I also derive an analytic expression for the ellipticity of the stellar surface.

In Chapter 6, I calculate the rotational broadening in the observed thermal spectra from the surfaces of spinning neutron stars. I show that fitting the spectra and inferring radii under the assumption that the star is not rotating causes an underestimate of the inferred radii. I calculate the inclination-averaged correction to inferred radii as a function of the stellar mass and radius and provide an empirical formula for these corrections.

Finally, in Chapter 7 I calculate the effect of spot size on neutron-star pulse profiles. Specifically, I quantify the bias introduced in radius measurements from the common assumption that hotspots on the surface are infinitesimally small. I consider the implications of these results for neutron star radius measurements with the upcoming and planned X-ray missions *NICER* and *LOFT*.

CHAPTER 2

Neutron-Star Spacetimes

The first solutions to Einstein's field equations were obtained in 1916 for non-spinning, spherically symmetric objects (Schwarzschild 1916). Soon thereafter, a solution for a spherically symmetric mass with a non-zero electric charge was found (Reissner 1916). This solution is of little astrophysical relevance, as any macroscopic charge asymmetry in an astrophysical object is expected to rapidly neutralize. Kerr (1963) found the first solution for a massive object with non-zero angular momentum. The Kerr metric is the exact solution describing the spacetime around a spinning black hole, and is a reasonable approximation for other spinning objects as long as their mass distribution is relatively spherically symmetric.

Hartle & Thorne (1968) decomposed the solution to the Einstein equations in terms of increasing multipole moments of the mass distribution. They found an exact solution at second order for an object with an arbitrary mass quadrupole moment. In recent years, solutions have been found for higher order mass multipoles (e.g. Pappas & Apostolatos 2012). In this chapter, I discuss various orders of approximations of the spacetime around a spinning neutron star. I then describe an algorithm to calculate photon trajectories through the curved spacetime from the neutron-star surface to an observer at spatial infinity.

2.1 Non-Spinning Stars

The spacetime around non-spinning, spherically symmetric stars is described exactly by the Schwarzschild metric. The line element in this metric has the form

$$ds^2 = -\left(1 - \frac{2M}{r}\right) dt^2 + \left(\frac{1}{1 - \frac{2M}{r}}\right) dr^2 + r^2 \, d\theta^2 + r^2 \sin^2\theta \, d\phi^2, \qquad (2.1)$$

where M is the neutron-star mass. Note that here and throughout this chapter I have set $G = c = 1$.

The appearance of a star in the Schwarzschild metric differs in two important respects from a star in a flat spacetime. First, light emitted from the surface of the star is lensed on its path to a distant observer. This lensing causes a larger fraction of the surface area to be visible to an observer at infinity, and consequently the apparent radius to appear larger than the physical radius R by a factor of $\left(1 - \frac{2M}{R}\right)^{-1/2}$. Secondly, photons traveling from the stellar surface is redshifted by a factor of $\sqrt{1 - \frac{2M}{R}}$. Therefore, the temperature measured by an observer at infinity is lower than the local temperature on the stellar surface.

2.2   Slowly Spinning Stars

For slowly spinning stars, a variety of approximations have been employed for their exterior spacetimes. The most commonly used of these approximations is the so-called Schwarzschild+Doppler approximation. In this formalism, the spacetime is treated to be spherically symmetric as in the Schwarzschild metric, but special relativistic Doppler terms arising from the high surface velocities are added to spectra and lightcurves calculated at infinity.

Although formally inconsistent, this approximation is extremely useful for sufficiently slowly-spinning stars as it decouples the rotation from the gravitational effects. The spherical symmetry of the spacetime allows some lensing effects to be calculated analytically and reduces the computational complexity of ray-tracing if it is necessary.

In the regime of slow rotation, the spacetime around the neutron star has also been approximated by the Kerr metric, even though this metric is not really appropriate for a neutron star, as I explain below. This metric has a line element of the

form

$$ds^2 = -\left(1 - \frac{2Mr}{\Sigma}\right) dt^2 - \left(\frac{4Mar\sin^2\theta}{\Sigma}\right) dtd\phi$$
$$+ \left(\frac{\Sigma}{\Delta}\right) dr^2 + \Sigma\, d\theta^2 + \left(r^2 + a^2 + \frac{2Ma^2r\sin^2\theta}{\Sigma}\right)\sin^2\theta\, d\phi^2, \quad (2.2)$$

with

$$\Delta \equiv r^2 - 2Mr + a^2, \tag{2.3}$$

and

$$\Sigma \equiv r^2 + a^2\cos^2\theta\ . \tag{2.4}$$

In these equations, a is the dimensionless spin parameter of the neutron star:

$$a = \frac{J}{M^2}, \tag{2.5}$$

where J is the angular momentum.

The Kerr metric is the exact solution for the metric of a rotating spherical mass distribution. It describes frame dragging, which arises from the $t\phi$ component of the metric. This effect causes an inertial observer near a spinning neutron star to corotate with the star at an angular rate equal to $g_{t\phi}/g_{tt}$. However, the Kerr metric makes an assumption about the quadrupole moment that is not entirely appropriate for neutron stars. Unlike, for example, black holes, neutron stars do not remain spherically symmetric as they increase in spin frequency. Instead, they become oblate in shape, which introduces a significant extra quadrupole mass moment. For spin periods much less than breakup, the neutron star surface remains approximately spherical and the Kerr metric is an adequate approximation of the exterior metric. For more rapidly spinning sources the Kerr metric is no longer an appropriate approximation.

2.3 Moderately Spinning Stars

For the majority of this work, I adopt a variant of the Hartle-Thorne metric (Hartle & Thorne 1968) developed by Glampedakis & Babak (2006). The Hartle-Thorne metric

is a multipole approximation of the spacetime around a neutron star truncated at second order in spin frequency. The metric includes terms up to the quadrupole mass moment, while all higher-order moments are set to zero. The Glampedakis & Babak metric I employ for this work is an expansion around the Kerr metric that allows for the quadrupole moment to be set to an appropriate value. The higher-order moments are equal to their Kerr values. To second order in spin frequency, the Hartle-Thorne and Glampedakis-Babak metrics are formally equivalent. I have opted to use this metric in order to contrast my results with those obtained when the external spacetime of a rapidly spinning neutron star is approximated by the Kerr metric.

In Boyer–Lindquist coordinates, I write the metric as a deviation from the Kerr metric:

$$g_{\mu\nu} = g_{\mu\nu}^{\mathrm{K}} + \eta a^2 h_{\mu\nu} \,, \tag{2.6}$$

where $g_{\mu\nu}$ is the metric element of the Kerr metric described by equation 2.2.

The quadrupole correction is given, in contravariant form, by

$$
\begin{aligned}
h^{tt} &= (1 - 2M/r)^{-1} \left[\left(1 - 3\cos^2\theta\right) \mathcal{F}_1(r) \right] , \\
h^{rr} &= (1 - 2M/r) \left[\left(1 - 3\cos^2\theta\right) \mathcal{F}_1(r) \right] , \\
h^{\theta\theta} &= -\frac{1}{r^2} \left[\left(1 - 3\cos^2\theta\right) \mathcal{F}_2(r) \right] , \\
h^{\phi\phi} &= -\frac{1}{r^2 \sin^2\theta} \left[\left(1 - 3\cos^2\theta\right) \mathcal{F}_2(r) \right] , \\
h^{t\phi} &= 0 \,,
\end{aligned}
\tag{2.7}
$$

with the functions $\mathcal{F}_{1,2}(r)$ shown explicitly in Appendix A of Glampedakis & Babak (2006). Note that, because it is of even order, the mass quadrupole affects only the diagonal components of the Kerr metric and not the $t\phi$-component that measures the amount of frame dragging.

2.4   Rapidly Spinning Stars

To even higher orders in spin frequency, the external spacetime of the neutron star depends on multipole moments that are of increasing order, which become important when the spin frequency exceeds ~800 Hz. These spacetimes can be calculated numerically (see, e.g., Cook et al. 1994; Stergioulas & Friedman 1995). In principle, these numerical calculations accurately describe the spacetime around a neutron star of arbitrary spin frequency.

However, these numerical spacetimes depend on the details of the equation of state. Since the primary aim of this work is to develop a framework for measurements of neutron-star properties to constrain the equation of state, it is desirable to formulate the metric in such a way that it depends only on the macroscopic properties of the neutron star. In addition, there are no known neutron star sources that spin at frequencies above 800 Hz, rendering numerical spacetimes nonessential. Therefore, for the purposes of this work, I have adopted the Hartle-Thorne metric described above rather than an exact numeric metric.

For completeness, I note that in principle the external spacetime of a rapidly spinning neutron star can also be accurately described by the analytic solution of Manko et al. (2000a, 2000b; see Berti & Stergioulas 2004; Berti et al. 2005). However, the Manko et al. (2000a, 2000b) metric does not reduce to the Schwarzschild or Kerr solutions when the angular velocity of the star is reduced toward zero (Berti & Stergioulas 2004), making it impractical for applications.

2.5   A Numerical Algorithm for Ray Tracing

In order to calculate the appearance of the neutron star at spatial infinity, I follow the method outlined in Psaltis & Johannsen (2012) to develop a ray-tracing algorithm that calculates the trajectories of photons in the neutron-star spacetime. This algorithm follows the path of a number of photons from an image plane at a great distance from the source along null geodesics back to the surface of the star.

I designate the position of the photon as the 4-vector x^μ. Then the paths of the

photons satisfy the geodesic equation,

$$\frac{d^2 x^\mu}{d\lambda^2} = -\Gamma^\mu_{\alpha\beta} \frac{dx^\alpha}{d\lambda} \frac{dx^\beta}{d\lambda}, \tag{2.8}$$

where λ is an affine parameter. Here, $\Gamma^\mu_{\alpha\beta}$ are the Christoffel symbols:

$$\Gamma^\mu_{\alpha\beta} = \frac{1}{2} g^{\mu\nu} \left(\frac{\partial g_{\nu\alpha}}{\partial x^\beta} + \frac{\partial g_{\nu\beta}}{\partial x^\alpha} - \frac{\partial g_{\alpha\beta}}{\partial x^\nu} \right), \tag{2.9}$$

where $g_{\mu\nu}$ and $g^{\mu\nu}$ are the covariant and contravariant forms of the metric, respectively.

The t and ϕ symmetries of the metric lead to the definition of two Killing vectors $\xi = (1, 0, 0, 0)$ and $\eta = (0, 0, 0, 1)$. These two Killing symmetries are equivalent to the conservation of energy and angular moment, respectively:

$$E = -g_{tt} \frac{dt}{d\lambda} - g_{t\phi} \frac{d\phi}{d\lambda} \tag{2.10}$$

and

$$L = g_{\phi\phi} \frac{d\phi}{d\lambda} + g_{t\phi} \frac{dt}{d\lambda}. \tag{2.11}$$

Following the notation of Johannsen & Psaltis (2012), I define λ' as $E\lambda$ and the impact parameter b as L/E. I can then write two first-order differential equations for the t and ϕ components of the photon trajectory:

$$\frac{dt}{d\lambda'} = \frac{-g_{\phi\phi} - b g_{t\phi}}{g_{\phi\phi} g_{tt} - g_{t\phi}^2} \tag{2.12}$$

and

$$\frac{d\phi}{d\lambda'} = \frac{b \left(g_{tt} + g_{t\phi} \right)}{g_{\phi\phi} g_{tt} - g_{t\phi}^2} \tag{2.13}$$

Using equation 2.8 for the r and θ components of the photon position and equations 2.12 and 2.13 for the t and ϕ components, respectively, I can now solve for the photon trajectory from the image plane to the surface of the star. I solve these equations numerically using a fourth-order Runge-Kutta algorithm until the photon

either intersects the surface of the star or exceeds the distance of the star by 10%, at which point I assume that it has bypassed the star entirely. In order to check the accuracy of the numerical integration, I use the additional constraint that the photon trajectories should be null geodesics, i.e.

$$g_{\mu\nu} \frac{dx^\mu}{d\lambda} \frac{dx^\nu}{d\lambda} = 0. \tag{2.14}$$

I calculate the deviation from this relation along the photon path as a proxy for the accumulated integration error.

Because the surface of the neutron star deviates from spherical symmetry at high spin frequencies (see section 3.2) and photons may intersect the surface at oblique angles, special care must be taken when evaluating the coordinates at which the photon geodesics intersect the stellar surface. I use a simple procedure to determine the spherical coordinates of intersection: once a step in the Runge–Kutta algorithm crosses over the surface of the star, I perform a linear interpolation between the last two points on the geodesic. I then employ a bisection algorithm to find the point of intersection between that interpolation and the functional form of the stellar surface.

Following Cadeau et al. (2007), I calculate the beaming angle for a photon emitted at the surface of the neutron star as

$$\cos \alpha_e = \frac{\sqrt{g^{rr}}}{1+z} \frac{k^r - k^\theta R'(\theta)}{\sqrt{1 + [\frac{R'(\theta)}{R(\theta)}]^2}} \tag{2.15}$$

where k^r and k^θ are the components of the photon's momentum at the point of intersection with the stellar surface, $R(\theta)$ is the functional form of the surface of the neutron star (Equation (3.2)), and z is the total redshift.

CHAPTER 3

Images of Moderately Spinning Neutron Stars

3.1   Apparent Surface Areas

Converting a measurement of the apparent surface area of a neutron star to a radius requires correcting for a number of general-relativistic effects. As the photons propagate in the strong gravitational fields of neutron stars, their energies are redshifted while their trajectories experience strong lensing. For a non-spinning neutron star, both effects depend only on the tt-component of its exterior metric and can be analytically corrected for in any metric theory of gravity (Psaltis 2008). The situation, however, becomes increasingly complicated as the angular velocity of the neutron star increases toward the point of breakup.

Various effects of increasing the angular velocity of a neutron star have been studied in the context of predicting the orbits of test particles (e.g., Shibata & Sasaki 1998; Abramowicz et al. 2003; Berti & Stergioulas 2004; Berti et al. 2005), the lightcurves that arise when the surface emission on a spinning neutron star is not uniform (Miller & Lamb 1998; Braje et al. 2000; Muno et al. 2003; Poutanen & Gierlinski 2003; Cadeau et al. 2005, 2007; Morsink et al. 2007), as well as the rotational broadening of atomic lines that originate on the stellar surfaces (Özel & Psaltis 2003; Bhattacharyya et al. 2006; Chang et al. 2006). There are two conclusions that emerged from these studies and are relevant for this work: (1) that the Hartle-Thorne metric provides an approximation to the external spacetime of a rotating neutron star that is adequate for most astrophysical applications (Berti et al. 2005) and (2) that taking into account the oblateness of the stellar surface is at least as important as considering the effects of frame dragging around a spinning neutron star (Morsink et al. 2007).

In this chapter, I calculate numerically the apparent geometric surface area of

a rotating neutron star using a variant of the Hartle–Thorne metric developed by Glampedakis & Babak (2006). I use a new, fast ray-tracing algorithm that takes into account the oblateness of the neutron star as well as deviations from the Schwarzschild metric for its external spacetime that are formally correct up to the contributions of the quadrupole mass moment. With this analytic metric I can calculate the apparent surface area of a neutron star in a way that depends only on global properties of the star and not on the details of an assumed equation of state. Indeed, as I will show, the apparent surface area depends on six parameters: the equatorial and polar radii of the neutron star, its mass, spin angular momentum, and quadrupole mass moment, as well as the observer's inclination. Using the approximate relation between the polar and equatorial radii of spinning neutron stars obtained by Morsink et al. (2007) reduces the number of parameters to five.

I find that the apparent surface area of the neutron star changes only marginally over the range of spin frequencies of known sources. The corrections to the observed surface area only become significant at rotational frequencies greater than 1000 Hz.

3.2   Quadrupole Moment and Oblateness

For a compact object with mass M and specific angular momentum a, I write the mass quadrupole moment of the spacetime as

$$q = -a^2(1 + \eta) \,, \tag{3.1}$$

so that, when $\eta = 0$, this reduces to the quadrupole moment of the Kerr metric. (Note that, in the formalism of Glampedakis & Babak 2006, $\epsilon = \eta a^2$.) This mass moment of the spacetime for a rapidly spinning neutron star depends on its density profile and hence on the underlying equation of state.

Laarakkers & Poisson (1999) calculated neutron-star quadrupole moments for a wide range of equations of state, using a numerical algorithm that solves the Einstein field equations with no approximations. They found that Equation (3.1) remains valid even for neutron stars that are spinning near their breakup points. They

calculated $\eta \sim 1-6$, depending on the stellar mass and radius. Berti & Stergioulas (2004) further computed the quadrupole moments of stars in the Hartle–Thorne approximation and compared them to those of the numerical spacetimes. They concluded that the Hartle–Thorne approximation is adequate for all astrophysical applications. This approximation is expected to be valid for observed neutron stars because the fastest known X-ray burster is spinning at 620 Hz (4U 1608-52; Galloway et al. 2008), and the fastest known pulsar is spinning at 716 Hz (Hessels et al. 2006), which are expected to be significantly smaller than their breakup frequencies. Figure 3.1 shows the dependence of the quadrupole moment q on the spin frequency for a 1.8 $M_\odot$ star with the appropriate value of the parameter η taken from Laarakkers & Poisson (1999) for two different equations of state.

In order to calculate the apparent surface area of a neutron star using the above spacetime, I need to allow for the stellar surface to be non-spherical. This is required by the fact that the deviations of both the external spacetime from the Kerr metric as well as of the shape of the stellar surface from spherical symmetry are of second order in f_s/f_0. Moreover, Morsink et al. (2007) have shown that, for purely geometric reasons, the changes in the predicted lightcurves of spinning neutron stars when the non-spherical shapes of their surfaces are taken into account are at least as important as the effects of frame dragging that are formally only of first order in f_s/f_0.

Morsink et al. (2007) fit a large number of neutron-star shapes calculated for a wide range of equations of state. They show that an equation of the form

$$\frac{R(\theta)}{R_{\rm eq}} = 1 + \sum_{n=0}^{N} a_{2n} P_{2n}(\cos\theta), \tag{3.2}$$

with $R_{\rm eq}$ the equatorial radius of the star and $P_{2n}(\cos\theta)$ the Legendre polynomial of order $2n$, accurately describes the shape of the neutron-star surface for even the fastest spinning stars if the series is terminated at $N = 2$. For all equations of state the coefficients of the expansion depend only on two parameters,

$$\zeta \equiv \frac{GM}{R_{\rm eq}c^2} \tag{3.3}$$

and

$$\epsilon \equiv \frac{(f_{\mathrm{s}}/2\pi)^2 R_{\mathrm{eq}}^2}{c^2 \zeta} \ . \tag{3.4}$$

Excluding those equations of state that describe self-bound strange stars, Morsink et al. (2007) obtain for the coefficients in Equation (3.2) the following empirical relations:

$$
\begin{aligned}
a_0 &= -0.18\epsilon + 0.23\zeta\epsilon - 0.05\epsilon^2 \\
a_2 &= -0.39\epsilon + 0.29\zeta\epsilon + 0.13\epsilon^2 \\
a_4 &= 0.04\epsilon - 0.15\zeta\epsilon + 0.07\epsilon^2 \ .
\end{aligned}
\tag{3.5}
$$

Figure 3.2 shows the ratio of the polar to the equatorial radius of a neutron star, as calculated with the above fitting formula.

In the Hartle–Thorne approximation, only terms up to second order are considered, i.e., the above series is terminated at $N = 1$. In this case, I can rewrite the shape of the stellar surface in terms only of the equatorial and polar radii as

$$\frac{R(\theta)}{R_{\mathrm{eq}}} = \sin^2\theta + \frac{R_{\mathrm{p}}}{R_{\mathrm{eq}}}\cos^2\theta \ . \tag{3.6}$$

This introduces the two additional parameters, R_{p} and R_{eq}, which will determine the apparent surface area of the neutron star. In Figure 3.2, I show the deformation of neutron stars for both the full fitting formula (solid lines) and the approximation up to quadrupole order (dashed lines). Over the entire region of interest, the agreement between the approximation and the exact formula is within 5%. Therefore disregarding higher order mass moment terms when calculating the shape of the neutron star is justified.

The last free parameter in my simulation is the inclination angle of the observer. Since there is no spherical symmetry, the apparent surface area of the neutron star will depend on the angle at which it is viewed. I define this angle, θ_0, as the angle between the rotation axis of the star and the line of sight to an observer at infinity.

3.3   Geometric Surface Areas of Neutron Stars

One way of inferring the apparent surface area of the neutron star, in principle, is by direct angular measurement of the stellar image. If the distance of the star is known, it is straightforward to calculate its physical radius given its angular dimension. Another method to infer the surface area is by means of its thermal spectrum. By measuring the temperature of the star and its total flux, one can again derive its surface area. For slowly spinning neutron stars, these two measurements agree.

In the absence of rotation, the spacetime around the star is described by the Schwarzschild metric. An observer at infinity will observe the star to be enlarged due to gravitational self-lensing. The angular apparent surface area of the star is then given by

$$\frac{A_{\mathrm{Sch}}^{G}}{A} = (1 - \frac{2GM}{Rc^2})^{-1} , \tag{3.7}$$

where $A = \pi R^2$. The spectroscopic area, on the other hand, is defined as

$$A_{\mathrm{Sch}}^{S} = \frac{F_\infty}{\sigma T_{\mathrm{eff},\infty}^4}, \tag{3.8}$$

where F_∞ is the thermal flux and $T_{\mathrm{eff},\infty}$ is its effective temperature. Gravitational redshift reduces both the observed flux and the effective temperature as

$$F_\infty = (1 - \frac{2GM}{Rc^2})F_{\mathrm{NS}},$$

$$T_\infty = \sqrt{1 - \frac{2GM}{Rc^2}}T_{\mathrm{NS}}, \tag{3.9}$$

where F_{NS} and T_{NS} are the flux and temperature measured at the surface of the neutron star. Combining Equations (3.8) and (3.9) I find that the apparent spectroscopic surface area at infinity is given by

$$\frac{A_{\mathrm{Sch}}^{S}}{A} = 4(1 - \frac{2GM}{Rc^2})^{-1}. \tag{3.10}$$

Clearly, for a slowly spinning neutron star

$$\frac{A_{\text{Sch}}^{S}}{A_{\text{Sch}}^{G}} = 4.$$

(3.11)

The factor of four arises from the difference between the total surface area $(4\pi R^2)$ measured spectroscopically and the projected surface area (πR^2) measured geometrically. For a moderately spinning neutron star, the lack of spherical symmetry in the metric, the oblateness of the star, and the second order terms in the Doppler shift will introduce different corrections to the geometric and spectroscopic areas as measured at infinity. As a result, these two measurements will not agree in general.

In practice, only the spectroscopic area can be measured, as neutron stars are too small to allow for a direct measurement of their angular sizes. However, the change in apparent angular size of a neutron star plays a role even in the measurement of its spectroscopic surface area. In the following, I use a ray-tracing algorithm to investigate the effect of rapid rotation on the geometric surface areas of neutron stars. I will discuss the additional effects of position-dependent redshift and Doppler shifts in Chapter 4.

Table 3.1: Neutron-Star Parameters

| Configuration | M | R_{eq} | I | η |
	$(M_\odot)$	(km)	(10^{45}g cm^2)	
1	1.8	10	1.4	1.2
2	1.8	15	3.0	3.9

Parameters of interest for the two neutron star configurations used in this chapter: the mass M, the equatorial radius R_{eq}, the moment of inertia I, and the deviation from the Kerr quadrupole η.

I calculate the apparent geometric surface area of a neutron star by counting directly the number of rays originating at the image plane that intersect the surface

of the star. The area on the image plane covered by the intersecting rays corresponds to the angular area of the image of the neutron star. Moreover, the coordinates on the neutron star at which each ray intersects the surface allow me to construct a contour plot of the apparent image of the star to an observer at infinity (see Figure 3.3).

For my models, I used two different configurations of neutron-star parameters, hereafter labeled "Configuration 1" and "Configuration 2". In each case, I chose the mass, equatorial radius, moment of inertia (from Cook et al. 1994), and quadrupole deviation η (according to Laarakkers & Poisson 1999) corresponding to a proposed equation of state in the non-spinning case. In order to demonstrate the range of the change in surface area, I chose a relatively soft equation of state (EOS FPS) for Configuration 1, and a relatively stiff equation of state (EOS L) for Configuration 2. I then held these parameters constant and varied only the spin frequency of the neutron star. Therefore, as the spin of each star increases, its parameters will increasingly deviate from the values predicted by the initial equations of state. While the resulting models do not reflect the predictions of any particular equation of state, they allow me to separate the various physical effects and estimate the magnitude of the change in surface area across the parameter space. The parameters of both configurations are summarized in Table 3.1.

Figure 3.3 illustrates the appearance of the two neutron stars in both the Schwarzschild approximation and at a high spin frequency. Three effects influence the apparent image in the rapidly spinning case: frame dragging, the non-zero quadrupole moment, and the oblateness of the stellar surface. The change in the apparent image of the star due to each of these effects is illustrated in Figure 3.4. Frame dragging causes the image of the neutron star to be displaced horizontally while preserving its circular appearance. The negative quadrupole moment causes the image to stretch horizontally about the axis of rotation. Finally, the oblateness of the stellar surface squeezes the poles together, further emphasizing the elongated appearance of the star. The combination of the displacement due to frame dragging and the stretching due to the quadrupole moment give rise to the asymmetric shape of the stellar image. A similar effect has been reported for images of accretion flows

around black holes (Johannsen & Psaltis 2010).

Figure 3.5 shows the contributions of each of these effects to the geometric surface area of the neutron star as a function of spin frequency. Note that the Hartle–Thorne approximation to the metric formally becomes inaccurate at the highest spin frequencies shown in this figure. The dominant effect on the image of a neutron star with a Kerr metric is due to frame dragging. However, as discussed above, frame dragging merely displaces the image of the star without altering its area. Therefore, the apparent area under the Kerr metric stays nearly constant (the small increase at high spin frequencies is due to the non-zero Kerr quadrupole). Including the extra quadrupole moment described by Equation (3.1) increases the surface area more significantly at faster spins. The oblateness of the stellar surface tends to counteract these effects and decrease the apparent surface area. Whether the surface area increases or decreases with higher spin frequency depends on which of these corrections dominate.

Comparing the left and right panels of Figure 3.5, it is clear that the relative importance of the oblate shape of the star grows as its equatorial radius increases. Figure 3.5 shows that the radius of a star described by Configuration 2 falls within the regime where the oblateness dominates the correction to the apparent surface area. In this case, the observed surface area of the star primarily decreases with increasing spin frequency, and the quadrupole moment only adds a small correction at the highest spin frequencies. At a radius of 10 km, however, as in Configuration 1, the effect of the quadrupole moment outweighs the oblateness for spin frequencies up to 1200 Hz, resulting in an overall increase of apparent surface area.

Since the presence of a spin axis breaks the symmetry of the spacetime, the image of the neutron star also depends on the inclination at which it is viewed. Figure 3.6 shows this dependence for the two neutron stars with different radii. Again, the direction of the trend depends on which of the effects is dominant. For the neutron star with a larger radius (left panel), increasing the spin invariably leads to a smaller observed surface area and a weak dependence on inclination. For the neutron star with a smaller radius, however, the effects due to the oblateness and the quadrupole

moment are comparable in magnitude (right panel). In this case, the direction of the effect depends more strongly on inclination: the star appears to grow in area with increasing spin frequency at large inclination, while it shrinks when viewed near the poles.

The change in surface area with inclination is due to the non-spherical shape of the neutron star and the θ-dependence of the metric. I investigate the behavior of these two contributions further in Figure 3.7, where I show the contributions of geometry and light-bending to this change in area for a fixed spin frequency for the Configuration 2 neutron star.

The curve labeled "Geometry" shows the dependence of the apparent surface area of the neutron star on inclination in the absence of any relativistic effects (see Appendix A for the details of the calculation). As expected, changing the inclination from pole-on to edge-on decreases the surface area of the image. On the other hand, the curve labeled "Total" shows the change of the surface area with inclination when relativistic effects are taken into account. I also plot the ratio of the two dependences as the curve labeled "Gravity." As the poles of the oblate spheroid lie deeper in the gravitational well than the equator, the effect of light-bending is stronger when the star is seen at a higher inclination. These two effects cancel to within 10%, leaving the apparent surface area of the star practically constant over changing inclination.

3.4 Conclusions

A spinning neutron star introduces several effects in surface area measurements beyond those of the stationary Schwarzschild metric. Rapid rotation causes the neutron star to acquire a quadrupole moment and an oblate surface. Both of these effects distort the image of the star as seen by distant observers, introducing a correction to the calculation of neutron star radii from a measurement of their surface areas.

The relative contributions of the quadrupole moment compared to the oblateness depend strongly on the radius of the star. At a radius of 15 km, the quadrupole contribution is negligible when compared to the change in apparent area caused by the deformation of the stellar surface at all spin frequencies. At a radius of

10 km, which are consistent with current observations (Özel et al. 2010; Steiner et al. 2010), the self-lensing dominates over the oblateness for spin frequencies less than ~ 1000 Hz.

While the apparent surface area does depend on the oblateness and quadrupole moment caused by the neutron-star spin, these corrections are small for the spin frequencies that have been observed to date. Only at frequencies above ~ 800 Hz does the apparent surface area change significantly. For the observed range of spin frequencies, the change in apparent geometric surface area is less than 10%, for both configurations considered here and at all inclinations.

Studies of the spectroscopic determination of surface areas for thermally emitting neutron stars have so far relied on the Schwarzschild approximation, which neglects the correction due to the changes in spin and oblateness of the neutron star due to the stellar rotation (e.g., Rutledge et al. 2001; Özel 2006; Heinke et al. 2006; Webb & Barret 2007; Özel et al. 2009; Güver et al. 2010a, 2010b). Observational uncertainties inherent in these measurements are currently at the $\sim 10\%$ level and hence larger than the effects presented here. I will discuss the additional corrections in the spectroscopic measurements of spinning neutron stars in Chapter 4. As the uncertainties in the data shrink with future observations, it will be necessary to take into account the corrections due to neutron star spins.
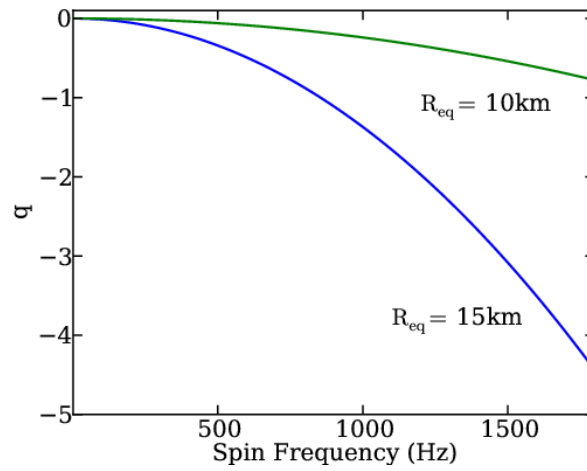
Figure 3.1: Mass quadrupole moment of the spacetime as a function of the spin frequency of the neutron star for two different radii. For each configuration, I show the quadrupole moment for a star of mass 1.8 $M_\odot$, with a radius of 10 km and 15 km, and the remaining parameters chosen to correspond to models with EOS FPS and EOS L, respectively (Cook et al. 1994).
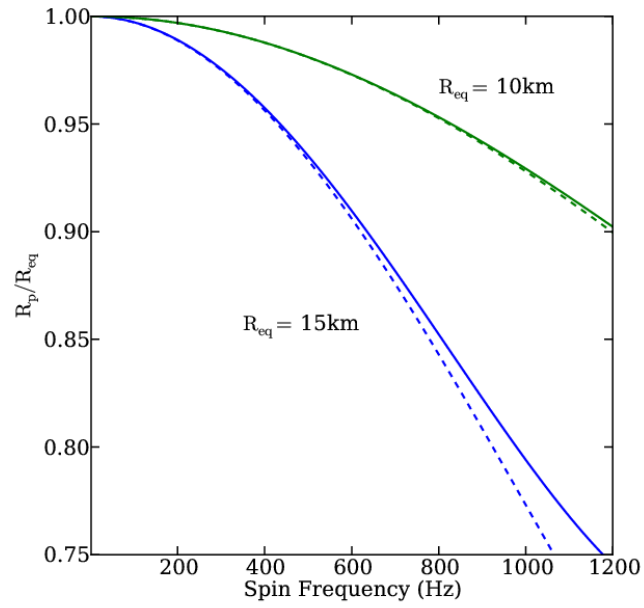
Figure 3.2: Ratio of the polar to the equatorial radius of a neutron star as a function of its spin frequency, calculated using the approximate relation of Morsink et al. (2007). The two pairs of curves correspond to two different stars with the same mass of 1.8 $M_\odot$ and different radii. In each case, the solid curve is the result of the complete fitting formula (3.2), whereas the dashed curve is the result when only the terms up to the quadrupole order are used.
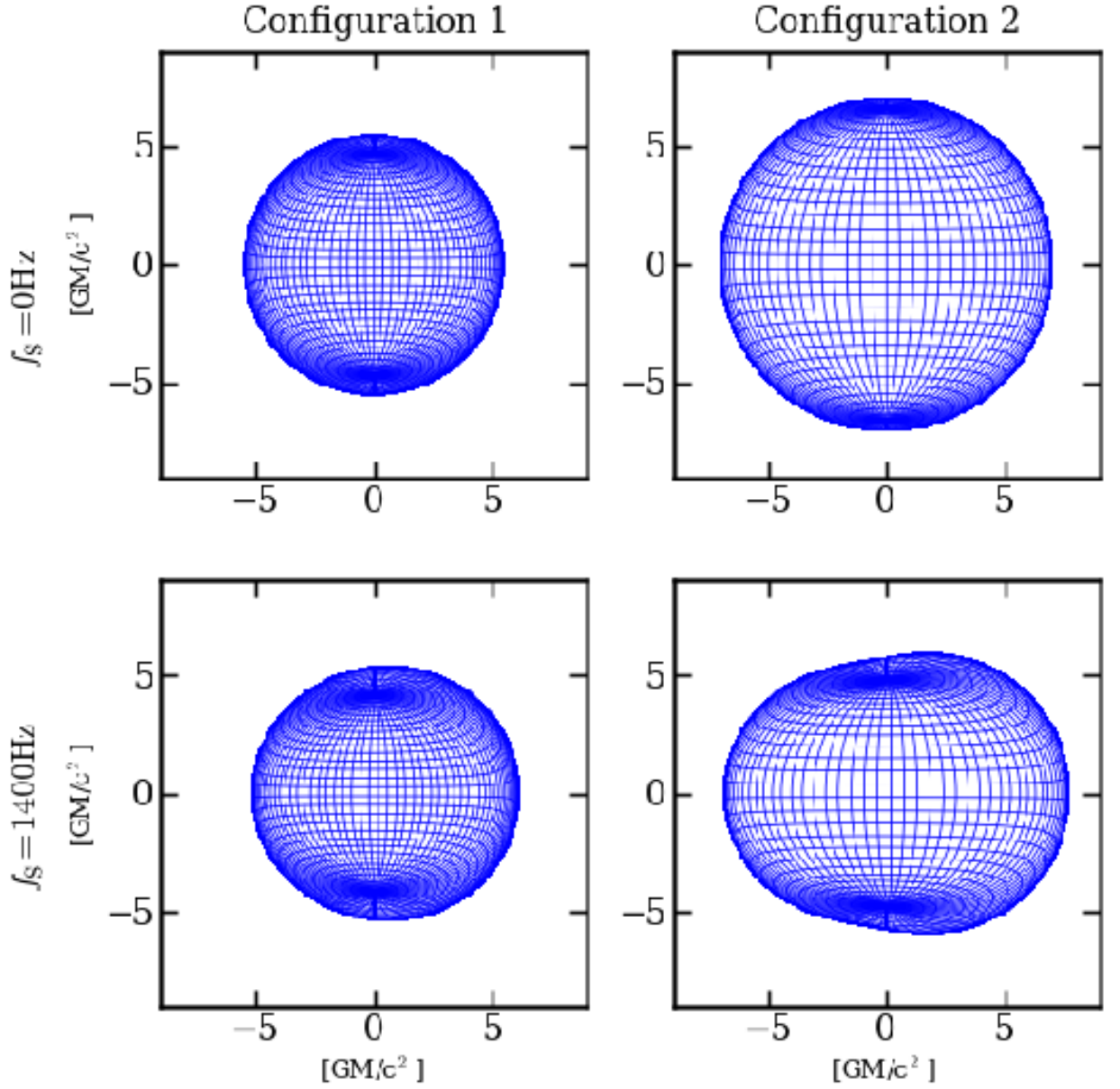
Figure 3.3: Apparent image of neutron stars at infinity calculated for different configurations. Two stars with $R_{eq} = 15$ km (left panels) and $R_{eq} = 10$ km (right panels) are shown, one non-spinning (upper panels) and one with a spin frequency of 1400 Hz (lower panels). In both cases, the observer is in the plane of the equator ($\theta_0 = \frac{\pi}{2}$), and the star rotates counterclockwise, the left side approaching the observer and the right side receding.
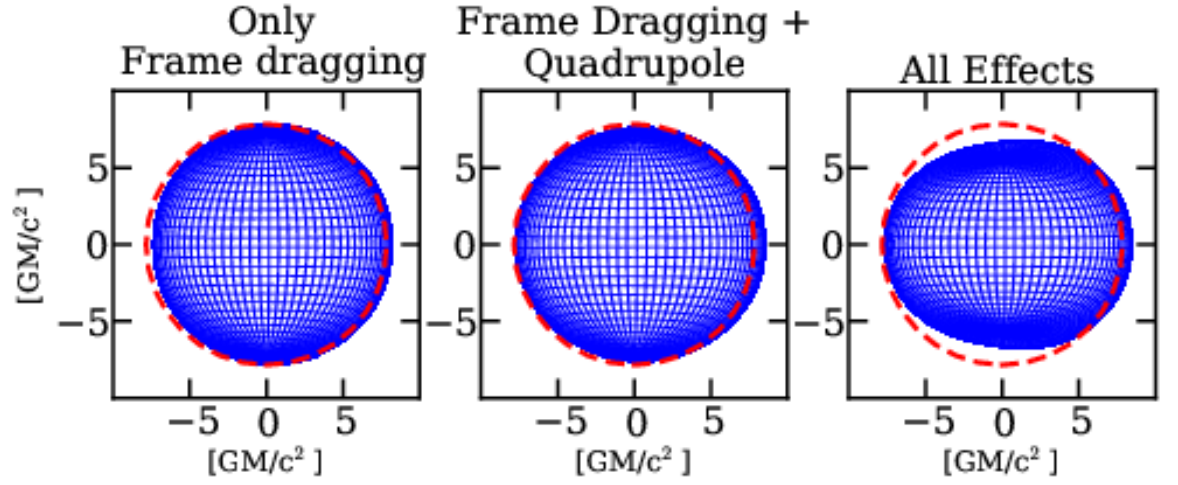
Figure 3.4: Effect of frame dragging, quadrupole moment, and oblateness on the image of a neutron star. The left panel shows the image of a star in a Kerr metric with $q = 0$, where the only effect on the appearance of the star is the displacement of the image due to frame dragging. The center panel shows the star in a Kerr metric with an extra quadrupole moment as described in Equation (3.1), which causes the image to stretch horizontally. The right panel includes both an extra quadrupole and an oblate stellar surface, causing the poles to squeeze together. The mass, radius, and moment of inertia for each star are chosen according to Configuration 2, as is the quadrupole moment for all but the Kerr case. In each case the star is rotating at 1000 Hz. The red dashed circle in each panel indicates the location and size of the image in the Schwarzschild metric.
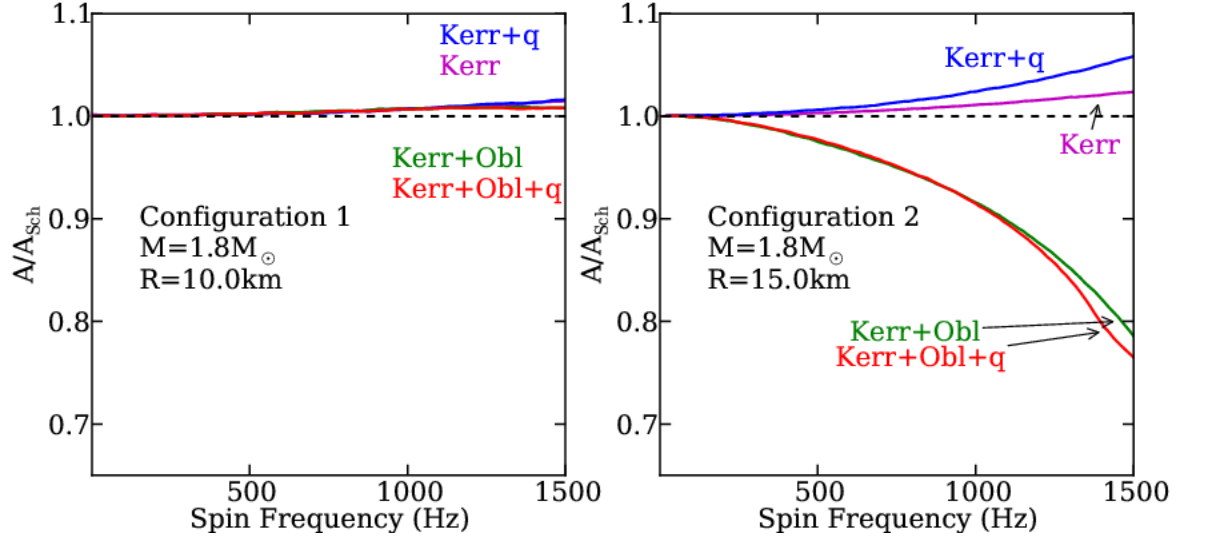
Figure 3.5: Ratio of the apparent surface area of a rotating neutron star to the area of a static neutron star as a function of spin frequency. Two stars are shown, corresponding to Configuration 1 (left panel) and Configuration 2 (right panel) as described in the text. In both plots, the four lines show different approximations of the metric outside the star: the Kerr metric, the Kerr metric plus a quadrupole deviation, the Kerr metric with an oblate stellar surface, and the Kerr metric with both a quadrupole deviation and oblateness. The dashed line is at $A/A_{\mathrm{Sch}} = 1$. In this plot, the inclination of the star is set to $90°$. Note that the plot is extended past the mass shed limit in some configurations in order to show the general trend of the relationship.
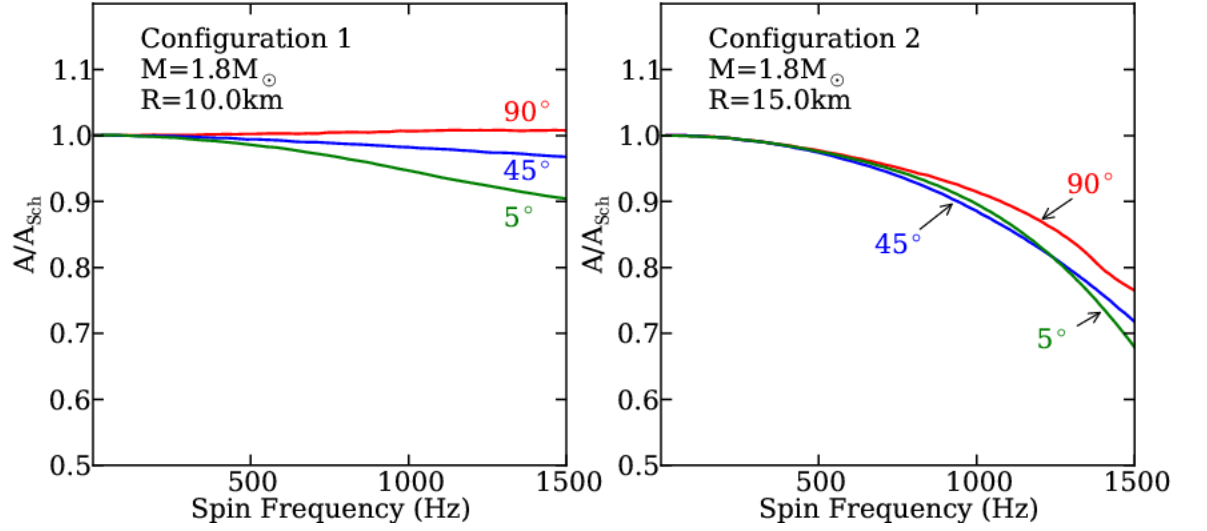
Figure 3.6: As in Figure 3.5 but showing the apparent radius for three different inclinations, taking into account both the quadrupole moment and the oblateness of the star. The left panel corresponds to Configuration 1, while the right panel corresponds to Configuration 2. Again, the x-axis is extended past the mass-shed limit in some cases.
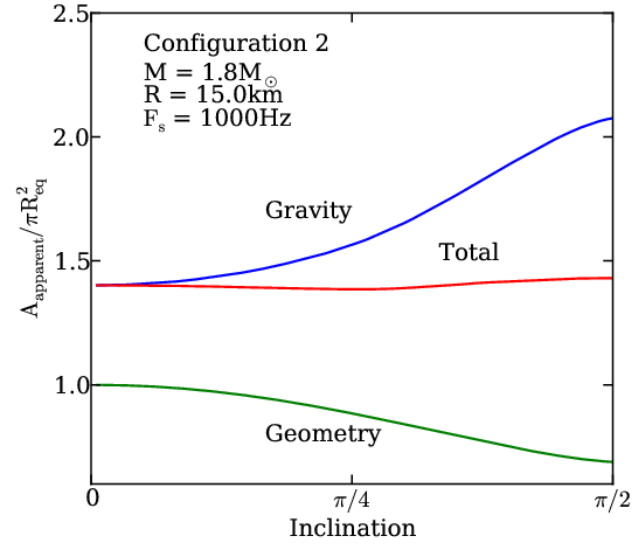
Figure 3.7: Relative contributions of geometry and gravitational light bending to the total surface area as a function of inclination. The green line, marked "Geometry," shows the apparent surface area normalized to πR_{eq}^2 in a flat spacetime (see Appendix A). The red line, labeled "Total," shows the area calculated by ray tracing in the Hartle–Thorne metric. The ratio of these two areas shows the effect of gravitational light-bending as a function of inclination, plotted in the blue line labeled "Gravity".

CHAPTER 4

Narrow Atomic Features from Rapidly Spinning Neutron Stars

4.1 Atomic Features

In addition to corrections in the observed surface area, the neutron star spin also changes the properties of emission from its surface. The combination of Doppler shifts and gravitational redshifts dictate the detailed profile and overall redshift of atomic features emitted at the stellar surface. Previous works have modeled the rotational broadening of spectral features by approximating the spacetime with the Schwarzschild metric and adding Doppler shifts due to the motion of the surface (e.g., Miller & Lamb 1998; Muno et al. 2002; Poutanen & Beloborodov 2006). In this approximation, the rotational broadening of spectral features is largely due to the Doppler shift and is approximately proportional to the neutron star radius (Özel & Psaltis 2003; Chang et al. 2006).

At more rapid spins, however, the Schwarzschild metric is no longer an appropriate approximation for the spacetime. In the Kerr metric, the additional effect of framedragging has a negligible effect on line profiles for the range of spins expected from astrophysical sources (Bhattacharyya et al. 2006). In the Hartle-Thorne metric, the neutron star is allowed to become oblate in shape and acquire an additional quadrupole moment. In this case, line profiles can further differ from the Schwarzschild+Doppler approximation.

In this chapter, I calculate the profiles of atomic features from neutron-star surfaces in the Hartle-Thorne approximation (Bauböck et al. 2012). This approach allows me to describe the external spacetimes of rotating neutron stars using only a few of their macroscopic properties, such as their masses, radii, angular momenta, and quadrupole moments, without a detailed knowledge of the equation of state; naturally, these properties can be calculated for any given equation of state. I

find that taking into account the quadrupole moment of the neutron-star space-time leads to atomic features that are qualitatively different than those calculated in the Schwarzschild+Doppler approximation. Indeed, atomic features with very narrow cores may originate on the surfaces of even moderately spinning neutron stars when viewed at inclinations at which pure Doppler effects would predict significantly broader features.

4.2   Line Profiles

Figure 4.1 shows the profiles of atomic features emitted from the surface of a neutron star with a radius of 10 km and a mass of 1.4 $M_\odot$, for different spin frequencies and observer inclinations. For each simulated profile, I normalize the line so that the bolometric luminosity is equal to unity.

In the absence of rotation, the only effect the geometry of the star has on the line profile is to shift its observed energy by the gravitational redshift at the stellar surface. In the case of a 1.4 $M_\odot$ star with a radius of 10 km, the energy of the line center is redshifted by a factor of 0.77.

The first order effect of rotation on the line profile is the broadening associated with the Doppler shift between the approaching and receding edges of the star. At low spin frequencies, the width of the line is determined almost entirely by this effect. A slight asymmetry appears in the profile that is due to the second order effect of relativistic beaming—the photons emitted on the blueshifted portion of the star are beamed toward the observer, shifting the peak of the observed spectrum to the right as shown in Figure 4.1. The profiles corresponding to high observer inclinations closely match the results of, e.g., Özel & Psaltis (2003), in which only first-order Doppler shift corrections were considered.

At low inclinations and more moderate spins, I find a significant deviation from the line profile predicted by the Schwarzschild + Doppler broadening. In that simplified approach, the width of the line is determined by the line-of-sight velocity of the neutron star surface and scales with the sine of the inclination to the observer. I find, however, that neutron stars with relatively rapid rotations (such that their
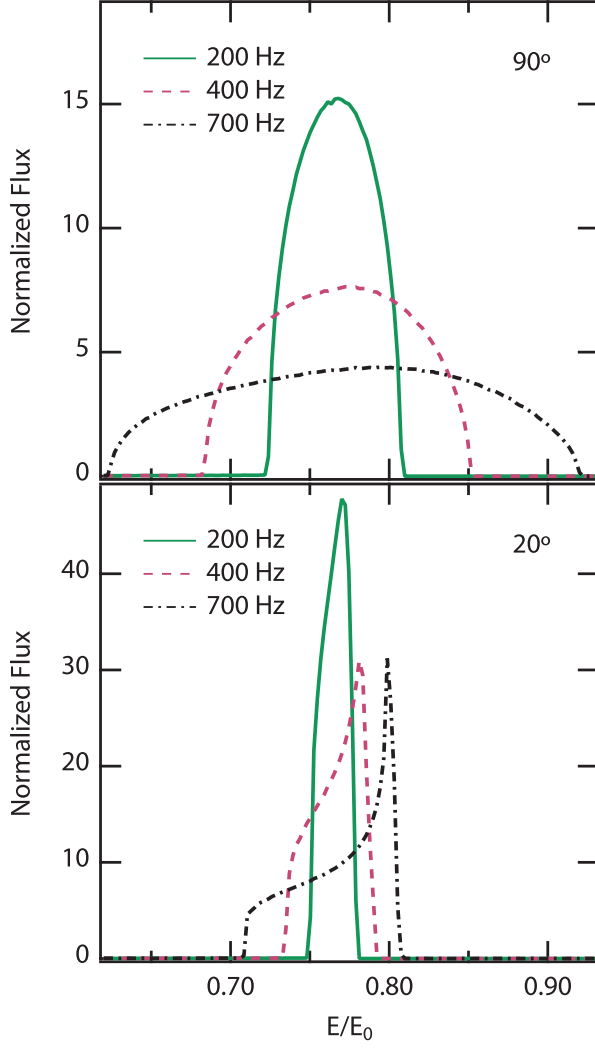
Figure 4.1: Line profiles for neutron stars spinning at three different rotational frequencies. In each case, the star has a radius of 10 km, a mass of 1.4 $M_\odot$, and an inclination of (top) 90° and (bottom) 20° to the observer. As the spin frequency increases, the lines become broader. At low observer inclinations, the lines also develop narrow cores.
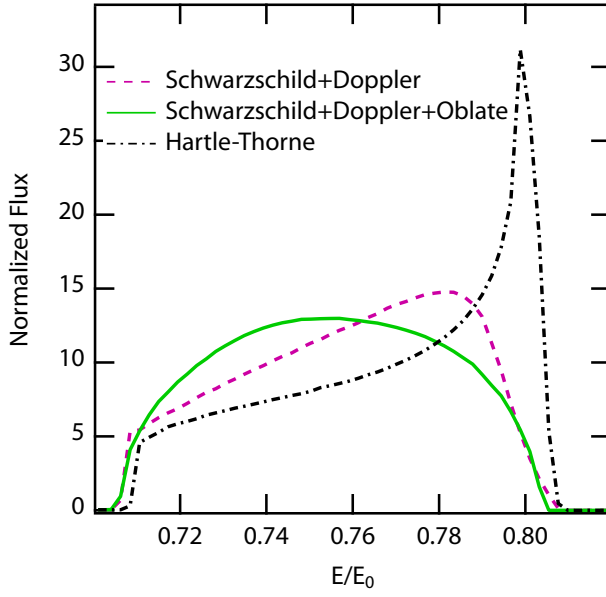
Figure 4.2: Line profiles computed by taking different properties of spinning neutron stars into account. In each case, the star is rotating at 700 Hz. As in Figure 4.1, the stars have a radius of 10 km, a mass of 1.4 $M_\odot$, and an inclination of 20°. The four lines show the results of calculations in four different approximations: the Schwarzschild+Doppler approximation for a spherical and an oblate star, and the Hartle-Thorne approximation for a spherical and an oblate star. The last case is identical to the 700 Hz profile shown in Figure 4.1.
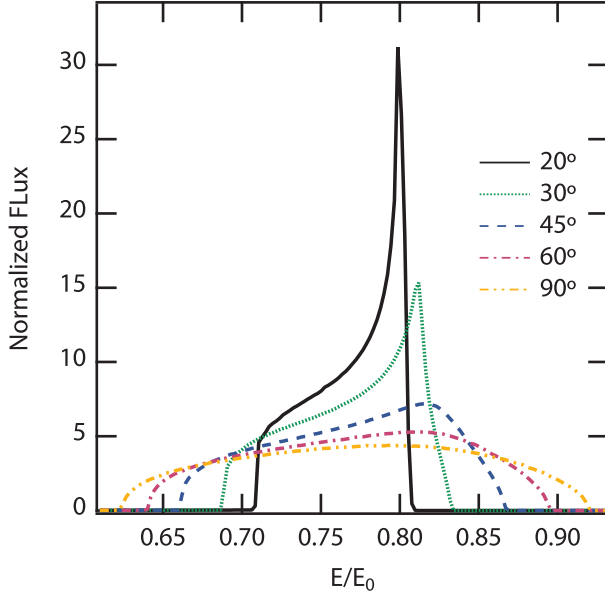
Figure 4.3: Line profiles for five different inclinations to the observer's line of sight. The neutron star has a radius of 10 km, a mass of 1.4 $M_\odot$, and a rotational frequency of 700 Hz. At high inclinations, the profile displays only Doppler broadening. At lower inclinations, however, a narrow peak appears.

quadrupole moments are large) and low inclinations (such that the Doppler effects are small) generate line profiles with remarkably narrow cores that are strongly peaked toward the blue end of the spectrum. These peaks are evident in the higher frequency simulations shown in the bottom panel of Figure 4.1.

The deviation at low inclinations from the Schwarzschild+Doppler predictions is due primarily to the quadrupole moment of the neutron star, with a small additional effect from the oblate shape of the surface. To disentangle the relative roles of the Doppler shift, the quadrupole moment, and the oblateness, I simulated two different scenarios: one in which the profile is calculated in the Schwarzschild+Doppler approximation and the other in which the full Hartle-Thorne metric is used. In each case, I performed the calculations both for a star with a spherical surface and for one in which the surface becomes oblate. The results are shown in Figure 4.2. The profile labeled "Spherical S+D" shows only the expected Doppler broadening and relativistic beaming. When I allow for the shape of the star to become oblate, the
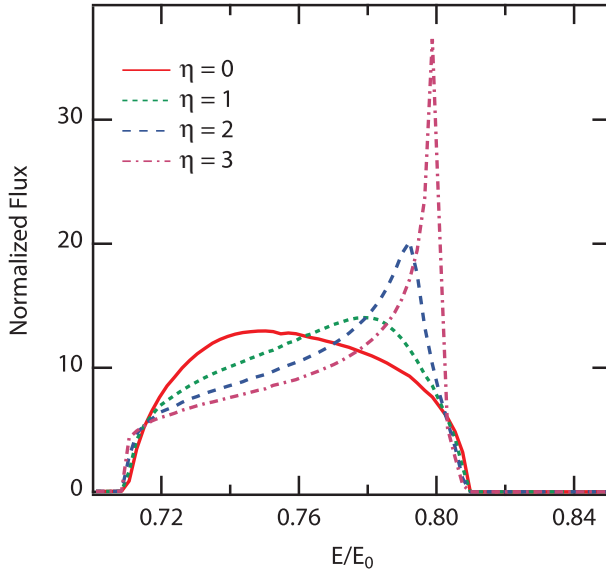
Figure 4.4: Line profiles for different values of the parameter η which measures the quadrupole moment of the neutron star. As in previous figures, the neutron star has a 10 km radius, a mass of 1.4 $M_\odot$, and a rotational frequency of 700 Hz. The inclination to the observer's line of sight is 20°. As the quadrupole moment (parametrized by η) increases, the line develops a narrow peak in the blueshifted portion of the spectrum.
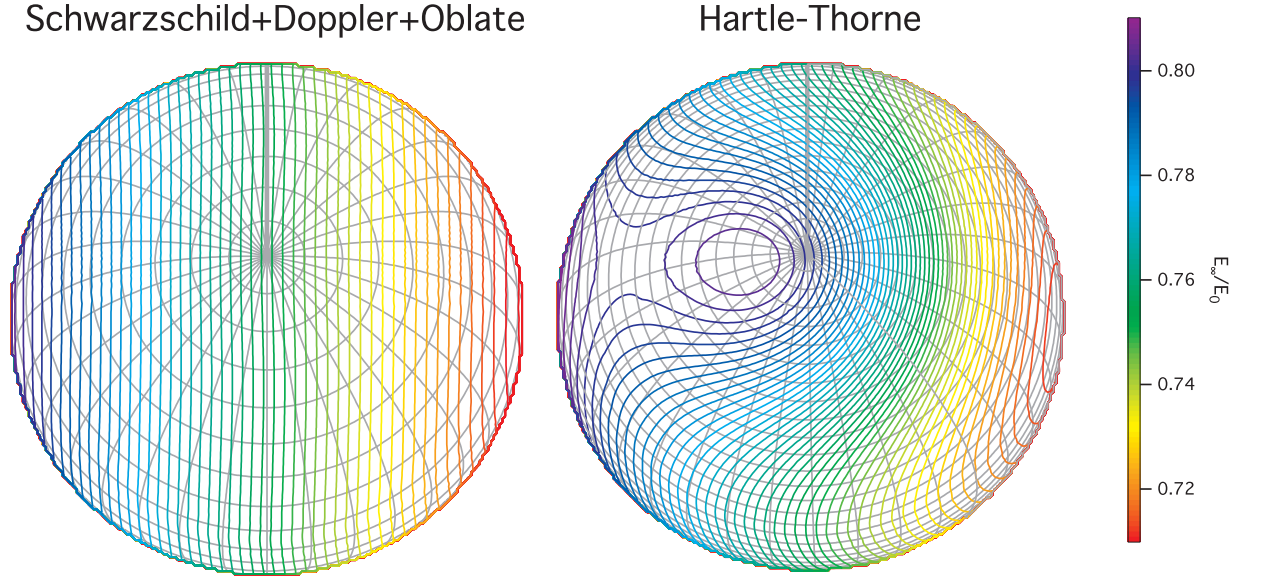
Figure 4.5: Contours of constant redshifted energy at the neutron star surface. The left panel shows the redshift for an oblate neutron star in the Schwarzschild+Doppler approximation, while the right panel includes a fiducial value for the neutron star's quadrupole moment as calculated by Laarakkers & Poisson (1999). In both cases, the star has a mass of 1.4 $M_\odot$, a radius of 10 km, an inclination of 20° to the observer's line of sight, and is rotating at 700 Hz. The star is rotating counterclockwise when viewed from above. In the right panel, the quadrupole moment of the neutron star causes a local extremum in the redshifted energy near rotational pole on the blueshifted side of the star. This maximum is responsible for the narrow core of the atomic features from moderately spinning neutron stars.

profile shifts toward the red. This shift is caused by the increased gravitational red-shift in the region near the pole. The effect of the oblate shape of the stellar surface is overpowered, however, by the contribution of a nonzero quadrupole moment. As shown in the two Hartle-Thorne scenarios illustrated in Figure 4.2, the quadrupole causes a narrow peak in the line profile for both the spherical and the oblate stellar surfaces.

This narrow peak vanishes at higher inclinations, as shown in Figure 4.3. The peak is very strong at inclinations below $30°$, but the effect of the quadrupole decreases rapidly as inclination increases because of the increasing relative importance of the Doppler broadening. When viewed perpendicular to the axis of rotation, the peak vanishes and the profile can be described purely by Doppler broadening. Moreover, the narrow core has a strong dependence on the magnitude of the quadrupole moment of the neutron star. Figure 4.4 shows line profiles for four different values of η, ranging from 0 (the Kerr case) to 3. As the quadrupole moment grows, the peak in the line profile becomes more pronounced. At the quadrupole moment predicted for this neutron star configuration, the narrow core dominates the line width.

The appearance of a narrow peak in the simulated spectra arises from the fact that the addition of a quadrupole moment causes a significant portion of the stellar surface to have roughly the same effective redshift. This effect is a combination of the varying Doppler shift across the surface and of the quadrupole component of the gravitational redshift. I show in Figure 4.5 contours of constant redshifted energy on the stellar surface for two stars: the right panel depicts a neutron star with my fiducial value of the quadrupole moment, while the left panel shows the same calculation performed in the Schwarzschild+Doppler metric for an oblate neutron star. On the star with zero quadrupole moment, the energy decreases monotonically toward the right (the receding side) due to the changing Doppler shift. In the other case, there is an additional effect due to the quadrupole moment that is symmetric about the pole of rotation. The result is a local maximum of energy that is offset slightly from the pole. The energy of this local maximum corresponds to the energy of the peak in Figure 4.1.

In Figure 4.6, I present another view of the combination of effects that give rise to these particular line profiles. The top panel shows the total redshifted energy as a function of colatitude for a constant value of the azimuth ϕ close to the local maximum for the configuration shown in the right panel of Figure 4.5. For a spherical star with no quadrupole, the redshift changes monotonically across the surface due to the Doppler shift. An oblate star with no quadrupole moment is more redshifted in the vicinity of the pole, causing the shift in the line peak seen in Figure 4.2. In contrast, for an oblate star with the fiducial quadrupole moment, a local maximum appears that is offset from the pole.

By taking various ratios of the curves shown in the upper panel of Figure 4.6, I can identify the effect of the oblateness and of the quadrupole moment. This is shown in the lower panel of Figure 4.6. For comparison, I also calculate the ratio of the g_{tt} terms of two metrics, one with fiducial quadrupole and the other with the quadrupole deviation set to zero:

$$\lambda = \frac{g_{tt,q}[\theta, R(\theta)]}{g_{tt,q=0}[\theta, R(\theta)]} \tag{4.1}$$

This ratio is shown as a dash-dotted curve in Figure 4.6. The similarity between the energy ratios and the metric curve strongly suggests that the maximum in redshifted energy is caused by the quadrupole moment.

Observed spectral lines from neutron star surfaces will be broadened by several effects in addition to the geometric effects considered above. In Figure 4.7, I show the broadening of several Gaussian lines with different intrinsic widths. Models of neutron-star surface emission predict line widths on the order of 10^{-3} (Özel 2013). As a result, the dotted line in Figure 4.7 shows a reasonable upper limit for the intrinsic line width expected from a neutron-star surface. For completeness, I also show profiles with significantly broader lines.

4.3 Discussion

Second order effects of the rotation of neutron stars introduce significant corrections to the observed profiles of atomic features from their surfaces. The dependence of these profiles on the inclination of the observer deviates strongly from the expected $\sin(\theta_0)$ behavior that is characteristic of Doppler effects. The principle cause of this deviation is the extra quadrupole mass moment induced by the rapid rotation of the star. The combination of the quadrupole moment and the Doppler shift due to the motion of the neutron star surface cause a strong and narrow feature to appear in the simulated spectra of emission lines. This narrow core is strongest at relatively low inclinations ($\theta_0 < 30°$) and high spin frequencies ($f_{NS} > 500$ Hz).

Several previous authors have modeled the relativistic effects on spectral lines emitted from neutron star surfaces. Özel & Psaltis (2003) calculate line broadening in a Schwarzschild metric with Doppler shifts. Taking into account these first-order effects of rotation, they found uniformly broadened profiles, as expected from pure Doppler effects. At high inclination to the observer's line of sight, where quadrupole effects are small, my profiles are consistent with these calculations.

Bhattacharyya et al. (2006) extended this analysis to include the effect of frame dragging. In their approximation, the authors assumed the neutron star to be spherical and the exterior spacetime to be described by the Kerr metric. Moreover, they assumed that line emission is confined to a band of latitudes on the surface of the neutron star. A neutron star in the Kerr metric has a small but non-zero quadrupole moment, so in principle narrow line cores could result in this approximation as well. However, because the quadrupole moment is small, the effect is only apparent at high spin frequencies, very low observer inclinations, and for bands of emission close to the rotational pole. The profiles in Bhattacharyya et al. (2006) are predominantly at high observer inclinations and for emission bands close to the rotational equator; therefore the effects of the Kerr quadrupole moment on their profiles is negligible.

Chang et al. (2006) calculated line profiles using numerical metrics for several equations of state. These numerical metrics incorporate appropriate quadrupole

and higher order moments of the spacetime and should, therefore, reproduce the effects discussed here. However, the authors confined their analysis to high-inclination sources and relatively low spin frequencies, at which the contribution of the quadrupole moment to the line profile is small.

Figure 4.8 shows a contour plot of the simulated full width at half-maximum of emission lines for a range of spin frequencies and inclinations. At high inclinations, the interpretation of line widths is straightforward, with narrow lines corresponding to slow rotation and broad lines implying fast rotation. At lower inclinations, however, there is often a degeneracy. Narrow lines could be caused by slow rotation or by the higher quadrupole induced by rapid rotation. Clearly, line broadening can only be used as a reliable measure of neutron star radii if additional information is available on the inclination of the observer and the spin frequency.

The presence of a narrow core in atomic features also increases the range of inclinations at which these features are detectable. At high spin frequencies and relatively low observer inclinations, atomic features from realistic stars are narrower than those expected from purely Doppler effects (Chang et al. 2006). This may allow for such features to be discernible from continuum spectra and translates into a larger solid angle over which they are detectable

The models presented here may shed new light on observations of the source EXO 0748–676. *XMM* observations of this source showed evidence for narrow absorption lines (Cottam et al. 2002), which were later used to constrain the mass and radius of the neutron star (e.g., Özel 2006). However, Lin et al. (2010) argued that the subsequent detection of the 552 Hz spin frequency and the large amplitude of burst oscillations were incompatible with the narrow observed width of the absorption lines and concluded that these lines did not originate at the neutron star surface.

In their calculations, Lin et al. (2010) use the Schwarzschild+Doppler approach to model the line spectra. As shown above, however, the inclusion of second-order effects leads to narrow profiles for much higher inclinations at a given spin frequency. Therefore, it appears plausible that the narrowness of the absorption lines is not incompatible with the high amplitudes of the observed burst oscillations and, therefore

does not exclude the possibility that they were emitted from the surface. A detailed analysis of the EXO 0748–676 case will be presented in a future paper.
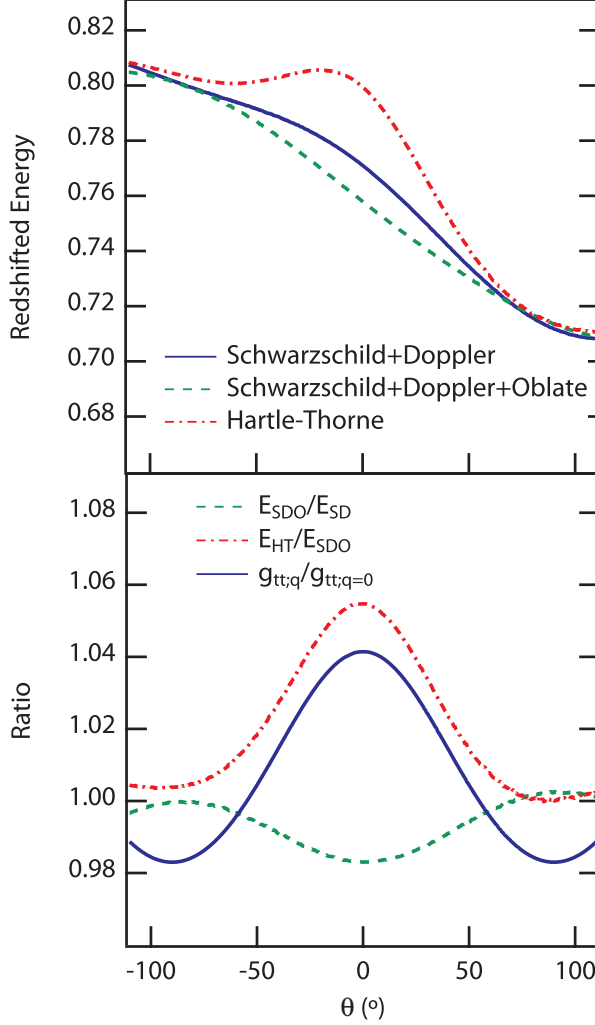
Figure 4.6: The top plot shows the redshifted energy of photons originating on the neutron star surface as a function of colatitude θ for a fixed value of the azimuth ϕ and for the neutron star parameters depicted in Figure 4.5. The colatitude θ is zero at the rotational pole; it assumes negative values on the blueshifted side of the star and positive values on the redshifted side. The three lines correspond to three different configurations of the neutron star: one in which the star is spherical and has no quadrupole moment, one in which the star is oblate with no quadrupole moment, and one with both oblateness and a quadrupole moment. In the lower panel, the dashed line shows the ratio of redshifted energies on a spherical neutron star to those on an oblate one. The dash-dotted line shows the ratio of the redshifted energies of a neutron star with a quadrupole moment to those on a star without. The solid line shows the ratio λ of the g_{tt} components of two different spacetimes: one in which the quadrupole deviation is set to zero and another in which the quadrupole is set to its fiducial value.
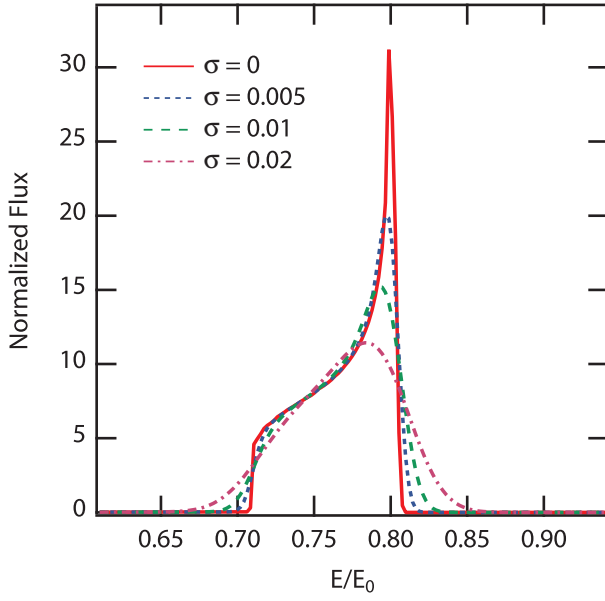
Figure 4.7: Line profiles for different intrinsic line widths. In each case, the result of the ray tracing for a star of 1.4 $M_\odot$ and a radius of 10 km spinning at 700 Hz is convolved with a Gaussian profile of width σ. The solid red profile shows a line with an infinitesimal intrinsic width and corresponds to the profile shown in Figures 4.1—4.3. In order to illustrate the effect of intrinsic line broadening, I have included profiles corresponding to unrealistically broad lines. In practice, intrinsic line widths are expected to be at or below the $\sigma = 0.005$ level shown by the blue dotted curve.
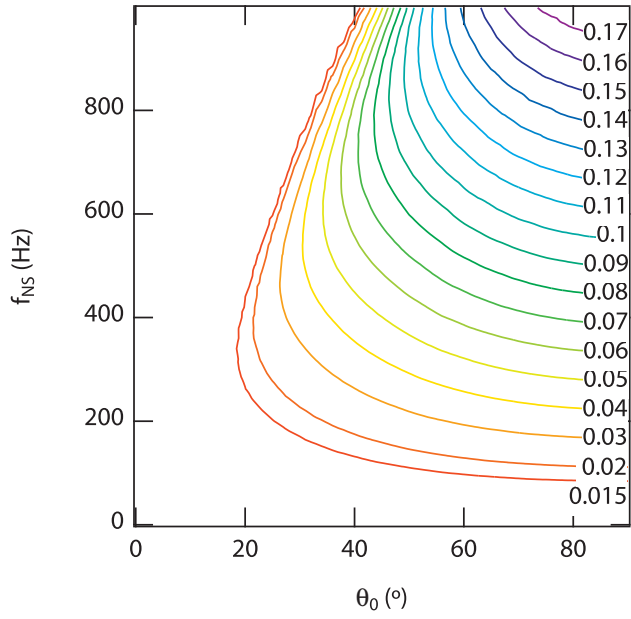
Figure 4.8: Contour plot of the full width at half maximum of the line profile from a spinning neutron star of 1.4 $M_\odot$ and a radius of 10 km as a function of spin frequency and inclination angle.

CHAPTER 5

Relations Between Neutron-Star Parameters in the Hartle-Thorne Approximation

5.1   Neutron-Star Parameters

In the Hartle-Thorne metric, the appearance of a neutron star as measured by an observer at spatial infinity depends on seven macroscopic parameters: the mass M, the equatorial radius R_{eq}, the spin frequency f, the inclination of the rotational pole with respect to the observer θ_0, the angular momentum J, the quadrupole moment Q, and the eccentricity of the surface e_s. Three of these parameters (f, θ_0, and, e.g., M) are independent of the equation of state for any given observed source. The remaining four parameters (R_{eq}, J, Q, and e_s) are uniquely determined by the equation of state, given a neutron star mass and spin frequency. Therefore, it is any of these four parameters that need to be measured observationally, in addition to the mass and spin frequency, in order for the underlying equation of state to be constrained.

Even though measuring only one of the four dependent parameters with high precision would be sufficient, typical observables depend on all seven parameters in a complex manner. It is unlikely that spectroscopic or timing observations in the near future will be accurate enough to allow for independent measurements of all of these parameters in individual neutron stars. In the work described above, I have assumed a sample equation of state in order to set the relations between those parameters that are not directly measured. In order to make progress, I can reduce the dimensionality of the problem by using approximate relations that connect quantities that are higher order in spin frequency (such as the spin angular momentum J, the space-time quadrupole Q, and the ellipticity of the stellar surface e_s) to ones that are of lower order (such as the mass M and equatorial radius R_{eq}). In this way, observable phenomena from a moderately spinning neutron star can be calculated based only on

its mass and equatorial radius, given a spin frequency and an observer's inclination.

This reduction of the parameter space by means of approximate relations allows for the properties of dense matter to be constrained only if the relations themselves do not depend strongly on the details of the equation of state. Andersson & Kokkotas (1998) modeled pulsation modes of neutron stars and showed that the relations between several parameters of interest have a significant dependence on the equation of state. However, given the constraints imposed on the equation of state of dense matter by recent observations (e.g., Demorest et al. 2010; Antoniadis et al. 2013), I show that it is possible to find relations between the parameters described above that are valid over the astrophysically relevant parameter range and for a variety of equations of state.

Several authors to date have explored such approximate relations in different contexts. Ravenhall & Pethick (1994) and Lattimer & Prakash (2001) provide empirical formulae for the moments of inertia and binding energies of slowly spinning neutron stars as a function of their masses and radii. Morsink et al. (2007) obtained empirical formulae that connect the ellipticity of the surfaces of spinning neutron stars to their masses, equatorial radii, and spin frequencies. More recently Urbanec et al. (2013) modeled the angular momenta and quadrupole moments of both neutron stars and strange stars, showing that different relations exist for these two classes of objects. Finally, Yagi & Yunes (2013a) found relations between the moment of inertia, the quadrupole moment, and the tidal Love number that are highly accurate for several equations of state.

In this chapter, I model the properties of moderately spinning neutron stars in the Hartle-Thorne approximation, which is adequate for spin frequencies $\lesssim 800$ Hz. I derive an analytic expression connecting the ellipticity of the stellar surface to the compactness, the spin angular momentum, and the spacetime quadrupole. I also obtain empirical relations between the compactness, the spin angular momentum, and the spacetime quadrupole similar to those found in Lattimer & Prakash (2001) and Yagi & Yunes (2013a). These relations allow me to fully determine the parameters of a neutron star given a measurement of its mass, radius, and spin frequency. I

demonstrate that these formulae reproduce the results of numerical calculations of neutron-star spacetimes to within a few percent. This is sufficient for comparing theoretical spectroscopic and timing models to observations that aim to measure the masses and radii of neutron stars and to determine the high-density equation of state prevailing in their interiors.

5.2 Numerical Models in the Hartle-Thorne Approximation

The Hartle-Thorne metric is based on a slow-rotation expansion. If the expansion is truncated at second order in the spin frequency, the spacetime exterior to a rotating object can be described by three parameters: the total mass, the angular momentum, and the quadrupole moment of a neutron star. Observationally, the appearance also depends on the geometry of its surface, i.e., on its equatorial radius and ellipticity.

Out of these parameters, I choose the mass M and the equatorial radius R_{eq} to characterize each neutron star. The other three parameters depend on the equation of state but are of higher order in spin frequency and introduce small corrections to most observables (e.g., Poisson 1998; Morsink et al. 2007; Racine 2008; Bauböck et al. 2013; Psaltis & Özel 2013). Therefore, I aim to find relations that allow for these parameters to be approximated given a neutron-star mass and radius, independent of the equation of state.

The angular momentum J of a neutron star is often represented by the dimensionless spin parameter

$$a \equiv \frac{cJ}{GM^2}, \tag{5.1}$$

which is zero for a non spinning object. Neutron stars typically have a spin $a \leq 0.7$ for uniform rotation and physically motivated equations of state (Cook et al. 2004, Berti & Stergioulas 2004, Lo & Lin 2011), but the spin magnitudes of neutron stars in binaries observable by Advanced LIGO are likely to be much smaller than this theoretical upper bound (Mandel & O'Schaughnessy 2010, Brown et al. 2012). The spin periods of isolated neutron stars at birth should be in the range 10-140 ms (Lorimer 2001), or $a \lesssim 0.04$. Accretion from a binary companion can spin up neutron

stars but is unlikely to produce periods less than 1 ms, i.e., $a \lesssim 0.4$ (Ferdman et al. 2008). The fastest-spinning observed pulsar has a period of 1.4 ms, ($a \sim 0.3$) (Hessels et al. 2006); the fastest known pulsar in a neutron star-neutron star system, J0737-3039A, has a period of 22.70 ms ($a \sim 0.02$; Burgay et al. 2003). The spin parameter depends both on the rotational period and on the moment of inertia of the neutron star, which is determined by the equation of state.

A spinning neutron star also acquires a nonzero quadrupole moment Q. I characterize the quadrupole moment by the dimensionless quantity

$$q \equiv -\frac{c^4 Q}{G^2 M^3}. \tag{5.2}$$

Laarakkers & Poisson (1999), Berti & Stergioulas (2004), and Pappas & Apostolatos (2012) computed the quadrupole moment of rapidly spinning neutron stars for a range of equations of state. They found values of q ranging between 1 and 11 (see also Bauböck et al. 2012).

Lastly, a spinning neutron star also becomes oblate in shape. In the Hartle-Thorne approximation, this oblateness is described by

$$R(\theta) = R_0 + \xi_2 P_2(\cos\theta), \tag{5.3}$$

where P_2 is the second-order Legendre polynomial and ξ_2 is a coefficient depending on the equation of state and spin frequency of the neutron star. In the non-spinning limit, $\xi_2 = 0$ and $R(\theta) = R_0$. For moderately spinning neutron stars, there are two frequently used parameters to characterize the oblate shape: the eccentricity of the surface,

$$e_s \equiv \sqrt{\left(\frac{R_{\mathrm{eq}}}{R_{\mathrm{p}}}\right)^2 - 1}, \tag{5.4}$$

and its ellipticity,

$$\varepsilon_s \equiv 1 - \frac{R_{\mathrm{p}}}{R_{\mathrm{eq}}}, \tag{5.5}$$

where R_{eq} is the equatorial radius and R_{p} is the radius at the pole.

As in Berti et al. (2005), I expand the parameters a, q, e_s, and ε_s to second order in the spin frequency of the neutron star. Specifically, I define the parameter

$$\epsilon_0 \equiv \frac{f}{f_0} \tag{5.6}$$

in terms of the characteristic frequency

$$f_0 \equiv \sqrt{\frac{GM_0}{R_0^3}}. \tag{5.7}$$

In this equation, M_0 and R_0 are the non-spinning mass and radius of the neutron star. The characteristic frequency f_0 corresponds to the Keplerian orbital period of a test particle at a radius R_0 around a mass M_0 and thus corresponds roughly to the maximum frequency a neutron star can be spun up to before breakup. For spin frequencies much smaller than this characteristic frequency ($f < f_0$), ϵ_0 serves as a suitable small parameter about which I can expand the metric. When f approaches f_0, the parameter ϵ_0 approaches unity, and the Hartle-Thorne approximation is no longer valid. The spin frequency at which this occurs depends on M_0 and R_0 and, therefore, on the equation of state. However, for most proposed equations of state, this approximation is valid for even the most rapidly spinning neutron stars observed to date (Berti et al. 2005).

For a non-spinning neutron star, the parameter ϵ_0 is equal to zero, and thus the spin a, the quadrupole moment q, and the eccentricity of the surface e_s are all zero, as well. As the spin frequency increases, corrections to the metric enter at different orders in ϵ_0. To first order in the spin frequency, the star acquires a non-zero angular momentum, characterized by the spin parameter a. To the lowest order, I can approximate the spin parameter as a linear function of spin frequency, i.e.,

$$a = \epsilon_0 a^*, \tag{5.8}$$

where a^* is a constant that depends on the equation of state. To second order in the

spin frequency, the star acquires a quadrupole moment and an elliptical shape, i.e.,

$$q = \epsilon_0^2 q^* \qquad (5.9)$$

and

$$\frac{R_{\text{eq}}}{R_{\text{p}}} = 1 + \epsilon_0^2 R^*, \qquad (5.10)$$

where q^* and R^* are again constants depending on the equation of state. Substituting Equation (5.10) into Equations (5.4) and (5.5) shows that the eccentricity of the surface of the neutron star has a first order dependence on the spin frequency

$$e_s = \epsilon_0 e_s^*, \qquad (5.11)$$

while the ellipticity has a second-order dependence on the spin frequency, i.e.,

$$\varepsilon_s = \epsilon_0^2 \varepsilon_s^*. \qquad (5.12)$$

The above relations all depend on ϵ_0, which in turn depends on the non-spinning values M_0 and R_0. For a spinning neutron star, however, these quantities are not readily measurable. Instead, observations can only constrain the spinning mass and equatorial radius, M and R_{eq}, respectively. These parameters differ from their non-spinning values at second order in ϵ_0:

$$M = M_0 + \epsilon_0^2 \delta M^*, \qquad (5.13)$$

$$R_{\text{eq}} = R_0 + \epsilon_0^2 \delta R^*, \qquad (5.14)$$

where δM^* and δR^* are again constants depending on the equation of state. Since M and R_{eq} differ from M_0 and R_0 at second order in ϵ_0, the corrections introduced to Equations (5.8)–(5.11) by the altered mass and radius will necessarily enter at third or fourth order in ϵ_0. Therefore, the lowest-order effects will be unchanged. For the remainder of this work, I will use the spinning mass and radius interchangeably with the nonspinning values.

I use the procedure described in Berti et al. (2005) to calculate the values of the parameters described above for several neutron-star equations of state. For a given equation of state, a central density and spin frequency uniquely determine the properties of a neutron star in the Hartle-Thorne approximation. First, I solve the Tolman-Oppenheimer-Volkoff equations to find the parameters of a non-spinning star with the same equation of state and central density. In this non-spinning case, a, q, and e_s^* are equal to 0. Next, I solve the full Hartle-Thorne equations for the perturbative quantities, i.e. q^*, a^*, R^*, e_s^*, and ε_s^*. Once I have found the values of these starred parameters, I can then use Equations (5.8)–(5.12) to determine the parameters of a neutron star spinning at any intermediate rate characterized by $\epsilon < \epsilon_0$.

5.3   Relations Between Spin, Quadrupole, and Compactness

As in Lattimer & Prakash (2001) and Yagi & Yunes (2013a), I find that tight empirical relations exist between the spin parameter a^*, the dimensionless quadrupole moment q^*, and the compactness $\zeta = GM_0/R_0c^2$ of neutron stars that depend very weakly on the assumed equation of state. In addition, I derive an analytic formula relating these four quantities to the eccentricity parameter e_s^* and the ellipticity parameter ε_s^* of the neutron star surface.

In order to generate my fits, I selected several modern equations of state. Observations by Demorest et al. (2010) of a 1.97 $M_\odot$ neutron star and by Antoniadis et al. (2013) of a 2.01 $M_\odot$ neutron star place significant constraints on the properties of dense matter and strongly disfavor several equations of state. I selected only equations of state that allow a maximum mass of at least 2.0 $M_\odot$. Following the naming convention of Lattimer & Prakash (2001), I chose for the fits the equations of state AP4, ENG, MPA1, and MS0, which cover a wide range of microphysics assumptions and calculational procedures.

For each equation of state, I use a large number of numerical models covering the astrophysically relevant range of masses $M > 1.0$ $M_\odot$ (Özel et al 2012). A least-squares polynomial fit of the spin parameter a^* as a function the compactness
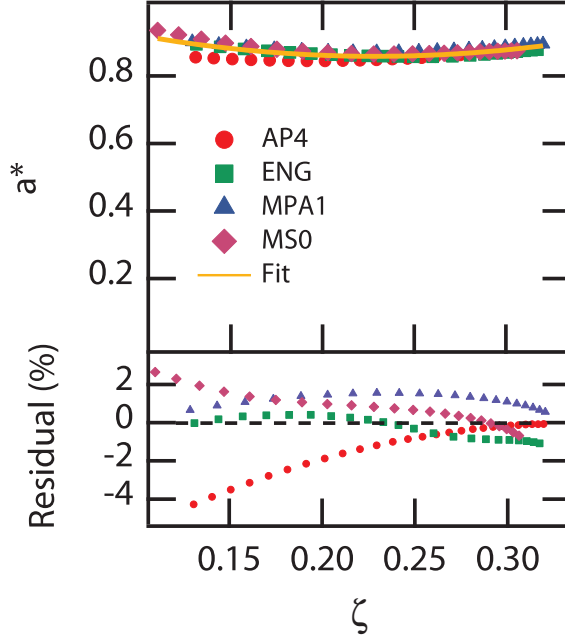
Figure 5.1: Empirical fit to the correlation between spin and compactness of a neutron star for four equations of state, corresponding to equation (5.15). The lower panel shows the residual in percent.

yields

$$a^* = 1.1035 - 2.146\zeta + 4.5756\zeta^2 \,. \tag{5.15}$$

Figure 5.1 shows this fit as a solid line, along with the results of numerical calculations for four different equations of state. The lower panel shows the residuals: for all equations of state, the residuals over the range of masses considered here are less than 4%.

Both Lattimer & Prakash (2001) and Yagi & Yunes (2013b) found similar empirical relations between the moment of inertia and the compactness. These authors consider a wider range of equations of state and neutron star parameters than those included in Figure 5.1. For less compact neutron stars than those shown in Figure 5.1, i.e., typically those with masses <1 $M_\odot$, different equations of state predict more divergent values for the moment of inertia (or equivalently the spin parameter a^*). For the purpose of modeling observations of astrophysical neutron stars,

however, the relation given in Equation (5.15) is adequate.

In order to determine the quadrupole moment, I adopt the relation proposed by Yagi & Yunes (2013b). These authors present a relation between the quadrupole moment and moment of inertia of spinning neutron stars with a variety of equations of state. They define a dimensionless quadrupole moment $\bar{Q}$ and moment of inertia $\bar{I}$ that relate to my q^* and a^* via

$$\bar{Q} \equiv \frac{q^*}{a^{*2}}, \tag{5.16}$$

and

$$\bar{I} \equiv a^* \zeta^{-3/2}. \tag{5.17}$$

They then find an empirical expression for $\bar{I}$ as a function of $\bar{Q}$. Since the inverse of this relation is required for use with the fit for the spin parameter a^* in Equation (5.15), I find instead an analogous fit for $\bar{Q}$ as a function of $\bar{I}$,

$$\begin{aligned}
\ln \bar{Q} &= -2.014 + 0.601 \ln \bar{I} + 1.10 (\ln \bar{I})^2 \\
&\quad - 0.412 (\ln \bar{I})^3 + 0.0459 (\ln \bar{I})^4.
\end{aligned} \tag{5.18}$$

Alternatively, the fit of Yagi & Yunes (2013b) can be inverted numerically to obtain an equivalent relation. The above fit is shown as the solid line in Figure 5.2 along with numerical calculations for the chosen equations of state. Again, the residuals shown in the lower panel are less than 2% for each considered equation of state.

5.4 Relations for the Elliptical Shape of the Neutron Star Surface

Given these two empirical fits for the spin parameter and quadrupole moment, I now find an analytic expression for the eccentricity of the neutron star surface. Hartle & Thorne (1968) solved the equations of stellar structure at second order in spin frequency and showed that the eccentricity of the neutron star surface measured in flat space is given by

$$e_s = \sqrt{-3(v_2 - h_2 + \xi_2/R_0)}, \tag{5.19}$$
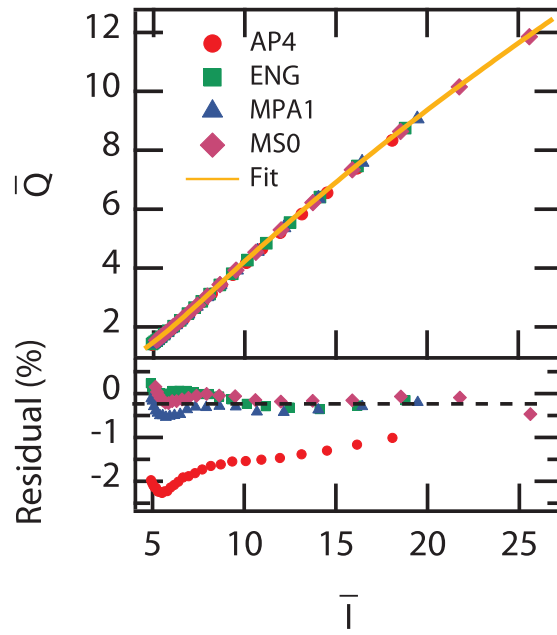
Figure 5.2: Empirical fit to the correlation between the dimensionless quadrupole moment $\bar{Q}$ and angular momentum $\bar{I}$. The fit corresponds to Equation (5.18) and is equivalent to that proposed in Yagi & Yunes (2013b). The lower panel shows the residual to the fit in percent.

where v_2 and h_2 are functions of R_0 that are second order in spin, and ξ_2 is the parameter defined in Equation (5.3). Hartle & Thorne (1968) provide the exact forms of the quantities v_2 and h_2 as functions of the mass, radius, angular momentum, and quadrupole moment. Using Equations (5.1) and (5.2), I can reduce Equation (5.19) to depend only on the dimensionless parameters ζ, a, q, and ϵ_0 defined above. Substituting a^* and q^* for a and q via Equations (5.8) and (5.9) and using the definition of e_s^* in Equation (5.11), I can eliminate the dependence on spin and find an analytic expression for the eccentricity e_s^*,

$$
\begin{aligned}
e_s^*(\zeta, a^*, q^*) = \Big[& 1 - 4a^*\zeta^{3/2} \\
& + \frac{15(a^{*2} - q^*)(3 - 6\zeta + 7\zeta^2)}{8\zeta^2} + \zeta^2 a^{*2}(3 + 4\zeta) \\
& + \frac{45}{16\zeta^2}(q^* - a^{*2})(\zeta - 1)(1 - 2\zeta + 2\zeta^2)\ln(1 - 2\zeta) \Big]^{1/2}.
\end{aligned}
\tag{5.20}
$$

Figure 5.3 shows this expression for the eccentricity as a function of the compactness, along with numerical calculations from several equations of state. I have substituted Equations (5.15), (5.17) and (5.18) into Equation (5.20) in order to present the relation as a function of the single parameter ζ. The residuals to this relation are shown in the lower panel. The residuals are nonzero due to the empirical nature of the fits between a^*, q^*, and ζ.

Alternatively, Hartle (1967) gives an expression for the ellipticity of the neutron star surface in Hartle-Thorne coordinates as

$$
\varepsilon_s = -\frac{3}{2R}\xi_2.
\tag{5.21}
$$

Again, I can reduce this equation to depend only on the dimensionless parameters and eliminate the spin dependency to find an expression for ε_s^*,
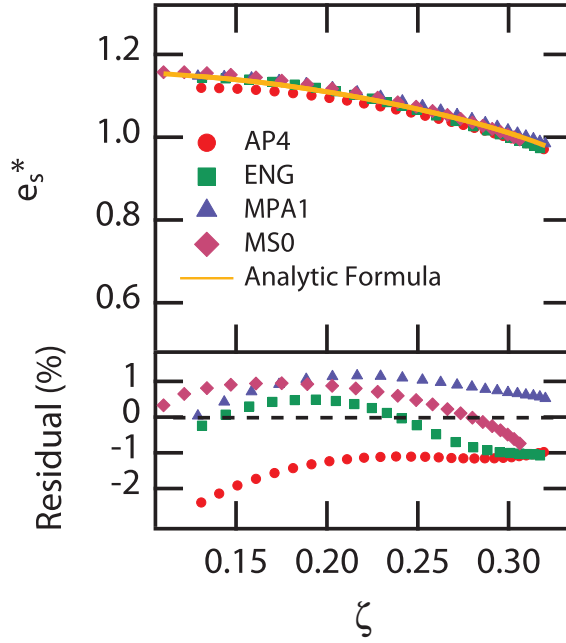
Figure 5.3: Analytic expression for the eccentricity of the neutron star surface, corresponding to Equation (5.20). In order to express this relation as a function of a single parameter, I have combined Equation (5.20) with the empirical fits for the quadrupole moment and spin parameter from Equations (5.15) and (5.18). The lower panel shows the residual to the relation in percent. Although the analytic relation is exact, the empirical fits between a^*, q^*, R, and M introduce some scatter about this relation.

$$\epsilon_s^*(\zeta, a^*, q^*) = \frac{1}{32\zeta^3} \left\{ 2\zeta \left[8\zeta^2 - 32a^*\zeta^{7/2} \right. \right.$$

$$+ (a^{*2} - q^*)(45 - 135\zeta + 60\zeta^2 + 30\zeta^3) + 24a^{*2}\zeta^4 + 8a^{*2}\zeta^5$$

$$\left. \left. - 48a^{*2}\zeta^6 \right] + 45(a^{*2} - q^*)(1 - 2\zeta)^2 \ln(1 - 2\zeta) \right\}. \quad (5.22)$$

5.5   Applications

In order to reduce the number of parameters necessary when fitting a neutron star observation, the following procedure can be used. For a given value of M, R_{eq}, and f, one can calculate the parameter ϵ_0 via Equations (5.6) and (5.7) as

$$\epsilon_0 = f \left(\frac{GM}{R_{eq}^3} \right)^{-1/2}. \quad (5.23)$$

The spin parameter a can then be found from Equation (5.15),

$$a = \epsilon_0 \left[1.1035 - 2.146\zeta + 4.5756\zeta^2 \right]. \quad (5.24)$$

The fit between moment of inertia and the quadrupole moment can then be used to write

$$q = a^2 \exp \left[- 2.014 + 0.601 \ln \left(\frac{a}{\epsilon_0} \zeta^{-3/2} \right) \right.$$

$$+ 1.10 \ln \left(\frac{a}{\epsilon_0} \zeta^{-3/2} \right)^2 - 0.412 \ln \left(\frac{a}{\epsilon_0} \zeta^{-3/2} \right)^3$$

$$\left. + 0.0459 \ln \left(\frac{a}{\epsilon_0} \zeta^{-3/2} \right)^4 \right]. \quad (5.25)$$

The parameters $a^* \equiv a/\epsilon_0$ and $q^* \equiv q/\epsilon_0^2$ can then be used in Equations (5.20) or (5.22) to find the eccentricity or ellipticity parameter of the neutron star surface in the appropriate spacetime. As defined in Equation (5.22), the ellipticity of the neutron
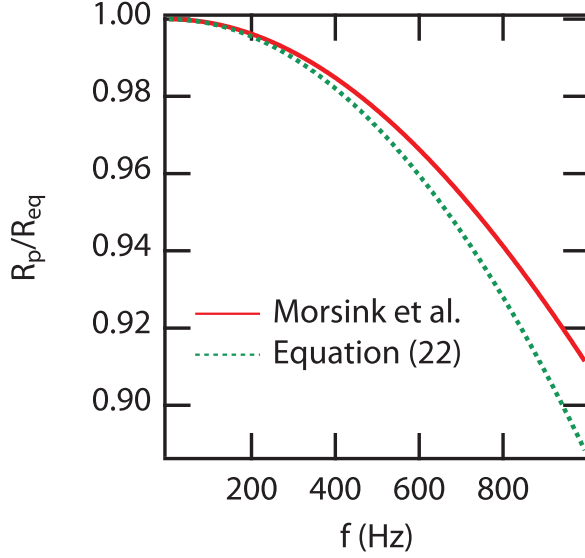
Figure 5.4: Comparison of the ratio of polar radius to equatorial radius found in this work and the ratio found by Morsink et al. (2007)

star is given in Hartle-Thorne coordinates. In order to convert to the commonly used Boyer-Lindquist coordinate system, the following transformation can be applied:

$$R_{\mathrm{BL}}(R_{\mathrm{HT}}, \theta) =$$

$$R_{\mathrm{HT}} - \frac{a^2 \left(\frac{GM}{c^2}\right)^2}{2R_{\mathrm{HT}}^3} \left[\left(R_{\mathrm{HT}} + 2\frac{GM}{c^2}\right) \left(R_{\mathrm{HT}} - \frac{GM}{c^2}\right) \right.$$

$$\left. - \cos^2(\theta) \left(R_{\mathrm{HT}} - 2\frac{GM}{c^2}\right) \left(R_{\mathrm{HT}} + 3\frac{GM}{c^2}\right) \right] \quad (5.26)$$

where R_{HT} is the radial coordinate in the Hartle-Thorne coordinate system and R_{BL} is the radial coordinate in the Boyer-Lindquist coordinate system (Hartle & Thorne 1968).

In the context of modeling pulse profiles, Morsink et al. (2007) similarly reduce the parameter space by finding an empirical description of the oblate shape of spinning neutron stars that is accurate for multiple equations of state. They find that compact objects can be divided into two broad classes with different oblateness at high spin frequencies. Normal neutron stars and hybrid quark stars follow one relation, while
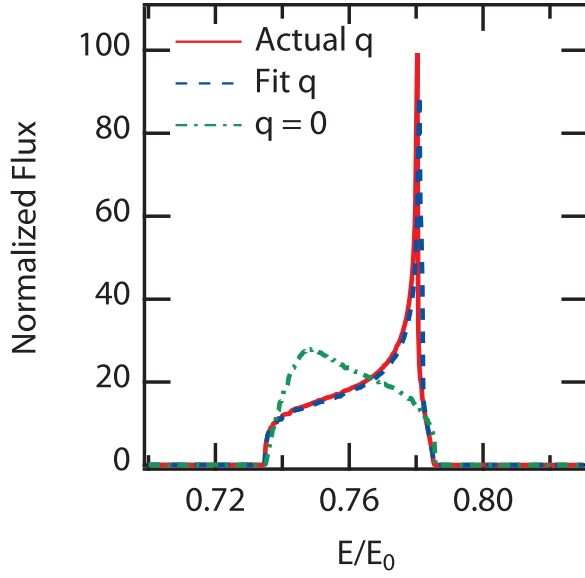
Figure 5.5: Simulated line profiles of an emission line from a neutron-star surface. The solid line shows a profile calculated using parameters from a numerical simulation of an AP4 star with a mass of 1.40 $M_\odot$ and a spin frequency of 700 Hz. The dashed line shows a star with the same mass, spin frequency, and radius (10.18 km), but with the quadrupole moment, spin parameter, and eccentricity determined by my fits. For reference, the dash-dotted line shows a profile with identical parameters but with the quadrupole moment set to zero. The photon energy at infinity and in the local Lorentz frame are denoted by E and E_0, respectively.

color-flavor–locked stars exhibit a different behavior. In both cases, Morsink et al. (2007) find that the deviation of the stellar surface from the spherical shape is proportional to the square of the spin frequency, with some additional correction at fourth order in the spin.

The empirical model of Morsink et al. (2007) for calculating the shape of normal neutron stars should agree with the analytic formula I find above when compared in the same coordinate system. Morsink et al. (2007) define the shape of the stellar surface in the Schwarzschild coordinate system. Since the Boyer-Lindquist coordinate system reduces to the Schwarzschild coordinate system in the limit of zero spin, I use Equation (5.22) to calculate the ellipticity in Hartle-Thorne coordinates and apply the change of coordinates described in Equation (5.26). Figure 5.4 shows the predicted ratio of the polar to the equatorial radius in the model of Morsink et al. (2007) as well as the analytic relation described above for a range of spin frequencies. In both models a neutron star with a mass of 1.4 $M_\odot$ and a radius of 10 km was used. The deviation derived here of the empirical model of Morsink et al. (2007) and the analytic formula is of order 1% in the range of observed spins.

The neutron-star shape and quadrupole moment play an important role in the profiles of lines that originate on neutron-star surfaces. Bauböck et al. (2013) showed that, at low inclinations, the quadrupole moment can cause anomalously narrow features to appear even for neutron stars spinning at moderate rates. In order to test whether the fits proposed in this work are precise enough to accurately model line profiles, I compared the profile calculated with the parameters predicted by a numerical simulation to one using the parameters from my fits. I show the result in Figure 5.5. For this example, I chose a model where the fits have large residuals, especially for the quadrupole moment, which provides the dominant contribution to the profile shape (Bauböck et al 2013). Even in this case, the narrow profile is recovered, and the difference in the resulting profiles is negligible.

5.6   Conclusions

I have demonstrated that several macroscopic parameters of spinning neutron stars can be approximated with high accuracy using relations that depend only on their masses, radii, and spin frequencies, but that are practically independent of the equation of state. These fits enable measurements of neutron-star masses and radii using X-ray spectroscopy, timing observations of pulse profiles, and gravitational-wave observations of neutron stars spinning at moderate frequencies.

Future detectors such as NICER, LOFT, and Advanced LIGO will soon allow for more precise measurements of neutron-star parameters than have been possible to date. Using these observations to constrain the equation of state of the dense matter found in neutron star cores requires that the parameter space be reduced in order to determine the mass and radius with the highest precision. The relations demonstrated above allow this reduction of the parameter space independent of the equation of state, making possible more precise measurement of the equation of state of neutron-star cores.

CHAPTER 6

Rotational Corrections to Neutron-Star Radius Measurements from Thermal
Spectra

6.1   Thermal Emission from the Stellar Surface

Although to date no observations of atomic emission or absorption lines from neutron-
star surfaces have been confirmed, thermal emission from the stellar surface has
been successfully used to constrain masses and radii. However, these measurements
have relied on the assumption that the sources are spinning too slowly to affect the
spectrum of radiation emitted from the surface. Here I investigate this assumption
by modeling thermal spectra that have been broadened and distorted by the neutron-
star spin.

An important component of theoretical modeling is related to spectral distortions
caused by radiative transfer effects in the neutron-star atmosphere. Because the free-
free opacity depends strongly on photon energy, the color temperature measured from
the peak of the spectrum emerging from the atmosphere is expected to be significantly
higher than the effective temperature of the surface (van Paradijs 1979). In addition,
the Compton scattering of photons off of the free electrons in the atmosphere further
distort the emitted spectra (London et al. 1986). Accurate models of neutron-star
atmospheres have accounted for these effects for a wide range of stellar parameters
(London et al. 1986; Madej et al. 2004; Suleimanov et al. 2012) and the results
of these calculations have been converging and now agree to within 10% (see the
discussion in Özel 2013).

I calculate simulated spectra from moderately spinning sources using an algorithm
(Bauböck et al. 2012, 2013b) that traces rays in a variant of the Hartle-Thorne metric
(Hartle & Thorne 1968). I investigate the distortions in the broadband spectra
resulting from spin effects, taking into account the oblate shape of the stellar surface

and the quadrupole moment of the metric. Using these model spectra, I calculate correction terms to account for the effects of rotation on measurements of the effective temperature, flux, and spectroscopic radius that are accurate for spin frequencies up to 800 Hz. These can be used to infer neutron-star radii from moderately spinning sources.

6.2 Spectral Modeling

In principle, the metric of the spacetime around the neutron star depends on six parameters: the mass M, the equatorial radius R, the spin frequency f_{NS}, the moment of inertia I, the quadrupole moment Q, and the ellipticity of the surface of the star ε. Additionally, measurements of the source depend on the inclination of the spin axis to the observer's line of sight θ_O. Using empirical and analytic relations discussed above (see also Bauböck et al. 2013a; Morsink et al. 2007; see also AlGendy & Morsink 2014), I determine three of these parameters (I, Q, and ε) in terms of only the mass, equatorial radius, and spin frequency.

I model neutron stars with masses between 1.0 and 2.5 $M_\odot$, radii between 8 and 16 km, and spin frequencies between 50 and 800 Hz over all possible inclinations. For each configuration, I produce a transfer function between the spectrum at the surface of the star and the spectrum an observer measures at a distant location, which I define below.

Photons are initialized on an image plane located in the asymptotically flat spacetime at a large radial distance from the neutron star. The photons are then traced backwards until they intersect the stellar surface. I record the position and energy of each photon on the surface and use these to find an image of the source on the image plane. I then integrate the specific intensity over this image in order to find the flux measured by an observer at spatial infinity as

$$F_\infty(E_\infty) = \frac{1}{D^2} \iint I_\infty(E_\infty, \alpha, \beta) \, d\alpha \, d\beta, \tag{6.1}$$

where E_∞ is the energy measured at infinity, D is the distance to the neutron star, I_∞

is the specific intensity measured at infinity, and α and β are Cartesian coordinates on the image plane (see Bauböck et al. 2012 for detailed definitions).

Since the quantity I/E^3 is Lorentz invariant, I can write

$$\frac{I_\infty(E_\infty)}{E_\infty^3} = \frac{I_s(E_s)}{E_s^3}, \tag{6.2}$$

where I_s and E_s are the specific intensity and energy, respectively, as measured on the surface of the neutron star. I assume uniform and isotropic emission over the surface of the star, i.e., that I_s does not depend on α and β. If I define

$$g(\alpha, \beta) \equiv E_\infty/E_s, \tag{6.3}$$

I can then write equation (6.1) as

$$F_\infty(E_\infty) = \frac{1}{D^2} \iint g^3 I_s\left(\frac{E_\infty}{g}\right) d\alpha \, d\beta. \tag{6.4}$$

My goal is to find a transfer function $G(E_\infty, E_s)$ such that I can write the flux at infinity as

$$F_\infty(E_\infty) = \int I_s(E_s) G(E_\infty, E_s) \, dE_s. \tag{6.5}$$

This allows me to understand the effects of rapid spin independent of the source spectrum. In order to convert equation (6.4) into this form, I need to translate the integral over the image plane into an integral over the energies on the stellar surface. I do this by introducing a Dirac delta function which is zero at all points on the image plane except at those where the energy on the surface E_s is equal to the energy at infinity E_∞ scaled by the factor g, $\delta(E_\infty/g - E_s)$. Since delta functions have the property that

$$\delta(ax) = \frac{1}{|a|}\delta(x), \tag{6.6}$$

I can rewrite this as

$$\delta\left(\frac{E_\infty}{g} - E_s\right) = g\delta(E_\infty - gE_s). \tag{6.7}$$

and equation (6.4) as

$$F_\infty(E_\infty) = \frac{1}{D^2} \iiint I_s(E_s) g^4 \delta(E_\infty - gE_s) \, dE_s \, d\alpha \, d\beta. \qquad (6.8)$$

By comparing equation (6.5) to equation (6.8), I find the transfer function

$$G(E_\infty, E_s) = \frac{1}{D^2} \iint g^4 \delta(E_\infty - gE_s) \, d\alpha \, d\beta. \qquad (6.9)$$

To calculate an observed spectrum for a given neutron-star configuration, I first calculate the transfer function $G(E_\infty, E_s)$ from Equation (6.9). I then use this function as a kernel for a convolution with the spectrum at the surface, as in Equation (6.5). In principle, the surface spectrum $I_s(E_s)$ can consist of a detailed atmospheric model, but for the purposes of this chapter I restrict my analysis to a blackbody function with an effective temperature T_s.

The top panel of Figure 6.1 shows the blackbody spectrum as measured in the rest-frame on the surface of the neutron star as a solid black curve. The spectrum measured by an observer at infinity for a star spinning at 700 Hz is shown as a solid red curve.

As expected, the spectrum at infinity is both broadened and shifted with respect to the surface spectrum and can no longer be represented by a blackbody. However, for the parameters of this calculation, the deviation from a blackbody spectrum is relatively small. In order to find the approximate blackbody temperature that would be measured at infinity, I fit a blackbody to the observed spectrum in two different ways. First, I locate the peak of the broadened spectrum and calculate the temperature and normalization of a blackbody with the same peak energy and flux. Second, I perform a fit to find the parameters of a blackbody with the minimum least-squares difference to the broadened spectrum over a range of energies. In order to capture the spectral broadening around the peak near 3 $k_B T_s$, I consider a range of energies between 0.04 and 12 $k_B T_s$. Changing the upper and lower energy bounds does not have a significant effect on my results. The dashed line in the upper panel in Figure 6.1 shows the latter fit, and the lower panel shows the residuals for both
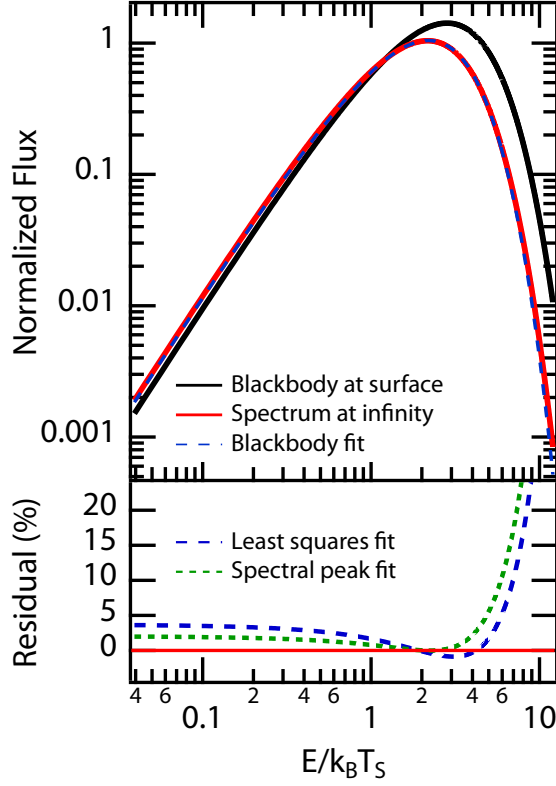
Figure 6.1: Broadened blackbody spectrum of temperature T_s emitted from the surface of a neutron star of mass 1.4 $M_\odot$ and radius 10 km, spinning at 700 Hz, as observed at an inclination of 85°. The x-axis shows photon energy scaled by $k_B T_s$. The surface spectrum has been normalized by a constant factor such that it has an integral of 1. The black solid line shows the blackbody spectrum of temperature T_s measured at the surface of the star. The red line shows the broadened spectrum measured at spatial infinity. The blue dashed line shows the best fit blackbody to the broadened spectrum found by a least-squares fitting algorithm in the energy range $0.04 \leq E/k_B T_s \leq 12$. The curve corresponding to a different fit that matches the energy and flux of the spectral peak is indistinguishable from the blue dashed line in the upper panel. The lower panel shows the residuals for both fits. In the observable range near the spectral peak, rotational effects introduce spectral distortions at the $\lesssim 5\%$ level. The large residual at higher energies is difficult to observe, since the flux at these energies is smaller by a factor of 10^{-3} than at the peak.

fitting methods. As the two procedures produce the same blackbody parameters to within a percent, I use only the least-squares method for the remainder of this work. The deviation of the spectrum at infinity from a blackbody varies from 3%–4% below the peak to ≥5% at higher energies. This is comparable to the measured deviation of observed spectra from blackbodies in X-ray bursters (Güver et al. 2012).

Both the measured flux and the blackbody temperature are used in inferring the masses and radii of thermally emitting neutron stars. When these inferences are made under the assumption of a non-rotating source, a systematic error is introduced in the measurements. For a non-spinning neutron star, the apparent spectroscopic radius R_∞ can be calculated from the measured flux F_∞ and temperature T_∞ using

$$F_\infty = \sigma \left(\frac{R_\infty}{D} \right)^2 T_\infty^4, \tag{6.10}$$

where D is the distance to the source, which I set to unity for the remainder of this work. In this case, the observed spectrum is a blackbody with a redshifted peak and diminished flux, both caused by the gravitational redshift from the stellar surface. In the Schwarzschild metric, both of these corrections can be calculated analytically. The peak of the spectrum (and, therefore, its inferred temperature) is redshifted by

$$\frac{T_\infty^{(f_{\mathrm{NS}}=0)}}{T_s} = \sqrt{1 - \frac{2GM}{Rc^2}}. \tag{6.11}$$

Likewise, I can find the bolometric flux at infinity by integrating the spectrum and use a similar expression to correct for the gravitational redshift and strong-field lensing, i.e.,

$$\frac{F_\infty^{(f_{\mathrm{NS}}=0)}}{F_s} = \left(1 - \frac{2GM}{Rc^2} \right), \tag{6.12}$$

where F_s is the flux measured on the surface. This will allow me to relate the spectroscopic radius observed at infinity to the circumferential radius of the star by

$$R = R_\infty \sqrt{1 - \frac{2GM}{Rc^2}}. \tag{6.13}$$

For a spinning neutron star, I can compare the values of the inferred temperature and flux to those derived under the assumption that the source is spherical and non-spinning in order to calculate correction factors introduced by the spin. In particular, I define the rotational temperature correction factor as

$$\zeta_{\rm rot} \equiv \frac{T_\infty}{T_\infty^{(f_{\rm NS}=0)}} = \frac{T_\infty}{T_s \sqrt{1 - \frac{2GM}{Rc^2}}}, \tag{6.14}$$

and the correction to the bolometric flux as

$$b_{\rm rot} \equiv \frac{F_\infty}{F_\infty^{(f_{\rm NS}=0)}} = \frac{F_\infty}{F_s \left(1 - \frac{2GM}{Rc^2}\right)}. \tag{6.15}$$

These correction factors quantify the bias in calculating the above quantities from an observed spectrum when it is assumed that the source is not rotating. Using Equations (6.14) and (6.15) I find that, for a spinning star, the inferred spectroscopic radius will be biased by a factor of

$$\frac{R_\infty}{R_\infty^{f_{\rm NS}=0}} = \sqrt{\frac{b_{\rm rot}}{\zeta_{\rm rot}^4}}. \tag{6.16}$$

6.3   Results

Figure 6.2 shows the bias $\zeta_{\rm rot}$ in the measured temperature as a result of the spin of the neutron star. The lines represent contours of constant rotational correction, as defined in Equation (6.14), for a range of possible spin frequencies $f_{\rm NS}$ and inclination angles θ_O. These corrections are small, at the 1% level, for both values of the neutron star radius shown in this figure. As the spin frequency approaches zero, the measured temperature approaches the value calculated in the Schwarzschild approximation, such that the correction factor becomes unity for all inclination angles.

The shape of the contours and whether the rotational correction factor is smaller or larger than unity for a set of parameters can be understood as follows. At high spin frequencies, Doppler shifts due to the velocity of the stellar surface become

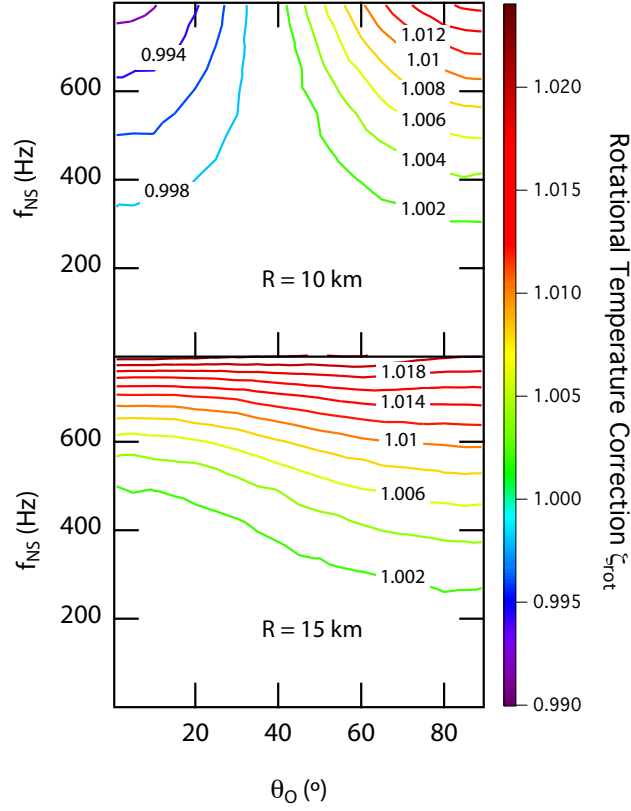Figure 6.2: Contours of constant rotational correction to temperature for a range of neutron-star spin frequencies (f_{NS}) and inclinations (θ_O). The correction to the temperature is defined as in Equation (6.14). The upper panel shows neutron stars with equatorial radii of 10 km, while the lower panel shows stars with 15 km radii. In both cases, the stars have a mass of 1.4 $M_\odot$.

significant, and the neutron star becomes oblate in shape. I can determine the effect of Doppler shifts by considering the photon energy E_∞ at infinity from a point on the stellar surface. Ignoring gravitational redshift, this energy is

$$E_\infty = \eta E_s, \tag{6.17}$$

where E_s is the photon energy at the surface and η is the Doppler function,

$$\eta = \frac{\sqrt{1 - (v/c)^2}}{1 - (v/c)\cos\xi}. \tag{6.18}$$

In this equation, v is the local magnitude of the velocity of a point on the stellar surface and ξ is the angle between the velocity vector and the direction of emission of the photon. The angle ξ is defined so that $\cos\xi$ is positive on the blueshifted side of the star and negative on the redshifted side. For small values of v, the Doppler factor can be approximated by

$$\eta \approx 1 + \frac{v}{c}\cos\xi + \left(\frac{v}{c}\right)^2 \left(\cos^2\xi - 0.5\right) + O\left[\left(\frac{v}{c}\right)^3\right]. \tag{6.19}$$

When the photon energies are averaged over the surface of the star, the first order term (as well as all higher odd powers of v/c) will cancel, leaving only the second order term. At high inclinations, $\cos\xi$ is large for most of the stellar surface, leading to a higher energy measured at infinity. At low inclinations, however, $\cos\xi$ is smaller than 0.5 for most of the surface, resulting in an average Doppler factor smaller than 1. Moreover, at low inclinations the oblate shape of the surface leads to a stronger gravitational redshift at the pole, further decreasing the inferred temperature.

The changes in the temperature also depend on the compactness of the neutron star. Stars with a smaller compactness (corresponding to a larger radius for a constant mass) have a larger quadrupole moment for a given spin frequency. For a 15 km star, the high quadrupole moment results in a smaller gravitational redshift near the pole, leading to a higher temperature for sources observed at low inclinations, as shown in the lower panel of Figure 6.2.
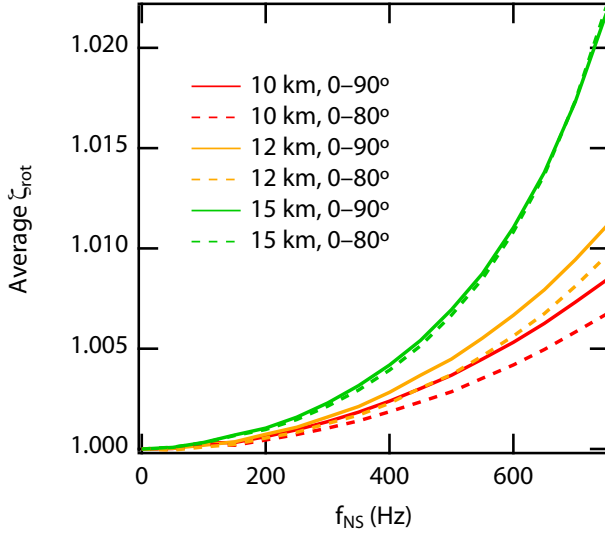
Figure 6.3: Rotational correction to the neutron-star temperature averaged over inclination. The plot shows the rotational correction to the temperature weighted by the sine of the inclination angle and averaged over a range of possible inclinations for a neutron star with a mass of 1.4 $M_\odot$ and three different radii. The solid lines show the correction averaged over inclinations from 0° (pole-on) to 90° (equatorial), while the dotted lines show the correction averaged between 0° and 80°. The largest radii lead to the largest corrections.

For most sources displaying thermal emission, the inclination of the spin axis to the observer's line of sight is not known. In Figure 6.3 I show the rotational correction to temperature as a function of spin frequency averaged over the inclination of the source assuming a random orientation of the observer. I choose two inclination ranges for these averages: from 0° (pole-on) to 90° (equatorial) and from 0° to 80°. I calculate the average over the latter range to take into account the possibility that an accretion disk may obscure the surface at high inclinations and, therefore, these objects would not be detected in a search for thermal emission. For both inclination ranges, the correction to the temperature due to the spin of the neutron star is less than 2% across the range of observed spin frequencies.

The different behavior of the lines in Figure 6.3 can be understood by an argument similar to the one presented above. For both the 10 km and 12 km neutron star, the dominant effect is the second-order Doppler shift, which increases the observed

temperature at high inclinations. Thus, when the highest inclinations are excluded from the average, as in the case of the dashed lines in Figure 6.3, the average correction decreases. For a 15 km star, however, the effect due to the quadrupole moment is comparable to the second order Doppler correction. In this case, the correction factor is greater than unity at all inclinations. Excluding the highest inclinations only negligibly affects the average temperature, as shown by the agreement of the dashed and solid lines for the 15 km case in Figure 6.3.

In Figure 6.4, I show the correction to the bolometric flux due to the neutron-star spin as defined in Equation (6.15). As before, the zeroth order gravitational redshift has been removed, and first order Doppler shift effects cancel when integrated over the surface. I find that b_{rot} is less than 1 across the parameter space, indicating that rapid rotation decreases the flux measured by an observer at infinity. The value of b_{rot} depends on several competing effects at second order in v/c: the second order terms of the Doppler shift, the oblate shape of the star, the quadrupole moment of the spacetime, and the frame dragging near the surface. I can first gain some insight into the relative magnitudes of these effects by calculating typical values for these corrections and how they scale with the neutron-star parameters.

I estimate the contributions of the Doppler shift by integrating Equation (6.17) for a spherical star in Newtonian gravity at an inclination of 90°,

$$\frac{\Delta E_\infty}{E_\infty} = \int_0^\pi \int_0^\pi \eta \, d\theta d\phi \tag{6.20}$$

I find that the average Doppler shift is

$$\frac{\Delta E_\infty^{\mathrm{Doppler}}}{E_\infty} \approx 0.004 \left(\frac{R_{\mathrm{eq}}}{10\,\mathrm{km}} \right)^2 \left(\frac{f_{\mathrm{NS}}}{600\,\mathrm{Hz}} \right)^2, \tag{6.21}$$

where R_{eq} is the equatorial radius.

Both the oblateness and the quadrupole moment affect the flux and temperature primarily by changing the gravitational redshift at different points on the surface. In the case of oblateness, I start from the Schwarzschild expression for the gravitational
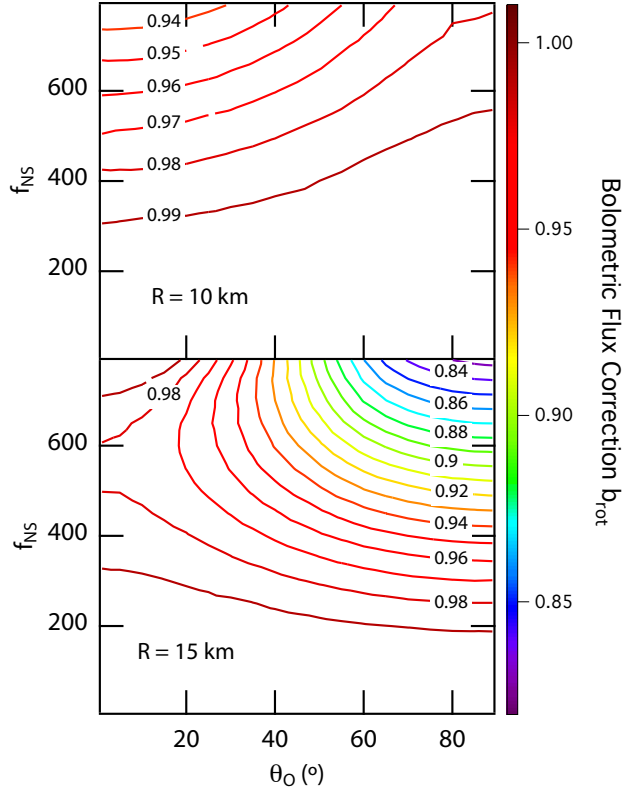
Figure 6.4: Contours of constant rotational correction to the bolometric flux for a range of neutron star spin frequencies $f_{\rm NS}$ and inclinations θ_O. The correction to the flux is defined as in Equation (6.15). The upper panel shows the result for a neutron star with a 10 km radius, while the lower panel shows a 15 km star. Both stars have a mass of 1.4 $M_\odot$.
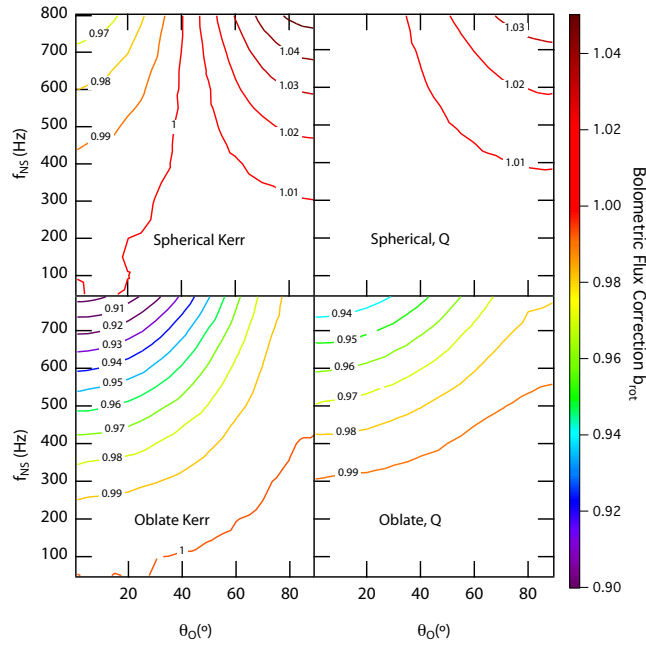
Figure 6.5: Contours of constant rotational correction to the bolometric flux for four different neutron-star configurations aiming to illustrate the effects of surface geometry and quadrupole moment. Each panel shows the result for neutron stars with a mass of 1.4 $M_\odot$ and a 10 km equatorial radius. The top left panel shows the result for a spherical neutron star in the Kerr metric. The top right panel shows the results for a spherical star with an appropriate quadrupole moment. The lower left panel corresponds to a star in the Kerr metric with an oblate surface. Finally, the lower right panel corresponds to a star in the Hartle-Thorne approximation, with an oblate surface and an appropriate quadrupole moment. The lower right panel is identical to the upper panel of Figure 6.4.

redshift

$$\frac{E_\infty}{E_s} = \sqrt{1 - \frac{GM}{R_{eq}c^2}}, \tag{6.22}$$

and estimate the difference in the polar and equatorial redshifts as

$$\frac{\Delta E_\infty^{Oblate}}{E_\infty} \approx -\frac{GM}{R_{eq}c^2}\left(1 - \frac{GM}{R_{eq}c^2}\right)^{-1}\left(1 - \frac{R_p}{R_{eq}}\right), \tag{6.23}$$

where R_p is the radius at the rotational pole. Using Equation (22) of Bauböck et al. (2013a), I find that

$$\frac{\Delta E_\infty^{Oblate}}{E_\infty} \approx -0.015\left(\frac{R_{eq}}{10\,km}\right)^2\left(\frac{f_{NS}}{600\,Hz}\right)^2. \tag{6.24}$$

Similarly, to estimate the effect of a non-zero quadrupole moment, I find the gravitational redshift at the poles and the equator using

$$\frac{E_\infty}{E_s} = \sqrt{g_{tt}}, \tag{6.25}$$

where g_{tt} is the tt-component of the metric. The exact form of g_{tt} can be found in Glampedakis & Babak (2006). Approximating the quadrupole moment with Equation (25) of Bauböck et al. (2013a), I find that

$$\frac{\Delta E_\infty^Q}{E_\infty} \approx 0.002\left(\frac{R_{eq}}{10\,km}\right)^2\left(\frac{f_{NS}}{600\,Hz}\right)^2. \tag{6.26}$$

Each of these effects introduce a bias in the flux and temperature measurements at second order in the spin frequency of the star. For most of the parameter space, the dominant effect is the oblateness, which tends to decrease the observed flux of the star. However, the actual contribution of each bias depends on the inclination of the observer and the gravitational lensing, which depends on M/R. Therefore, it is possible for different effects to dominate depending on the neutron-star mass, radius, and inclination. It should be noted that, although the effects calculated above are at or less than the 1% level, the bias in the flux depends on these factors to the fourth

power and can therefore be considerably larger.

In order to illustrate these effects, I calculated fluxes for several neutron-star configurations that emphasize different effects at second order. (Note that this is only for the purposes of delineating different effects; in reality, an oblate star would always have a non-zero quadrupole moment, etc.) Each of the four panels of Figure 6.5 shows the flux correction for a different neutron star configuration and for a range of spin frequencies and observer inclinations. The upper left panel shows the flux for a spherical neutron star in the Kerr metric. In this case, the only effects causing a change in the flux are frame dragging and higher order terms in the Doppler shift. I find that the frame dragging has a negligible effect on the flux. At low inclinations, the transverse Doppler shift causes the limbs of the neutron star to appear redder and, therefore, dimmer, causing the flux correction to be less than 1. At high inclinations, on the other hand, Doppler boosting causes the blueshifted side of the star to appear brighter than the redshifted side. Since the Doppler boost is second order in v/c, the decreased flux from the redshifted side does not cancel the increased flux from the blueshifted side of the star, leading to a flux correction greater than 1.

In the bottom left panel, I allow the surface of the neutron star to become oblate with increasing spin frequency while retaining the Kerr metric. Comparing this panel to the Kerr panel, I find that introducing oblateness decreases the measured flux at all spin frequencies and inclinations. At low inclinations, this is due to the additional redshift at the pole, which is deeper in the gravitational well (see Equation (6.24)). At high inclinations, the geometric size of the neutron star decreases as it becomes more oblate, also decreasing the measured flux (see Bauböck et al. 2013b).

The top right panel of Figure 6.5 shows a spherical star with a spacetime with a quadrupole moment that is appropriate for a spinning neutron star. Note that this is not a self-consistent calculation since the proper radius of the pole and the equator are not the same. However, I use it here only to isolate the effect of the spacetime quadrupole. Compared to the spherical star in the upper left panel, the quadrupole moment decreases the gravitational redshift at the poles while increasing it at the equator (see Equation (6.26)). Consequently, the flux increases for neutron
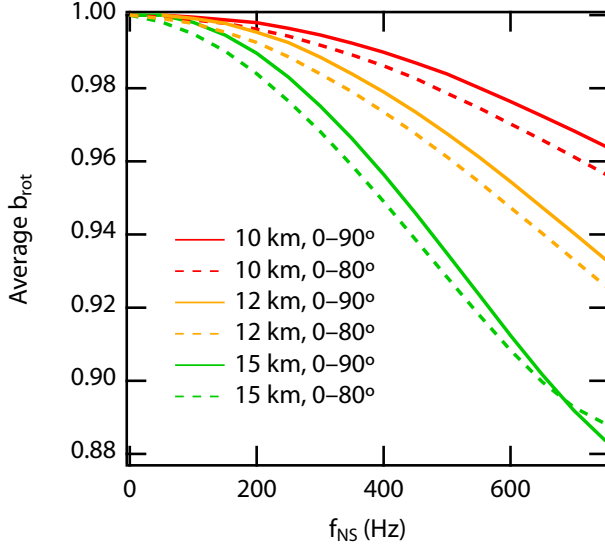
Figure 6.6: Rotational correction to the bolometric flux averaged over inclination. As in Figure 6.3, the three colored lines show the averaged correction for neutron stars with three different radii. Solid lines correspond to the correction averaged over 0°–90°, while dashed lines show the correction averaged over 0°–80°. In the case of a neutron star with a radius of 12 km, the solid and dashed lines are indistinguishable.

stars observed at low inclinations compared to the spherical Kerr case and decreases at high inclinations.

Finally, the lower right panel shows the combination of all the above mentioned effects. This panel shows an oblate star in the Hartle-Thorne metric and is identical to the upper panel of Figure 6.4. At low inclinations, the flux-decreasing effects of the oblate shape and transverse Doppler shift outweigh the decrease in redshift from the quadrupole moment, leading to a flux correction factor less than one. Similarly, at high inclinations the smaller area due to oblateness and the additional redshift due to the quadrupole moment outweigh the Doppler boost to cause a decrease in the flux. As expected from the order-of-magnitude estimates above, the dominant effect is that of stellar oblateness.

In Figure 6.6, I show the correction to the bolometric flux averaged over the inclination angle. As in Figure 6.3, I use two inclination ranges to account for possible obscuration of the source by an accretion disk. I find that the flux observed

from a neutron star spinning above 600 Hz is 2%–10% lower than for a non-spinning source. The largest flux corrections apply to neutron stars with the larger radii, which are more strongly modified by the second-order effects.

In general, excluding the highest inclination sources from the average leads to a smaller value of $b_{\rm rot}$ (i.e., a value that is further from unity). This is because in the high-inclination sources, the dominant effect is the second order Doppler shift, which tends to increase the value of $b_{\rm rot}$. Without these sources, the average flux correction factor decreases. For a radius as large as 15 km at a high spin frequency, the dominant effect at high inclination is the decrease in apparent area caused by the significantly oblate surface. Since the oblateness decreases the flux correction when viewed at high inclinations, excluding these high-inclination sources increases the value of $b_{\rm rot}$. This effect can be seen in the lower panel of Figure 6.4, in which the lowest values of flux correction occur at high inclination and high spin frequency.

6.4 Conclusions

I have shown that moderate spins have significant effects on the observed thermal spectra from neutron-star surfaces. At spin frequencies above 300 Hz, terms of second order in v/c can change observable quantities such as the flux and surface temperature. For moderately spinning stars, the temperature and flux measured by an observer at infinity is biased by factors related to the spin and the gravitational redshift of the stellar surface. Whether the inferred temperature is higher or lower than that of a non-spinning source depends on the parameters of the neutron star. However, I find that the magnitude of the bias is less than 2% across the parameter space. Increasing the spin of the source also results in a decrease in the flux observed at infinity. The magnitude of this decrease can be up to 12% for realistic neutron-star parameters. In general, neutron stars with larger radii experience stronger rotational effects and therefore have a decreased flux.

Given these biases, I can calculate how the correction to the flux and tempera-ture due to the rapid spin of the source translates into a correction on the radius measurement. In Figure 6.7, I show the apparent spectroscopic radius measured for
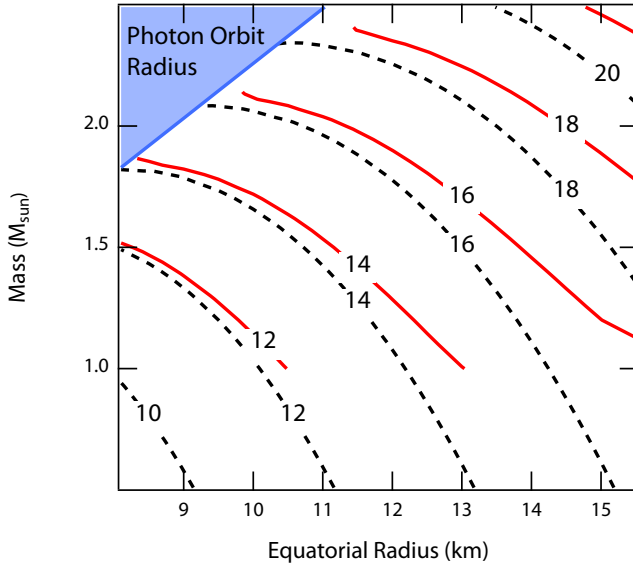
Figure 6.7: Contours of constant spectroscopic radius R_∞ plotted over the parameter space of equatorial radius and mass. The dashed lines are the contours for a non-spinning Schwarzschild star defined by Equation (6.13). The solid lines are the contours defined by Equation (6.16) for stars spinning at 600 Hz averaged over all inclination angles. The shaded region in the upper left corner corresponds to masses and radii for which the neutron star surface is within the photon orbit. Over the whole parameter space, a spinning star shows a smaller apparent radius than a non-spinning star for the same value of mass and equatorial radius.

a non-spinning star and one spinning at 600 Hz for a range of masses and radii. The dashed lines show the apparent radii for non-spinning stars in the Schwarzschild metric given in Equation (6.13). The solid lines correspond to sources spinning at 600 Hz and is given by Equation (6.16). The reduction in the flux that reaches the observer at infinity leads to a smaller apparent radius across the parameter space. In particular, assuming a non-spinning source leads to significant underestimation of the equatorial radius in the case of neutron stars with large radii and small masses.

Consider a star that spins at a frequency of 600 Hz and is known to have a mass of 1.4 $M_\odot$. If a measurement yields an apparent spectroscopic radius of 14 km and one uses the Schwarzschild approximation to calculate the equatorial radius, the dashed curve labeled 14 gives a value of 10.8 km. Using the solid curve which corrects for the effects of the spin yields an equatorial radius of 11.2 km. In this case, using the non-spinning approximation underestimates the radius by 3.5%.

Finally, I find an empirical formula to correct the bias introduced to radius measurements by the assumption that a source is non-spinning. I calculate the bolometric flux correction factor $b_{\rm rot}$ and temperature correction factor $\zeta_{\rm rot}$ for neutron stars with masses between 1.1 and 2.0 $M_\odot$ and radii between 10 and 15 km for all inclination angles and spin frequencies up to 800 Hz. As in Figures 6.3 and 6.6, I average these correction factors over inclination. Using Equation (6.16), I can then find the bias in the apparent radius inferred from the measured flux and temperature. The solid lines in the upper panel of Figure 6.8 show these correction factors. I calculate least-squares quadratic fits to the correction factor as a function of spin frequency for each neutron-star radius. Lastly, I fit the coefficients of this quadratic as a function of the radius to find a general equation for the spectroscopic radius correction,

$$
\frac{R_\infty^{f_{\rm NS}}}{R_\infty^{f_{\rm NS}=0}} = 1 + \left[\left(0.108 - 0.096\frac{M}{M_\odot} \right) + \right.
$$
$$
\left(-0.061 + 0.114\frac{M}{M_\odot} \right) \frac{R}{10\ \rm km} -
$$
$$
\left. 0.128 \left(\frac{R}{10\ \rm km} \right)^2 \right] \left(\frac{f_{\rm NS}}{1000\ \rm Hz} \right)^2 . \quad (6.27)
$$
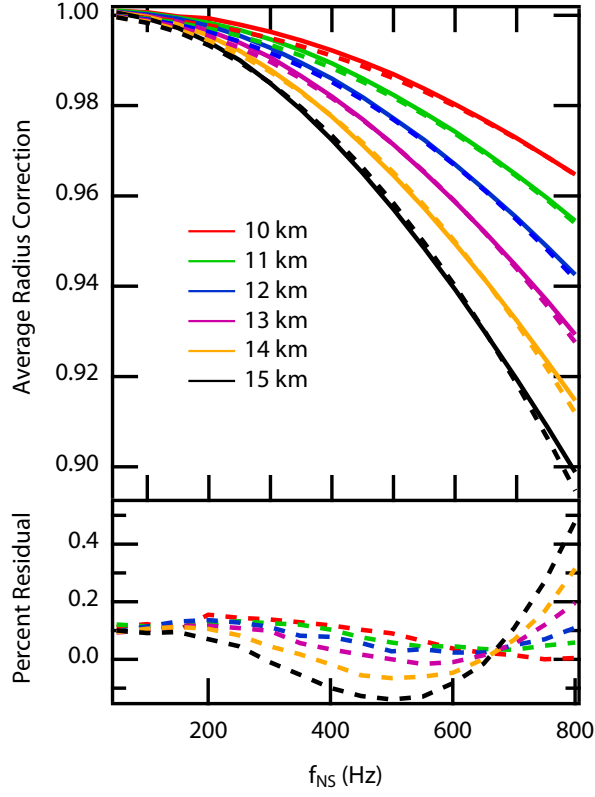
Figure 6.8: Rotational correction to the spectroscopically measured radii averaged over the inclination of the observer. The solid lines show the correction for different neutron-star radii, as in Figure 6.6. Dashed lines show empirical fits corresponding to Equation (6.27). The lower panel shows the percent residual in each fit.

The dashed lines in Figure 6.8 show this fit for 1.4 $M_\odot$ neutron stars with six chosen values of radius. The lower panel of Figure 6.8 shows the residuals to this fit. For neutron stars with radii between 10 and 15 km and masses between 1.1 and 2.0 $M_\odot$, I find that this fit approximates the numerical value of $R_\infty^{f_{\rm NS}}/R_\infty^{f_{\rm NS}=0}$ to within 0.5% for spin frequencies below 800 Hz.

These results have two important implications for the spectroscopic measurements of neutron-star masses and radii in X-ray bursters and quiescent sources. First, the distortion of the observed spectra from blackbodies are predicted to be at the $\simeq 5\%$ level. This is comparable to the spectral distortions caused by atmospheric effects (see, e.g. Suleimanov et al. 2012) and to the inferred deviation of the observed spectra in thermonuclear bursters from blackbodies (Güver et al. 2012). Second, the equatorial radii of neutron stars spinning at moderate rates inferred under the assumption that the stars are non-spinning are underestimated at a similar level. The bias depends on the spin and radius of the neutron star as well as on the observer's inclination but can be corrected with the formulae presented in this work.

CHAPTER 7

Effects of Spot Size on Neutron-Star Radius Measurements from Pulse Profiles

7.1   Masses and Radii from Pulse Profiles

Aside from observations of neutron star spectra, the other promising avenue for measuring masses and radii is via modeling pulse profiles from sources with brightness oscillations. Observations of such sources have already led to mass and radius constraints, and future missions such as *NICER* will provide constraints even tighter than those achieved by other methods.

In order to extract the mass and radius from the pulse profile shape, accurate theoretical models are needed that take account gravitational lensing, Doppler shifts, and time delays from the neutron-star surface. Several studies to date have focused on modeling pulse profiles in the Schwarzschild+Doppler approximation (e.g., Miller & Lamb 1998; Muno et al. 2002, 2003; Lamb et al. 2009a, b; Lo et al. 2013). Poutanen & Beloborodov (2006, see also Bogdanov et al. 2007) used this model to find analytic approximations for the photon lensing and time delays and constructed analytic lightcurves for neutron-star pulse profiles.

Braje et al. (2000) modeled pulse profiles in the Kerr metric and found that the distortion of the profile due to these effects is at the 1% level. Cadeau et al. (2007, see also Morsink et al. 2007) found that the oblateness of the stellar surface significantly alters the pulse profile, causing the spot to be visible at inclinations where it would be eclipsed by a spherical star. Psaltis & Özel (2014) used the Hartle-Thorne metric to model pulse profiles, including an appropriate quadrupole moment. Cadeau et al. (2007) modeled lightcurves for rapidly spinning neutron stars by calculating the metric numerically. They found that corrections from higher-order terms are negligible for the spin frequencies of known neutron stars.

The problem of modeling pulse profiles and, in turn, inferring neutron-star proper-
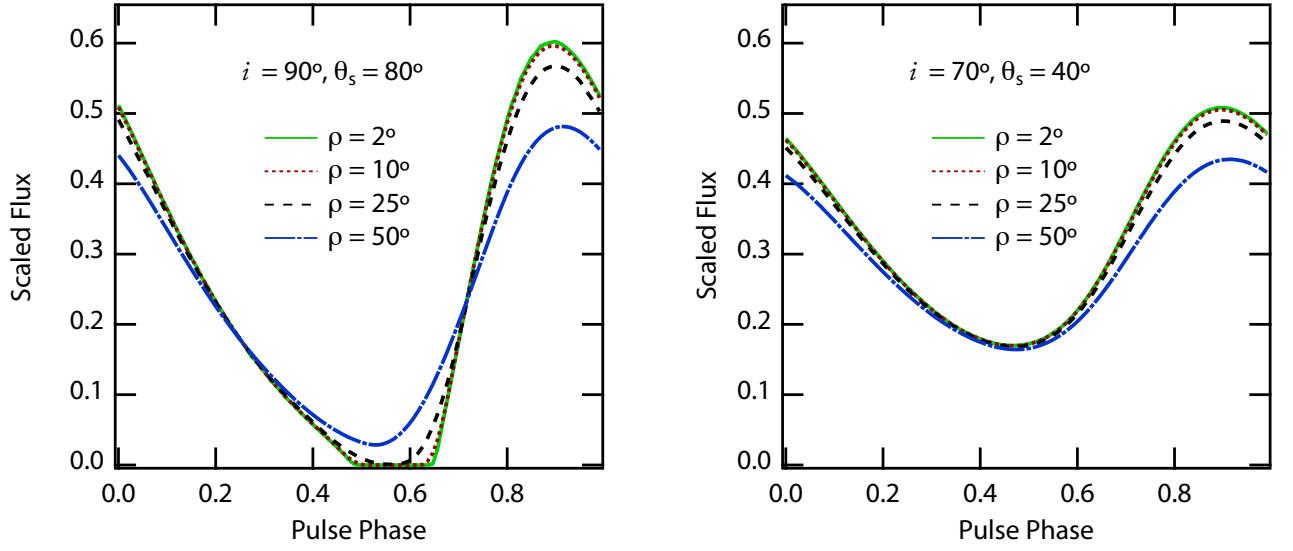
Figure 7.1: Example pulse profiles for two different spot configurations. In the left panel, the observer inclination is set to $i = 90°$ and the spot colatitude to $\theta_s = 80°$. In the right panel, they are set to $i = 70°$ and $\theta_s = 40°$. In both panels, the angular radius of the spot varies from $2°$ to $50°$. The flux has been scaled by $(50°/\rho)^2$ in order to remove the primary dependence of the flux on the spot area. In all cases, I have set $M = 1.6$ $M_\odot$, $R = 10$ km, and $f_{\rm NS} = 600$ Hz.

ties from pulse profiles, is difficult because of the large number of parameters needed. In principle, for any neutron-star model, the pulse profile depends on the properties of the neutron star as well as the size, shape, and position of the hotspot on the stellar surface. In order to simplify the models and reduce the parameter space, pulse profiles are often calculated under the assumption that the spot is infinitesimal in size. Lamb et al. (2009a, b; see also Psaltis et al. 2000) considered the effects of spot size on the amplitude of the pulse profile and found that the spot size has negligible effect as long as it is below $\sim 45°$. However, they did not consider the effect of the spot size on the higher harmonics of the profile, which are necessary for measuring the stellar radius.

In this chapter, I investigate the effect of spot size on pulse profiles for moderately spinning sources. Specifically, I determine the maximum spot size for which the spot can be considered small for the purpose of measuring the neutron-star radius. I then estimate the expected spot sizes as a function of spin frequency for rotation-powered and accretion-powered X-ray pulsars. In the case of X-ray burst oscillations, I find the fraction of the burst rise times during which a sufficient number of counts can be accumulated before the spot size becomes large enough to significantly bias the radius measurement from the pulse profile. I discuss the implications of these results for future missions that will observe pulse profiles, such as NICER and LOFT.

7.2   Pulse Profiles

I use the ray-tracing code described in Bauböck et al. (2012) and Psaltis & Özel (2014), which calculates pulse profiles using the Hartle-Thorne metric to approximate the spacetime around a moderately spinning neutron star. This metric is formally correct to second order in spin frequency and allows for the stellar surface to become oblate and the mass distribution to acquire an appropriate quadrupole moment. This algorithm also accounts for frame dragging around the star, time of flight delays, and Doppler shifts and aberration due to the motion of the stellar surface.

The propagation of photons to infinity depends on seven parameters of the neutron star: the mass, the equatorial radius, the spin frequency, the moment of inertia,

the oblateness, the quadrupole moment, and the inclination of the observer's line of sight to the spin axis. Of these, the mass, spin frequency, and inclination are independent and vary between different sources. The radius, oblateness, moment of inertia, and quadrupole moment of the star are determined, for a given spin, by the equation of state of the matter in its interior. (e.g., Baubök et al. 2013; Yagi & Yunes 2013). I use the relations described in Chapter 5 (see also Baubök et al. 2013; Yagi & Yunes 2013) to calculate the oblateness, moment of inertia, and quadrupole moment for a star with a given mass, radius, and spin frequency.

By using the universal relations described above, I reduce the number of parameters for each pulse profile to six: the mass and radius of the neutron star, the spin frequency, the inclination of the observer to the spin axis, and the colatitude and angular radius of the hotspot. For the simulations presented in this work, I fix the mass at 1.6 $M_\odot$, the radius at 10 km, and the spin frequency at 600 Hz. I calculate pulse profiles over the full range of observer inclinations i and spot colatitudes θ_s. I define the observer's inclination as the angle between the the observer's line of sight and the spin axis, such that $i = 0°$ and $i = 180°$ correspond to an observer directly over the north and south pole of the neutron star, respectively, while $i = 90°$ corresponds to an observer in the equatorial plane. I vary the colatitude of the spot θ_s, such that a spot on the pole has a colatitude $\theta_s = 0°$ and a spot on the equator corresponds to $\theta_s = 90°$.

Figure 7.1 shows several example pulse profiles for a variety of parameters. For all neutron-star configurations, the flux observed from the hotspot is proportional (to first order) to its area. In this figure, I have scaled the flux by this approximation to the spot area in order to highlight the more subtle changes in the profile shape introduced by increasing the spot size. In the left panel, the observer is in the equatorial plane of the neutron star, while the spot is near the equator. In this configuration, the spot is eclipsed behind the neutron star for a fraction of the spin period. As the spot grows in size, the duration of the eclipse decreases until the spot is visible at all phases.

The right panel of Figure 7.1 shows profiles for a smaller observer inclination and
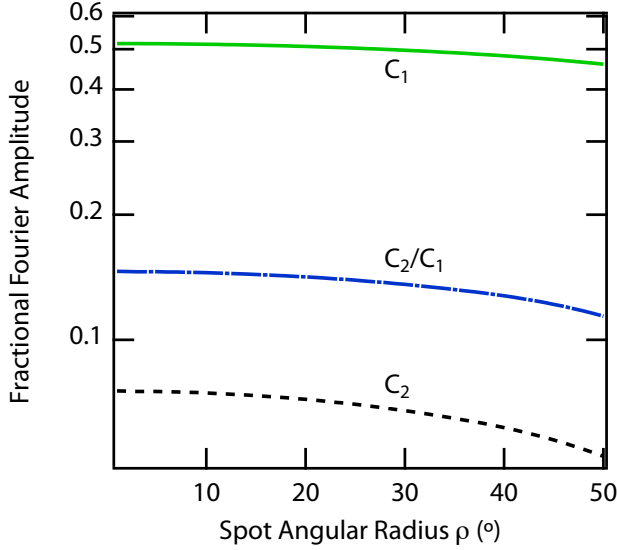
Figure 7.2: Fractional Fourier amplitudes of pulse profiles as a function of spot size. The observer inclination is $i = 70°$ and the spot colatitude is $\theta_s = 40°$. The remaining parameters are as in Figure 7.1. The solid and dotted lines show the first and second Fourier amplitudes, respectively. The dashed-dotted line shows the ratio between the two components.

spot colatitude. In this case, the spot is visible at all phases, regardless of its size. At larger angular radii, however, the amplitude of the profile still decreases. Moreover, the higher order harmonics also decrease, leading to a more symmetric and sinusoidal profile.

Since observations of neutron-star pulse profiles are usually limited by photon counts, information is often extracted by means of decomposing profiles into their Fourier components (Poutanen & Beloborodov 2006; Psaltis et al. 2014). The number of parameters of the neutron star and the hotspot that can be constrained increases with the number of Fourier components that can be measured from the lightcurve. I limit my analysis to realistic situations where the fundamental and the second harmonics can be measured in at least two energy bands.

As expected from the examples in Figure 7.1, in addition to encoding information about the neutron star itself and the location of the hotspot, the Fourier amplitudes of the pulse profiles also depend on the size of the hotspot. In particular, as the

size of the spot increases, the higher order harmonics are damped and the profile becomes more sinusoidal. In Figure 7.2, I show the amplitude of the first and second Fourier components, labeled C_1 and C_2 respectively, for a specific configuration of the observer inclination and the spot colatitude. For larger spot sizes, both the first and second harmonics decrease in amplitude. However, the second harmonic decreases more quickly than the first, causing the ratio between them to decrease also, as shown by the dashed-dotted line. This introduces a potential bias in the measurement of neutron-star radii, since the principal effect of a smaller radius is the reduction of the higher-order harmonics and, thereby, of the ratio C_2/C_1.

7.3 Biases in Radius Measurements

I wish to determine the extent to which the common assumption of an infinitesimally small spot is justified for the purpose of measuring the radius of a neutron star from its pulse profile. In order to quantify the effect of the spot size on measurements of the radius, I calculate profiles with a very small spot (with an angular radius $\rho = 2°$) and quantitatively compare these to profiles with larger spots. I find the maximum spot size for which the assumption that the spot is infinitesimally small is reasonable, i.e., leading to a radius bias that is less than 10%, allowing for meaningful constraints on the equation of state.

Using the relationships from Bauböck et al. (2013) for a neutron star of known spin frequency and the assumption that the hotspot is small, one can reduce the number of model parameters that need to be determined from the pulse profiles to four: the mass and radius of the neutron star, the colatitude of the hotspot, and the inclination of the observer. The number of observable quantities obtained from a pulse profile, on the other hand, depends to some extent on the relative inclinations of the observer and the spot to the spin axis of the neutron star. I will consider two cases: when the spot is visible for all phases, and when the spot becomes eclipsed behind the star for part of the spin period.

In the first case, I can measure the radius directly using the first two Fourier components of the pulse profiles at two broad energy ranges as the four required

observables (see discussion in Psaltis et al. 2014). All four observables carry information about the radius of the neutron star because Doppler shifts and aberration, which are proportional to the stellar radius, affect their values. Following Psaltis et al. (2014), I will use the ratio of amplitudes of the first two Fourier harmonics, which to leading order is proportional to the Doppler shift (see below), in order to quantify the effect of the spot size on the radius measurement.

The second case arises when both the hotspot and the observer are located near the stellar equator. Although the strong lensing of photons increases the fraction of the surface area visible to a distant observer, there is a region which is hidden from sight in this configuration. When the spot is in this region, none of its flux reaches the observer. This eclipse introduces sharp edges to the pulse profile and causes many higher harmonics to become large. However, the amplitudes of these higher order harmonics are not independent, as they are caused by the sharp eclipse. In practice, the eclipse introduces one additional measurable parameter, which is its duration. For a given spot colatitude and observer's inclination, a spot with a smaller radius will tend to have shorter eclipses, as the lensing is stronger and a smaller fraction of the stellar surface is hidden. However, a large hotspot can mimic the effects of a smaller radius. As the spot grows, the fraction of the profile during which it is completely hidden from the observer decreases. In this second case, I will determine the effect of the spot size on the eclipse duration in order to quantify the possible bias in radius measurements.

In order to estimate the error introduced in the radius measurement by a nonnegligible spot size, I use the relation between the radius and the ratio of the first and second harmonics (Psaltis et al. 2014)

$$\frac{C_2}{C_1} \approx \frac{4\pi f}{c} R \sin i \sin \theta_s. \tag{7.1}$$

This scaling was derived for a slowly spinning star in the Schwarzschild metric and is only expected to hold approximately for the most rapidly spinning stars. However, my purpose here is only to approximate the error in the radius measurement
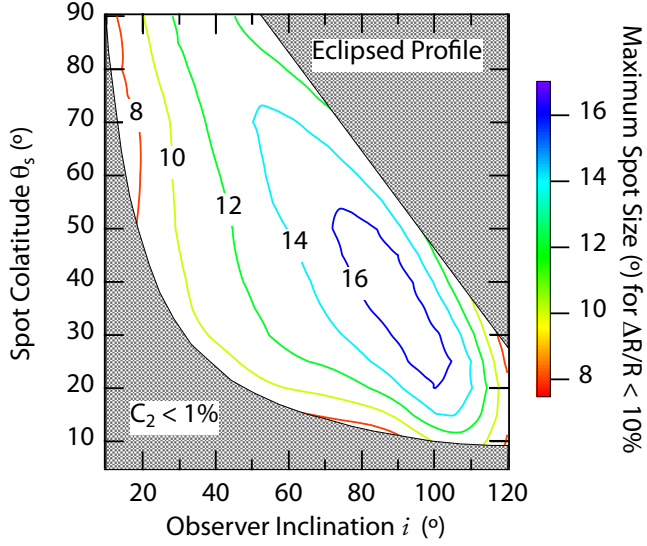
Figure 7.3: Maximum spot angular radius that leads to a $\leq10\%$ error in radius measurement as a function of the spot colatitude and observer inclination. If a radius measurement is made under the assumption of an infinitesimally small spot, the contours correspond to the spot size for which the measurement differs from the true neutron-star radius by ten percent.

introduced by large spot sizes, for which this expression is sufficient.

My goal is to calculate the maximum spot size at which the change introduced to the ratio C_2/C_1 due to the spot size is comparable to the difference introduced to this quantity by changing the radius by 10%. To determine this maximum size, I first calculate the change in the ratio C_2/C_1 as

$$\Delta\left(\frac{C_2}{C_1}\right) \approx 0.025 \left(\frac{\Delta R}{1 \text{ km}}\right)\left(\frac{f}{600 \text{ Hz}}\right)\sin i \sin\theta_s. \tag{7.2}$$

Next, I calculate the change in this ratio introduced by increasing the spot size. Specifically, for each pair of angles i and θ_s, I calculate a pulse profile and its Fourier components for a range of spot sizes between 2° and 50°. As the spot grows in size, there is an increasing change in the ratio C_2/C_1. Comparing the two, I find the largest spot size ρ for which this change is smaller than the error corresponding to a radius uncertainty of 10% given by equation (7.2).

The contours in Figure 7.3 show the spot size which corresponds to a maximum

error of 10% in radius. For most of the parameter space, I find that a spot size of up to 10°–18° introduces biases in the radius that are smaller than 10%. The maximum allowable size generally increases with increasing inclination and decreasing spot colatitude. This effect is primarily due to the $\sin i \sin \theta_s$ term in equation (7.2). For small angles i and θ_s, the change in the ratio C_2/C_1 for a 10% change in the neutron-star radius becomes very small, leading to a small allowed spot size.

The contours in Figure 7.3 are calculated for a 10 km star. For stars with larger radii, the maximum allowed spot size that leads to a 10% bias in the radius measurement is smaller. This is due to the larger tangential velocity of the neutron star surface for a given spin frequency. As the linear velocity increases, the differential Doppler boost from the near and far edges of the spot reduces the amplitude of the second harmonic of the pulse profile more than for a smaller star at the same spin frequency. This leads to a larger bias in the radius measurement and therefore a smaller maximum spot size.

The Doppler boost scales as the tangential velocity squared and thus as R^2. Therefore, the spot size that introduces a fixed absolute bias in the radius measurement scales to first order as $1/R^2$. In order to achieve a fractional accuracy of 10%, the maximum spot size scales as $1/R$.

The shaded parts of the parameter space in Figure 7.3 correspond to regions where my calculation of the maximum spot size is no longer valid or the measurement becomes unfeasible. In the lower region, corresponding to configurations where the observer and the spot are both near the rotational pole of the neutron star, the amplitude of the pulse profile is very small and the second harmonic is less than one percent. In the shaded region, the small amplitudes of pulse profiles make radius measurements of neutron stars unfeasible.

The upper shaded region in Figure 7.3 corresponds to the part of the parameter space where the spot is eclipsed for some fraction of the spin period. I focus on this region in Figure 7.4. The contours in the top panel of Figure 7.4 show the fraction of the profile during which the spot is eclipsed. Because of the strong lensing, the spot is hidden from view entirely for only a small portion of the parameter space,
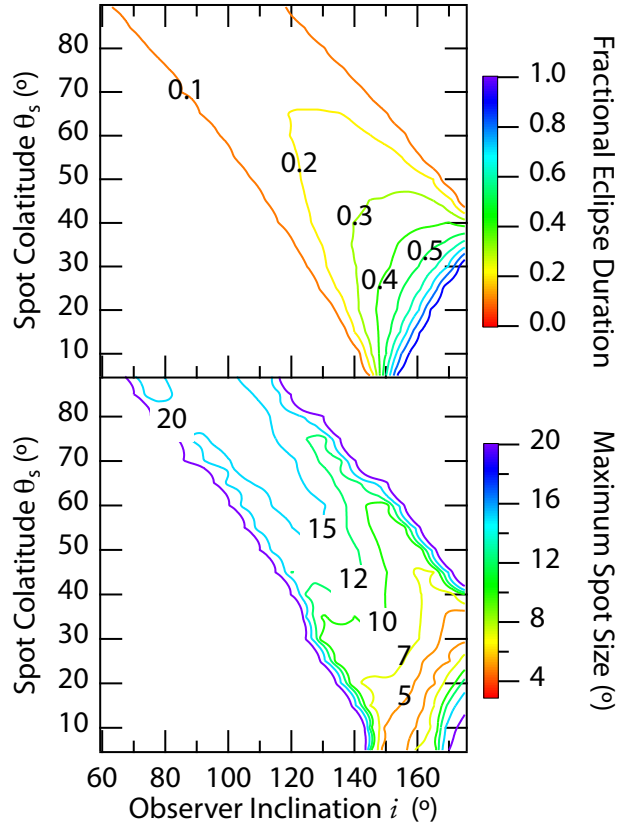
Figure 7.4: Region of the parameter space in which the spot is eclipsed for some fraction of the lightcurve. The upper panel shows the fractional duration of the eclipse for a 2° spot angular radius: zero corresponds to a spot that is visible at all phases, while one corresponds to a spot that is never visible. For larger spots, the eclipse duration decreases. The lower panel shows the spot angular radius at which the duration of the eclipse is shorter compared to the eclipse for a 2° spot by 0.1 of the period.

when the spot is near one pole and the observer's line of sight is near the other.

For the purpose of the top panel in Figure 7.4, I have set the spot size to $\rho = 2°$. As the spot grows in size, however, it spends less time completely hidden behind the star and the eclipse duration decreases. If I were to make the assumption that the spot was infinitesimal in size, this decrease in the eclipse duration would introduce a bias in the parameters derived from the eclipse. In the lower panel of Figure 7.4, the contours correspond to the spot size that introduces an error equal to 10% of the total period to the eclipse duration. Note that the unevenness in the contours is a result of the numerical uncertainty in the eclipse duration. The dominant source of this uncertainty is the phase resolution of the pulse profile, which is on the order of 1%. As in the case of no eclipses, spot sizes smaller than 15–20° introduce marginal biases to the measurements of the eclipse duration and, hence, of the neutron-star radius.

7.4   Sources

I now compare my spot size limits to realistic situations where pulse profiles will be used to measure neutron-star radii with upcoming missions such as NICER or LOFT. I consider three types of sources in which X-ray pulsations have been observed. In the case of rotation-powered and accreting millisecond pulsars, the precise size of the spot is unknown a priori but can be estimated using physical arguments. For X-ray bursters, the spot grows during the rise of the burst until it covers the entire surface of the star. In each case, I estimate the size of the hotspot depending on the specific parameters of the system.

In rotation-powered pulsars, hotspots on the surface are generated by magnetic return currents. To obtain a size estimate, I consider the simple scenario in which the hotspot corresponds to the footprint of the open field lines on the stellar surface (Sturrock 1971). Open field lines are defined as those which pass through the light cylinder radius R_{LC}. This is the radius at which a cylinder corotating with the
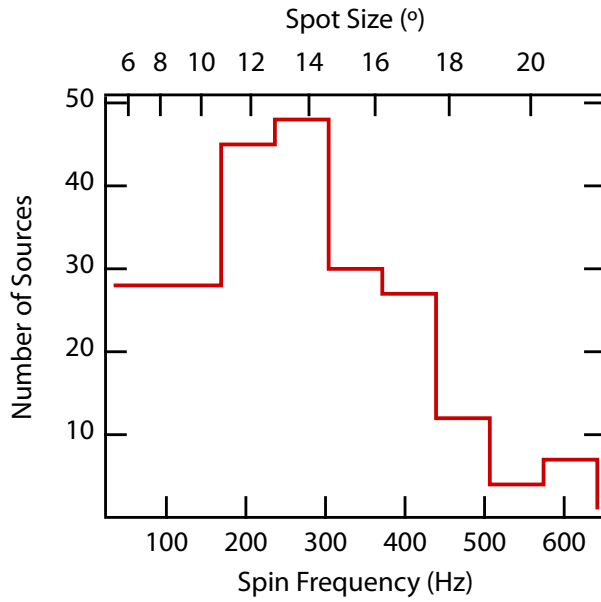
Figure 7.5: Histogram of the spin frequencies and the corresponding sizes of the polar caps of known rotation-powered millisecond pulsars. The lower axis shows the spin period, while the upper axis shows the spot size corresponding to equation (7.5).
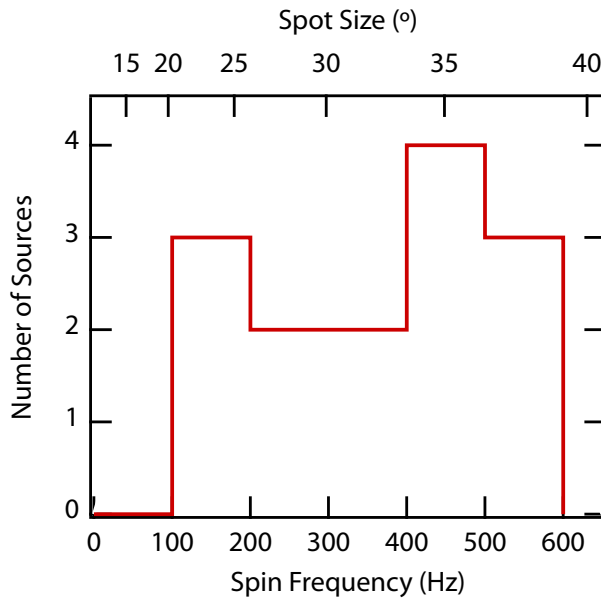
Figure 7.6: Histogram of accretion-powered X-ray pulsars from Watts (2012). As in Figure 7.5, the lower axis corresponds to the spin frequency, while the upper axis corresponds to the spot size derived from equation (7.7).

neutron star reaches the speed of light, i.e.,

$$R_{LC} \equiv \frac{c}{2\pi f_{\mathrm{NS}}},\tag{7.3}$$

where f_{NS} is the spin frequency of the neutron star. In a dipole magnetic field, the quantity $\sin^2\theta/r$, where θ is the polar angle, is constant along field lines, leading to

$$\frac{\sin^2\theta}{R} = \frac{\sin^2\theta_{\mathrm{NS}}}{R_{\mathrm{NS}}}.\tag{7.4}$$

The edge of the hotspot (where $\theta_{\mathrm{NS}} = \rho$) corresponds to the field line that reaches the light cylinder radius at the equator, where $\theta = 90°$. Therefore, I find the angular radius of the hotspot to be

$$\rho_{\mathrm{RPP}} = \sin^{-1}\left(\sqrt{\frac{2\pi f_{\mathrm{NS}} R_{\mathrm{NS}}}{c}}\right).\tag{7.5}$$

Figure 7.5 shows the spin the distribution of rotation-powered X-ray pulsars from the online catalog compiled by D. Lorimer[1]. The lower axis shows the spin period of the pulsar, while the upper axis shows the spot size from equation (7.5), assuming a 10 km neutron star. The peak of the distribution is near 300 Hz, corresponding to a spot size of 14°, and the majority of sources have spot sizes smaller than 18°. This implies that assuming that the hotspot on rotation-powered pulsars is infinitesimally small is a reasonable approximation for all but the most rapidly spinning sources.

In order to compare my analytical estimate with more detailed numerical simulations, I make use of the results of Bai & Spitkovsky (2010a, b), who modeled the size and shape of the polar cap region under more realistic vacuum dipole and force-free magnetosphere conditions. They found that the spot size can vary slightly from the value derived in equation (7.5), especially for neutron stars in which the magnetic pole is misaligned from the spin axis. Moreover, they found that the spot is not circular in shape. For spots smaller than the limits I derived above, I expect the spot shape to be unimportant to the pulse profile. For larger spots, further investigation

[1]http://astro.phys.wvu.edu/GalacticMSPs/GalacticMSPs.txt
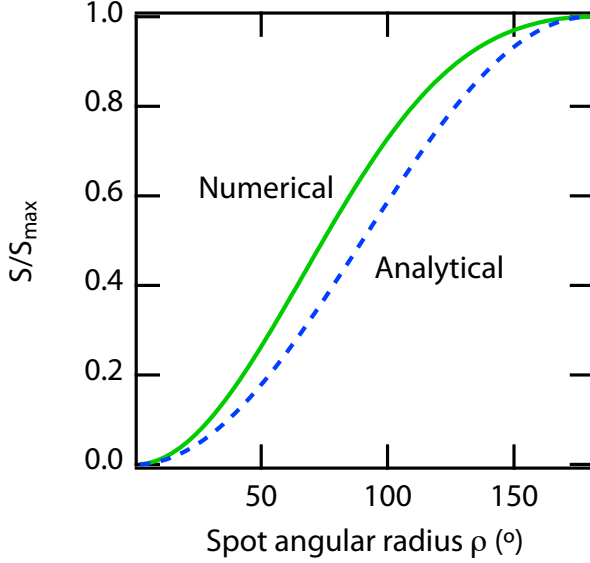
Figure 7.7: Apparent area of a hotspot averaged over the pulse profile as a function of the spot size. The analytical curve corresponds to equation (7.9). For the numerical curve, I have chosen a spot colatitude and observer inclination of $i = \theta_s = 45°$. For both curves, I have normalized the result by the apparent area of the whole neutron star such that $S(\rho = 180°)$ is equal to one.

is needed to find the effect of non-circular spots on the shape of the pulse profiles.

In accreting sources, matter is funneled from the disk onto the stellar surface along magnetic field lines. I will approximate the radius at which matter is transferred onto the magnetic field as the corotation radius R_c, i.e. the radius where a test mass in Keplerian orbit is corotating with the neutron star. In this case, it is straightforward to calculate the mass loading radius,

$$R_c \equiv \left(\frac{GM}{4\pi^2 f_{\mathrm{NS}}^2} \right)^{1/3}$$

$$\approx 2.46 \left(\frac{R}{10 \ \mathrm{km}} \right)^{-1} \left(\frac{M}{1.6 \ \mathrm{M_\odot}} \right)^{1/3} \left(\frac{f_{\mathrm{NS}}}{600 \ \mathrm{Hz}} \right)^{-2/3}. \quad (7.6)$$

Using equation (7.4), I can again find the size of the hotspot as

$$\rho_{\mathrm{AMXP}} = \sin^{-1} \left(\sqrt{\frac{4\pi^2 R f_{\mathrm{NS}}}{GM}} \right). \quad (7.7)$$

In Figure 7.6, I show the histogram of the spin frequencies of accreting millisecond pulsars from Watts (2012). As in Figure 7.5, the lower axis shows the spin frequency, while the upper axis corresponds to the spot size derived from equation (7.7). Here, I assume a neutron-star radius of 10 km and a mass of 1.4 $M_\odot$ as before. As Figure 7.6 shows, the majority of accretion-powered pulsars have hotspots that are significantly larger than the maximum size I calculate above. Therefore, their pulse profiles will be significantly affected by the spot sizes and consequently by the spot shapes. Further study is needed to determine how to extract radius measurements from these sources.

The last class of sources I consider are X-ray bursters that show oscillations during the burst rise. In this case, the hotspot on the surface arises from the relatively slow spreading of the thermonuclear burning across the stellar surface. Therefore, during the rise, the spot size changes with time and the amplitude of pulsations decreases (see Strohmayer et al. 1996). I estimate here the fraction of the burst oscillations for which I can assume that the spot is infinitesimal without introducing a large bias to the radius measurement.

Assuming that the spot size increases linearly during the burst rise from a point at $t = 0$ to a spot covering the entire surface ($\rho = 180°$) at the burst maximum, I write the angular radius as a function of time,

$$\rho(t) = \frac{\pi t}{t_R},\tag{7.8}$$

where t_R is the rise time of the burst. This equation is formally valid only when the photon diffusion time from the burning layer to the photosphere is smaller than the lateral propagation time of the burning front such that the rise time of the burst is dominated by the lateral spreading. Nevertheless, for the purposes of my estimates here, I will use this approximation to calculate the time before the spot reaches some maximum size ρ_{max}.

In the Newtonian case, I could calculate the emitting area on the stellar surface analytically,

$$S_{\text{spot}}^{\text{Newton}} = \int_0^\rho 2\pi R_{\text{NS}}^2 \sin \rho' \, d\rho' = 2\pi R_{\text{NS}}^2 (1 - \cos \rho).\tag{7.9}$$

However, this does not take into account the lensing of the spot, which distorts its size and shape and increases the fraction of the stellar surface that is visible to a distant observer or the effects of phase averaging. I numerically calculate the average emitting area of the spot over all phases as in Psaltis et al. (2000). Figure 7.7 shows the emitting area as a function of the spot size for a configuration where the spot colatitude and the inclination to the observer are both 45°. The analytic expression derived in equation (7.9) is shown in the dashed line. As expected in this configuration, the analytic approximation underestimates the average flux, since gravitational lensing tends to increase the apparent surface area.

Converting this surface area into a countrate depends on the specifics of the spectrum emitted from the hotspot and the detector used. Since I am primarily interested in an approximate estimate of the time needed to constrain the radius, I assume that the hotspot emits a blackbody spectrum at a temperature of 2 keV. The detected flux then depends only on the angular size of the source, which I encode in the blackbody normalization A, in units of $(km/10~kpc)^2$. The countrate also depends on the detector efficiency, which I encode in the quantity C that measures the number of photons detected from a 2 keV blackbody with an angular size of $(1~km/10~kpc)^2$. Then the countrate that will be observed for a spot of a given size becomes

$$\frac{\text{counts}}{\text{second}} = \frac{S_{\text{spot}}}{S_{\text{max}}} AC, \tag{7.10}$$

where S_{max} is the apparent area of the whole star. I find the total number of counts for a given burst by numerically integrating equation (7.10) from 0 to ρ_{max}. In order to estimate total number of photons N for a typical spot location and observer inclination, I set ρ_{max} to 15° and C to 2700 counts s^{-1} (10 kpc/km)^2 (for the LOFT Large Area Detector, T. Güver 2015, private communication) and find

$$N = 2.64At_R. \tag{7.11}$$

The number of counts necessary to measure the radius to 10% depends on the magnitude of the Fourier components as well as the geometry of the hotspot and the

spin frequency of the neutron star. Psaltis et al. (2014) found that the number of counts necessary to constrain the radius to 10% is approximately

$$N \approx 4.7 \cdot 10^4 \left(\frac{C_1}{0.38}\right)^2 \left(\frac{f_{\mathrm{NS}}}{600}\right)^2 \left(\frac{R_{\mathrm{NS}}}{10 \text{ km}}\right)^2$$

$$\left(\frac{\sin i}{0.71}\right)^2 \left(\frac{\sin \theta_s}{0.71}\right)^2, \quad (7.12)$$

which is consistent with numerical simulations by Lo et al. (2013). Here, I have set $i = \theta_s = 45°$ as above. For this configuration, I also find the first Fourier harmonic C_1 to have a fractional amplitude of 0.38 for a spot size of $\rho = 2°$.

I now combine equation (7.11) with equation (7.12) to find the number of individual bursts which must be added to measure the radius to a 10% accuracy. If I further know the burst rate, r_b, and the fraction of bursts showing oscillations during their rise, f_o, I can calculate the observing time necessary for each source as

$$t_{10\%} = \frac{1.79 \cdot 10^4}{A t_R} r_b f_o. \quad (7.13)$$

Table 7.1: Source Parameters

Name	$f_{\rm NS}$ [a] (Hz)	A [b] (km/10 kpc)^2	t_R [c] (s)	r_b [d] (h^{-1})	f_o [e]	$N_{\rm osc}$ [f]	$N_{\rm bursts}$ [g]	$t_{10\%}$ [h]
EXO 0748-646	552	114.0	4.9	0.24	0.02	38	1900	27.1
4U 1608-52	620	324.6	3.0	0.07	0.13	17	131	7.0
4U 1636-53	581	124.6	2.6	0.22	0.11	59	536	8.7
4U 1702-429	329	164.6	1.0	0.13	0.26	359	1381	39.0
4U 1728-34	363	121.6	1.0	0.20	0.10	400	4000	69.3
KS 1731-260	524	88.4	1.1	0.20	0.37	73	197	35.6

Notes.
[a] Spin frequency
[b] Blackbody normalization
[c] Average rise time
[d] Burst rate
[e] Fraction of bursts with oscillations in the rise
[f] Number of bursts with oscillations needed to constrain $R_{\rm NS}$ to within 10%
[g] Total number of bursts needed to constrain $R_{\rm NS}$ to within 10%
[h] Observing time needed to constrain $R_{\rm NS}$ to within 10%

Parameters for several bursting sources that show oscillations during the rise time.

I present in Table 7.1 the parameters for several bursting sources for which oscillations were detected during the rise time with the *Rossi X-ray Timing Explorer* (*RXTE*). Here, I use the burst rise times, the burst frequency, and the fraction of bursts with oscillations from Galloway et al. (2008). I use the blackbody normalization A from Güver et al. (2012) for sources 4U 1728-34, 4U 1702-429, KS 1731-260, and 4U 1636-53, from Özel (2006) for EXO 0748-676, and from Güver et al. (2010) for 4U 1608-52. I have chosen only the sources for which the spin frequency and blackbody normalization are known. In Figure 7.8, I show the time needed to reach an accuracy of 10% in measuring the radius versus the spin frequency for these sources.

It is evident from Figure 7.8 that sources with higher spin rates in general allow for better constraints to the radius. This is because a faster spin leads to stronger Doppler effects, causing the pulse profile to become more asymmetric. This results in
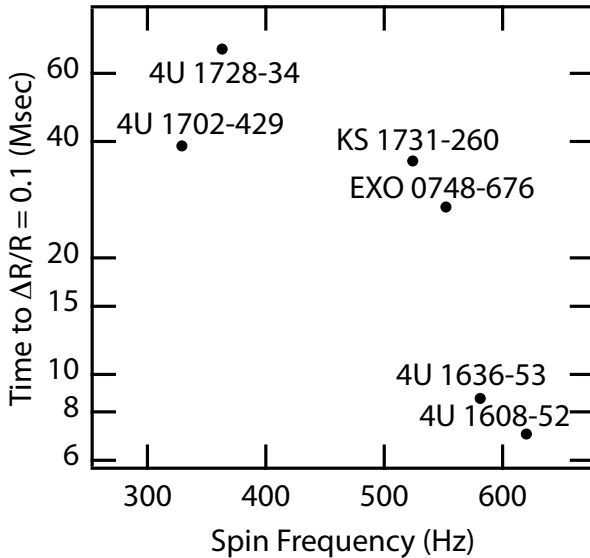
Figure 7.8: Time needed to achieve a 10% accuracy in the measurement of neutron-star radii using rise-time burst oscillations for several representative X-ray bursters, plotted against their spin frequencies.

an increase in the higher Fourier harmonics and thereby an increase in the accuracy of the radius measurement.

In the preceding estimate, I used the fraction of bursts with rise-time oscillations as inferred from *RXTE* observations. Using a future timing instrument with a larger collecting area such as LOFT will allow searching for burst oscillations during smaller time segments in the rise of the bursts. This increased sensitivity will most likely reveal oscillations in bursts in which the spreading time is short compared to the typical duration of the *RXTE* time segments or the location of the ignition of the bursts gives rise to smaller amplitude oscillations. Those bursts, however, will not add an appreciable number of counts to the integrated pulse profiles that will be used for measuring neutron star radii.

7.5   Conclusions

In this chapter, I focused on the problem of deriving neutron star parameters by modeling pulse profiles from hotspots on the stellar surface. In particular, I addressed

an often made assumption that the spot size can be treated to be infinitesimal in size and investigated the conditions under which this leads to errors that can be tolerated. I calculated the maximum size for which the hotspot can be considered to be infinitesimal, both for derivations of the radius from the Fourier components of the profile and for profiles which include an eclipse.

I found that hotspots with angular radius smaller than $10°$–$18°$ produce profiles that are not significantly different from those with very small hotspots. The maximum allowed spot size that corresponds to a 10% error in the derived radius depends on both the location of the spot and the inclination of the neutron star spin axis to the observer's line of sight. In general, increasing the inclination and decreasing the colatitude lead to a larger allowed spot sizes.

Similarly, I found that the duration of eclipses is relatively insensitive to the size of the hotspot if it is below $10°$–$20°$. In this case, increasing observer inclination and decreasing spot colatitude lead to a smaller maximum spot size. Nevertheless, for some extreme regions of the parameter space, even a spot smaller than $5°$ can have an eclipse duration that is significantly smaller than that of an infinitesimal spot.

Finally, I considered the implications of spot size limits for the upcoming NICER and the planned LOFT missions. I showed that, for rotation-powered millisecond X-ray pulsars, the majority of sources are expected to have spot sizes smaller than the limits derived above. For accretion-powered pulsars, I expect only the most slowly spinning sources to have hotspots small enough that the spot size can be neglected. For X-ray bursters, I calculated the fraction of the burst rise-time for which the spot is small enough to constrain the radius to within 10%. I found that, for two sources (4U 1636-53 and 4U 1608-52), it is possible to measure the radius to a 10% accuracy within a time of 7–9 Ms. Other sources with less optimal configurations require longer observations of 20–40 Ms in order to accurately measure their radii.

In this appendix I calculate the Newtonian surface area of the neutron star as a function of the inclination angle. Qualitatively, I am calculating the area of the shadow cast by the neutron star onto the image plane in the presence of light rays normal to the image plane. The outline of this figure is defined by the points on the neutron star at which a normal to the image plane is tangent to its surface.

To find this locus of points, I first write a parametric expression for a vector from the origin to a point on the surface of the neutron star with coordinates (θ,ϕ) in the usual form:

$$\mathbf{R}(\theta, \phi) = \{R(\theta)\sin(\theta)\cos(\phi), R(\theta)\sin(\theta)\sin(\phi), R(\theta)\cos(\theta)\}, \tag{A14}$$

with $R(\theta)$ defined as in Equation (3.2). I then define a normal vector to the surface at (θ,ϕ) as

$$\mathbf{N}(\theta, \phi) = \frac{\partial \mathbf{R}}{\partial \theta} \times \frac{\partial \mathbf{R}}{\partial \phi}, \tag{A15}$$

and a unit vector normal to the image plane at an angle θ_0 to the rotational axis of the neutron star as $\mathbf{V}(\theta_0) = \{0, \sin(\theta_0), \cos(\theta_0)\}$. As θ_0 varies from 0 to $\frac{\pi}{2}$, the inclination of the image plane ranges from pole-on to edge-on.

The boundary of the projection onto the image plane is defined by those points on the stellar surface which satisfy the equation

$$\mathbf{N}(\theta, \phi) \cdot \mathbf{V}(\theta_0) = 0. \tag{A16}$$

This equation is linear in $\sin(\phi)$ and has the solution

$$\sin(\phi) = -\frac{\cos(\theta)\cot(\theta_0)R(\theta) + \cot(\theta_0)\sin(\theta)R'(\theta)}{R(\theta)\sin(\theta) - \cos(\theta)R'(\theta)}. \tag{A17}$$

This equation is no longer valid in the limiting cases $\theta = \frac{\pi}{2}$ and $\theta = 0$. In the former case, the outline of the neutron star is described by Equation (3.2). In the latter case, when the observer lies along the rotational axis of the star, the outline will of course appear as a circle with radius $R(\frac{\pi}{2})$. It should also be noted that not all values of colatitude θ will correspond to a physical solution for the azimuth ϕ—the projected

circumference of the image will lie within a range of θ around the equator. I denote by θ_+ and θ_- the limits of colatitude that contribute to the image at infinity.

In order to project the resulting outline of the neutron star onto the image plane, I simply rotate the coordinate system by an angle $-\theta_0$ so the x–y plane is parallel to the image plane. I then set the z-component of all the points on the outline to zero to find a two-dimensional parametric form $\{C_x(\theta; \theta_0), C_y(\theta; \theta_0)\}$ of the outline of the projected image. Finally, I numerically integrate this curve to find the projected surface area:

$$A = 2 \int_{\theta_-}^{\theta_+} C_x \frac{dC_y}{d\theta} d\theta. \tag{A18}$$

REFERENCES

Abramowicz, M. A., G. J. E. Almergren, W. Kluzniak, and A. V. Thampan (2003). The Hartle-Thorne circular geodesics. *ArXiv General Relativity and Quantum Cosmology e-prints.*

AlGendy, M. and S. M. Morsink (2014). Universality of the Acceleration due to Gravity on the Surface of a Rapidly Rotating Neutron Star. *ApJ*, **791**, 78. doi: 10.1088/0004-637X/791/2/78.

Andersson, N. and K. D. Kokkotas (1998). Towards gravitational wave asteroseismology. *MNRAS*, **299**, pp. 1059–1068. doi:10.1046/j.1365-8711.1998.01840.x.

Antoniadis, J., P. C. C. Freire, N. Wex, T. M. Tauris, R. S. Lynch, M. H. van Kerkwijk, M. Kramer, C. Bassa, V. S. Dhillon, T. Driebe, J. W. T. Hessels, V. M. Kaspi, V. I. Kondratiev, N. Langer, T. R. Marsh, M. A. McLaughlin, T. T. Pennucci, S. M. Ransom, I. H. Stairs, J. van Leeuwen, J. P. W. Verbiest, and D. G. Whelan (2013). A Massive Pulsar in a Compact Relativistic Binary. *Science*, **340**, p. 448. doi:10.1126/science.1233232.

Arons, J. (1981). Pair creation above pulsar polar caps - Steady flow in the surface acceleration zone and polar CAP X-ray emission. *ApJ*, **248**, pp. 1099–1116. doi: 10.1086/159239.

Arzoumanian, Z., K. C. Gendreau, C. L. Baker, T. Cazeau, P. Hestnes, J. W. Kellogg, S. J. Kenyon, R. P. Kozon, K.-C. Liu, S. S. Manthripragada, C. B. Markwardt, A. L. Mitchell, J. W. Mitchell, C. A. Monroe, T. Okajima, S. E. Pollard, D. F. Powers, B. J. Savadkin, L. B. Winternitz, P. T. Chen, M. R. Wright, R. Foster, G. Prigozhin, R. Remillard, and J. Doty (2014). The neutron star interior composition explorer (NICER): mission definition. In *Space Telescopes and Instrumentation 2014: Ultraviolet to Gamma Ray*, volume 9144 of *Proc. SPIE*, p. 914420. doi:10.1117/12.2056811.

Asaoka, I. and R. Hoshi (1987). Energy spectrum at infinity emitted from a rapidly rotating neutron star. *PASJ*, **39**, pp. 475–484.

Bai, X.-N. and A. Spitkovsky (2010a). Modeling of Gamma-ray Pulsar Light Curves Using the Force-free Magnetic Field. *ApJ*, **715**, pp. 1282–1301. doi:10.1088/0004-637X/715/2/1282.

Bai, X.-N. and A. Spitkovsky (2010b). Uncertainties of Modeling Gamma-ray Pulsar Light Curves Using Vacuum Dipole Magnetic Field. *ApJ*, **715**, pp. 1270–1281. doi: 10.1088/0004-637X/715/2/1270.

Bauböck, M., E. Berti, D. Psaltis, and F. Özel (2013a). Relations between Neutron-star Parameters in the Hartle-Thorne Approximation. *ApJ*, **777**, 68. doi:10.1088/0004-637X/777/1/68.

Bauböck, M., D. Psaltis, and F. Özel (2013b). Narrow Atomic Features from Rapidly Spinning Neutron Stars. *ApJ*, **766**, 87. doi:10.1088/0004-637X/766/2/87.

Bauböck, M., D. Psaltis, F. Özel, and T. Johannsen (2012). A Ray-tracing Algorithm for Spinning Compact Object Spacetimes with Arbitrary Quadrupole Moments. II. Neutron Stars. *ApJ*, **753**, 175. doi:10.1088/0004-637X/753/2/175.

Berti, E. and N. Stergioulas (2004). Approximate matching of analytic and numerical solutions for rapidly rotating neutron stars. *MNRAS*, **350**, pp. 1416–1430. doi:10.1111/j.1365-2966.2004.07740.x.

Berti, E., F. White, A. Maniopoulou, and M. Bruni (2005). Rotating neutron stars: an invariant comparison of approximate and numerical space-time models. *MNRAS*, **358**, pp. 923–938. doi:10.1111/j.1365-2966.2005.08812.x.

Bhattacharyya, S., M. C. Miller, and F. K. Lamb (2006). The Shapes of Atomic Lines from the Surfaces of Weakly Magnetic Rotating Neutron Stars and Their Implications. *ApJ*, **644**, pp. 1085–1089. doi:10.1086/503860.

Bildsten, L. (1995). Propagation of nuclear burning fronts on accreting neutron stars: X-ray bursts and sub-hertz noise. *ApJ*, **438**, pp. 852–875. doi:10.1086/175128.

Bogdanov, S., J. E. Grindlay, and G. B. Rybicki (2008). Thermal X-Rays from Millisecond Pulsars: Constraining the Fundamental Properties of Neutron Stars. *ApJ*, **689**, 407-415. doi:10.1086/592341.

Bogdanov, S., G. B. Rybicki, and J. E. Grindlay (2007). Constraints on Neutron Star Properties from X-Ray Observations of Millisecond Pulsars. *ApJ*, **670**, pp. 668–676. doi:10.1086/520793.

Braje, T. M., R. W. Romani, and K. P. Rauch (2000). Light Curves of Rapidly Rotating Neutron Stars. *ApJ*, **531**, pp. 447–452. doi:10.1086/308448.

Brown, D. A., I. Harry, A. Lundgren, and A. H. Nitz (2012). Detecting binary neutron star systems with spin in advanced gravitational-wave detectors. *Phys. Rev. D*, **86**, p. 084017. doi:10.1103/PhysRevD.86.084017.

Burgay, M., N. D'Amico, A. Possenti, R. N. Manchester, A. G. Lyne, B. C. Joshi, M. A. McLaughlin, M. Kramer, J. M. Sarkissian, F. Camilo, V. Kalogera, C. Kim, and D. R. Lorimer (2003). An increased estimate of the merger rate of double neutron stars from observations of a highly relativistic system. *Nature*, **426**, pp. 531–533. doi:10.1038/nature02124.

Cadeau, C., D. A. Leahy, and S. M. Morsink (2005). Pulse Shapes from Rapidly Rotating Neutron Stars: Equatorial Photon Orbits. *ApJ*, **618**, pp. 451–462. doi: 10.1086/425857.

Cadeau, C., S. M. Morsink, D. Leahy, and S. S. Campbell (2007). Light Curves for Rapidly Rotating Neutron Stars. *ApJ*, **654**, pp. 458–469. doi:10.1086/509103.

Catuneanu, A., C. O. Heinke, G. R. Sivakoff, W. C. G. Ho, and M. Servillat (2013). Mass/radius Constraints on the Quiescent Neutron Star in M13 Using Hydrogen and Helium Atmospheres. *ApJ*, **764**, 145. doi:10.1088/0004-637X/764/2/145.

Chang, P., S. Morsink, L. Bildsten, and I. Wasserman (2006). Rotational Broadening of Atomic Spectral Features from Neutron Stars. *ApJ*, **636**, pp. L117–L120. doi: 10.1086/499428.

Cook, G. B., S. L. Shapiro, and S. A. Teukolsky (1994). Rapidly rotating polytropes in general relativity. *ApJ*, **422**, pp. 227–242. doi:10.1086/173721.

Cottam, J., F. Paerels, and M. Mendez (2002). Gravitationally redshifted absorption lines in the X-ray burst spectra of a neutron star. *Nature*, **420**, pp. 51–54. doi: 10.1038/nature01159.

Cottam, J., F. Paerels, M. Méndez, L. Boirin, W. H. G. Lewin, E. Kuulkers, and J. M. Miller (2008). The Burst Spectra of EXO 0748-676 during a Long 2003 XMM-Newton Observation. *ApJ*, **672**, 504-509. doi:10.1086/524186.

Demorest, P. B., T. Pennucci, S. M. Ransom, M. S. E. Roberts, and J. W. T. Hessels (2010). A two-solar-mass neutron star measured using Shapiro delay. *Nature*, **467**, pp. 1081–1083. doi:10.1038/nature09466.

Drake, J. J., H. L. Marshall, S. Dreizler, P. E. Freeman, A. Fruscione, M. Juda, V. Kashyap, F. Nicastro, D. O. Pease, B. J. Wargelin, and K. Werner (2002). Is RX J1856.5-3754 a Quark Star? *ApJ*, **572**, pp. 996–1001. doi:10.1086/340368.

Ferdman, R. D., I. H. Stairs, M. Kramer, R. N. Manchester, A. G. Lyne, R. P. Breton, M. A. McLaughlin, A. Possenti, and M. Burgay (2008). The double pulsar: evolutionary constraints from the system geometry. In Bassa, C., Z. Wang, A. Cumming, and V. M. Kaspi (eds.) *40 Years of Pulsars: Millisecond Pulsars, Magnetars and More*, volume 983 of *American Institute of Physics Conference Series*, pp. 474–478. doi:10.1063/1.2900277.

Frank, J., A. King, and D. J. Raine (2002). *Accretion Power in Astrophysics: Third Edition*.

Fu, A. and R. E. Taam (1990). The spectra of weakly magnetized neutron stars. *ApJ*, **353**, pp. 205–214. doi:10.1086/168608.

Galloway, D. K., J. Lin, D. Chakrabarty, and J. M. Hartman (2010). Discovery of a 552 Hz Burst Oscillation in the Low-Mass X-Ray Binary EXO 0748-676. *ApJ*, **711**, pp. L148–L151. doi:10.1088/2041-8205/711/2/L148.

Galloway, D. K., M. P. Muno, J. M. Hartman, D. Psaltis, and D. Chakrabarty (2008). Thermonuclear (Type I) X-Ray Bursts Observed by the Rossi X-Ray Timing Explorer. *ApJS*, **179**, 360-422. doi:10.1086/592044.

Glampedakis, K. and S. Babak (2006). Mapping spacetimes with LISA: inspiral of a test body in a 'quasi-Kerr' field. *Classical and Quantum Gravity*, **23**, pp. 4167–4188. doi:10.1088/0264-9381/23/12/013.

Guillot, S., R. E. Rutledge, and E. F. Brown (2011). Neutron Star Radius Measurement with the Quiescent Low-mass X-ray Binary U24 in NGC 6397. *ApJ*, **732**, 88. doi:10.1088/0004-637X/732/2/88.

Guillot, S., M. Servillat, N. A. Webb, and R. E. Rutledge (2013). Measurement of the Radius of Neutron Stars with High Signal-to-noise Quiescent Low-mass X-Ray Binaries in Globular Clusters. *ApJ*, **772**, 7. doi:10.1088/0004-637X/772/1/7.

Güver, T. and F. Özel (2013). The Mass and the Radius of the Neutron Star in the Transient Low-mass X-Ray Binary SAX J1748.9-2021. *ApJ*, **765**, L1. doi:10.1088/2041-8205/765/1/L1.

Güver, T., F. Özel, A. Cabrera-Lavers, and P. Wroblewski (2010a). The Distance, Mass, and Radius of the Neutron Star in 4U 1608-52. *ApJ*, **712**, pp. 964–973. doi:10.1088/0004-637X/712/2/964.

Güver, T., F. Özel, and D. Psaltis (2012a). Systematic Uncertainties in the Spectroscopic Measurements of Neutron-star Masses and Radii from Thermonuclear X-Ray Bursts. II. Eddington Limit. *ApJ*, **747**, 77. doi:10.1088/0004-637X/747/1/77.

Güver, T., D. Psaltis, and F. Özel (2012b). Systematic Uncertainties in the Spectroscopic Measurements of Neutron-star Masses and Radii from Thermonuclear X-Ray Bursts. I. Apparent Radii. *ApJ*, **747**, 76. doi:10.1088/0004-637X/747/1/76.

Güver, T., P. Wroblewski, L. Camarota, and F. Özel (2010b). The Mass and Radius of the Neutron Star in 4U 1820-30. *ApJ*, **719**, pp. 1807–1812. doi:10.1088/0004-637X/719/2/1807.

Harding, A. K. and A. G. Muslimov (2001). Pulsar Polar Cap Heating and Surface Thermal X-Ray Emission. I. Curvature Radiation Pair Fronts. *ApJ*, **556**, pp. 987–1001. doi:10.1086/321589.

Harding, A. K. and A. G. Muslimov (2002). Pulsar Polar Cap Heating and Surface Thermal X-Ray Emission. II. Inverse Compton Radiation Pair Fronts. *ApJ*, **568**, pp. 862–877. doi:10.1086/338985.

Hartle, J. B. (1967). Slowly Rotating Relativistic Stars. I. Equations of Structure. *ApJ*, **150**, p. 1005. doi:10.1086/149400.

Hartle, J. B. and K. S. Thorne (1968). Slowly Rotating Relativistic Stars. II. Models for Neutron Stars and Supermassive Stars. *ApJ*, **153**, p. 807. doi:10.1086/149707.

Heinke, C. O., H. N. Cohn, P. M. Lugger, N. A. Webb, W. C. G. Ho, J. Anderson, S. Campana, S. Bogdanov, D. Haggard, A. M. Cool, and J. E. Grindlay (2014). Improved mass and radius constraints for quiescent neutron stars in ω Cen and NGC 6397. *MNRAS*, **444**, pp. 443–456. doi:10.1093/mnras/stu1449.

Heinke, C. O., G. B. Rybicki, R. Narayan, and J. E. Grindlay (2006). A Hydrogen Atmosphere Spectral Model Applied to the Neutron Star X7 in the Globular Cluster 47 Tucanae. *ApJ*, **644**, pp. 1090–1103. doi:10.1086/503701.

Hessels, J. W. T., S. M. Ransom, I. H. Stairs, P. C. C. Freire, V. M. Kaspi, and F. Camilo (2006). A Radio Pulsar Spinning at 716 Hz. *Science*, **311**, pp. 1901–1904. doi:10.1126/science.1123430.

Johannsen, T. and D. Psaltis (2010). Testing the No-hair Theorem with Observations in the Electromagnetic Spectrum. II. Black Hole Images. *ApJ*, **718**, pp. 446–454. doi:10.1088/0004-637X/718/1/446.

Kerr, R. P. (1963). Gravitational Field of a Spinning Mass as an Example of Algebraically Special Metrics. *Physical Review Letters*, **11**, pp. 237–238. doi: 10.1103/PhysRevLett.11.237.

Laarakkers, W. G. and E. Poisson (1999). Quadrupole Moments of Rotating Neutron Stars. *ApJ*, **512**, pp. 282–287. doi:10.1086/306732.

Lamb, F. K., S. Boutloukos, S. Van Wassenhove, R. T. Chamberlain, K. H. Lo, A. Clare, W. Yu, and M. C. Miller (2009a). A Model for the Waveform Behavior of Accreting Millisecond X-Ray Pulsars: Nearly Aligned Magnetic Fields and Moving Emission Regions. *ApJ*, **706**, pp. 417–435. doi:10.1088/0004-637X/706/1/417.

Lamb, F. K., S. Boutloukos, S. Van Wassenhove, R. T. Chamberlain, K. H. Lo, and M. C. Miller (2009b). Origin of Intermittent Accretion-Powered X-ray Oscillations in Neutron Stars with Millisecond Spin Periods. *ApJ*, **705**, pp. L36–L39. doi: 10.1088/0004-637X/705/1/L36.

Lattimer, J. M. (2012). The Nuclear Equation of State and Neutron Star Masses. *Annual Review of Nuclear and Particle Science*, **62**, pp. 485–515. doi:10.1146/annurev-nucl-102711-095018.

Lattimer, J. M. and M. Prakash (2001). Neutron Star Structure and the Equation of State. *ApJ*, **550**, pp. 426–442. doi:10.1086/319702.

Lattimer, J. M. and M. Prakash (2007). Neutron star observations: Prognosis for equation of state constraints. *Phys. Rep.*, **442**, pp. 109–165. doi:10.1016/j.physrep.2007.02.003.

Lewin, W. H. G. and P. C. Joss (1977). X-ray burst sources. *Nature*, **270**, pp. 211–216. doi:10.1038/270211a0.

Lin, J., F. Özel, D. Chakrabarty, and D. Psaltis (2010). The Incompatibility of Rapid Rotation with Narrow Photospheric X-ray Lines in EXO 0748-676. *ApJ*, **723**, pp. 1053–1056. doi:10.1088/0004-637X/723/2/1053.

Lindblom, L. (1992). Determining the nuclear equation of state from neutron-star masses and radii. *ApJ*, **398**, pp. 569–573. doi:10.1086/171882.

Lo, K. H., M. C. Miller, S. Bhattacharyya, and F. K. Lamb (2013). Determining Neutron Star Masses and Radii Using Energy-resolved Waveforms of X-Ray Burst Oscillations. *ApJ*, **776**, 19. doi:10.1088/0004-637X/776/1/19.

Lo, K.-W. and L.-M. Lin (2011). The Spin Parameter of Uniformly Rotating Compact Stars. *ApJ*, **728**, 12. doi:10.1088/0004-637X/728/1/12.

London, R. A., R. E. Taam, and W. M. Howard (1986). Model atmospheres for X-ray bursting neutron stars. *ApJ*, **306**, pp. 170–182. doi:10.1086/164330.

Lorimer, D. R. (2001). Binary and Millisecond Pulsars at the New Millennium. *Living Reviews in Relativity*, **4**.

Madej, J., P. C. Joss, and A. Różańska (2004). Model Atmospheres and X-Ray Spectra of Bursting Neutron Stars: Hydrogen-Helium Comptonized Spectra. *ApJ*, **602**, pp. 904–912. doi:10.1086/379761.

Majczyna, A. and J. Madej (2005). Mass and Radius Determination for the Neutron Star in X-ray Burst Source 4U/MXB 1728-34. *Act. Astron.*, **55**, pp. 349–366.

Mandel, I. and R. O'Shaughnessy (2010). Compact binary coalescences in the band of ground-based gravitational-wave detectors. *Classical and Quantum Gravity*, **27**(11), 114007. doi:10.1088/0264-9381/27/11/114007.

Manko, V. S., E. W. Mielke, and J. D. Sanabria-Gómez (2000a). Exact solution for the exterior field of a rotating neutron star. *Phys. Rev. D*, **61**(8), 081501. doi:10.1103/PhysRevD.61.081501.

Manko, V. S., J. D. Sanabria-Gómez, and O. V. Manko (2000b). Nine-parameter electrovac metric involving rational functions. *Phys. Rev. D*, **62**(4), 044048. doi:10.1103/PhysRevD.62.044048.

Miller, M. C. and F. K. Lamb (1998). Bounds on the Compactness of Neutron Stars from Brightness Oscillations during X-Ray Bursts. *ApJ*, **499**, pp. L37–L40. doi:10.1086/311335.

Morsink, S. M., D. A. Leahy, C. Cadeau, and J. Braga (2007). The Oblate Schwarzschild Approximation for Light Curves of Rapidly Rotating Neutron Stars. *ApJ*, **663**, pp. 1244–1251. doi:10.1086/518648.

Muno, M. P., F. Özel, and D. Chakrabarty (2002). The Amplitude Evolution and Harmonic Content of Millisecond Oscillations in Thermonuclear X-Ray Bursts. *ApJ*, **581**, pp. 550–561. doi:10.1086/344152.

Muno, M. P., F. Özel, and D. Chakrabarty (2003). The Energy Dependence of Millisecond Oscillations in Thermonuclear X-Ray Bursts. *ApJ*, **595**, pp. 1066–1076. doi:10.1086/377447.

Özel, F. (2006). Soft equations of state for neutron-star matter ruled out by EXO 0748 - 676. *Nature*, **441**, pp. 1115–1117. doi:10.1038/nature04858.

Özel, F. (2013). Surface emission from neutron stars and implications for the physics of their interiors. *Reports on Progress in Physics*, **76**(1), 016901. doi:10.1088/0034-4885/76/1/016901.

Özel, F., G. Baym, and T. Güver (2010). Astrophysical measurement of the equation of state of neutron star matter. *Phys. Rev. D*, **82**(10), 101301. doi:10.1103/PhysRevD.82.101301.

Özel, F. and P. Freire (2016). Masses, Radii, and Equation of State of Neutron Stars. *ArXiv e-prints*.

Özel, F., T. Güver, and D. Psaltis (2009). The Mass and Radius of the Neutron Star in EXO 1745-248. *ApJ*, **693**, pp. 1775–1779. doi:10.1088/0004-637X/693/2/1775.

Özel, F. and D. Psaltis (2003). Spectral Lines from Rotating Neutron Stars. *ApJ*, **582**, pp. L31–L34. doi:10.1086/346197.

Özel, F. and D. Psaltis (2009). Reconstructing the neutron-star equation of state from astrophysical measurements. *Phys. Rev. D*, **80**(10), 103003. doi:10.1103/PhysRevD.80.103003.

Özel, F., D. Psaltis, R. Narayan, and A. Santos Villarreal (2012). On the Mass Distribution and Birth Masses of Neutron Stars. *ApJ*, **757**, 55. doi:10.1088/0004-637X/757/1/55.

Pappas, G. and T. A. Apostolatos (2012). Revising the Multipole Moments of Numerical Spacetimes and its Consequences. *Physical Review Letters*, **108**(23), 231104. doi:10.1103/PhysRevLett.108.231104.

Pechenick, K. R., C. Ftaclas, and J. M. Cohen (1983). Hot spots on neutron stars - The near-field gravitational lens. *ApJ*, **274**, pp. 846–857. doi:10.1086/161498.

Poisson, E. (1998). Gravitational waves from inspiraling compact binaries: The quadrupole-moment term. *Phys. Rev. D*, **57**, pp. 5287–5290. doi:10.1103/PhysRevD.57.5287.

Pons, J. A., F. M. Walter, J. M. Lattimer, M. Prakash, R. Neuhäuser, and P. An (2002). Toward a Mass and Radius Determination of the Nearby Isolated Neutron Star RX J185635-3754. *ApJ*, **564**, pp. 981–1006. doi:10.1086/324296.

Poutanen, J. and A. M. Beloborodov (2006). Pulse profiles of millisecond pulsars and their Fourier amplitudes. *MNRAS*, **373**, pp. 836–844. doi:10.1111/j.1365-2966.2006.11088.x.

Poutanen, J. and M. Gierliński (2003). On the nature of the X-ray emission from the accreting millisecond pulsar SAX J1808.4-3658. *MNRAS*, **343**, pp. 1301–1311. doi:10.1046/j.1365-8711.2003.06773.x.

Poutanen, J., J. Nättilä, J. J. E. Kajava, O.-M. Latvala, D. K. Galloway, E. Kuulkers, and V. F. Suleimanov (2014). The effect of accretion on the measurement of neutron star mass and radius in the low-mass X-ray binary 4U 1608-52. *MNRAS*, **442**, pp. 3777–3790. doi:10.1093/mnras/stu1139.

Psaltis, D. (2008a). Probes and Tests of Strong-Field Gravity with Observations in the Electromagnetic Spectrum. *Living Reviews in Relativity*, **11**. doi:10.12942/lrr-2008-9.

Psaltis, D. (2008b). Testing general metric theories of gravity with bursting neutron stars. *Phys. Rev. D*, **77**(6), 064006. doi:10.1103/PhysRevD.77.064006.

Psaltis, D. and T. Johannsen (2012). A Ray-tracing Algorithm for Spinning Compact Object Spacetimes with Arbitrary Quadrupole Moments. I. Quasi-Kerr Black Holes. *ApJ*, **745**, 1. doi:10.1088/0004-637X/745/1/1.

Psaltis, D. and F. Özel (2014). Pulse Profiles from Spinning Neutron Stars in the Hartle-Thorne Approximation. *ApJ*, **792**, 87. doi:10.1088/0004-637X/792/2/87.

Psaltis, D., F. Özel, and D. Chakrabarty (2014). Prospects for Measuring Neutron-star Masses and Radii with X-Ray Pulse Profile Modeling. *ApJ*, **787**, 136. doi: 10.1088/0004-637X/787/2/136.

Psaltis, D., F. Özel, and S. DeDeo (2000). Photon Propagation around Compact Objects and the Inferred Properties of Thermally Emitting Neutron Stars. *ApJ*, **544**, pp. 390–396. doi:10.1086/317208.

Racine, É. (2008). Analysis of spin precession in binary black hole systems including quadrupole-monopole interaction. *Phys. Rev. D*, **78**(4), 044021. doi: 10.1103/PhysRevD.78.044021.

Raithel, C. A., F. Özel, and D. Psaltis (2016). Model-independent inference of neutron star radii from moment of inertia measurements. *Phys. Rev. C*, **93**(3), 032801. doi:10.1103/PhysRevC.93.032801.

Ravenhall, D. G. and C. J. Pethick (1994). Neutron star moments of inertia. *ApJ*, **424**, pp. 846–851. doi:10.1086/173935.

Read, J. S., B. D. Lackey, B. J. Owen, and J. L. Friedman (2009). Constraints on a phenomenologically parametrized neutron-star equation of state. *Phys. Rev. D*, **79**(12), 124032. doi:10.1103/PhysRevD.79.124032.

Reissner, H. (1916). Über die Eigengravitation des elektrischen Feldes nach der Einsteinschen Theorie. *Annalen der Physik*, **355**, pp. 106–120.

Ruderman, M. A. and P. G. Sutherland (1975). Theory of pulsars - Polar caps, sparks, and coherent microwave radiation. *ApJ*, **196**, pp. 51–72. doi:10.1086/153393.

Rutledge, R. E., L. Bildsten, E. F. Brown, G. G. Pavlov, and V. E. Zavlin (2001). Quiescent Thermal Emission from the Neutron Star in Aquila X-1. *ApJ*, **559**, pp. 1054–1059. doi:10.1086/322361.

Schoelkopf, R. J. and R. L. Kelley (1991). Detection of coherent 7.6 HZ oscillations during a burst from Aquila X-1. *ApJ*, **375**, pp. 696–700. doi:10.1086/170234.

Schwarzschild, K. (1916). Über das Gravitationsfeld eines Massenpunktes nach der Einsteinschen Theorie. *Sitzungsberichte der Königlich Preußischen Akademie der Wissenschaften (Berlin), 1916, Seite 189-196.*

Shibata, M. and M. Sasaki (1998). Innermost stable circular orbits around relativistic rotating stars. *Phys. Rev. D*, **58**(10), 104011. doi:10.1103/PhysRevD.58.104011.

Steiner, A. W., J. M. Lattimer, and E. F. Brown (2010). The Equation of State from Observed Masses and Radii of Neutron Stars. *ApJ*, **722**, pp. 33–54. doi: 10.1088/0004-637X/722/1/33.

Steiner, A. W., J. M. Lattimer, and E. F. Brown (2013). The Neutron Star Mass-Radius Relation and the Equation of State of Dense Matter. *ApJ*, **765**, L5. doi:10.1088/2041-8205/765/1/L5.

Stergioulas, N. and J. L. Friedman (1995). Comparing models of rapidly rotating relativistic stars constructed by two numerical methods. *ApJ*, **444**, pp. 306–311. doi:10.1086/175605.

Strohmayer, T. E. (1992). Light curves of rotating, oscillating neutron stars. *ApJ*, **388**, pp. 138–147. doi:10.1086/171136.

Strohmayer, T. E., W. Zhang, J. H. Swank, A. Smale, L. Titarchuk, C. Day, and U. Lee (1996). Millisecond X-Ray Variability from an Accreting Neutron Star System. *ApJ*, **469**, p. L9. doi:10.1086/310261.

Sturrock, P. A. (1971). A Model of Pulsars. *ApJ*, **164**, p. 529. doi:10.1086/150865.

Suleimanov, V., J. Poutanen, M. Revnivtsev, and K. Werner (2011). A Neutron Star Stiff Equation of State Derived from Cooling Phases of the X-Ray Burster 4U 1724-307. *ApJ*, **742**, 122. doi:10.1088/0004-637X/742/2/122.

Suleimanov, V., J. Poutanen, and K. Werner (2012). X-ray bursting neutron star atmosphere models using an exact relativistic kinetic equation for Compton scattering. *A&A*, **545**, A120. doi:10.1051/0004-6361/201219480.

Urbanec, M., J. C. Miller, and Z. Stuchlík (2013). Quadrupole moments of rotating neutron stars and strange stars. *MNRAS*, **433**, pp. 1903–1909. doi:10.1093/mnras/stt858.

van Paradijs, J. (1978). Average properties of X-ray burst sources. *Nature*, **274**, pp. 650–653. doi:10.1038/274650a0.

van Paradijs, J. (1979). Possible observational constraints on the mass-radius relation of neutron stars. *ApJ*, **234**, pp. 609–611. doi:10.1086/157535.

Watts, A. L. (2012). Thermonuclear Burst Oscillations. *ARA&A*, **50**, pp. 609–640. doi:10.1146/annurev-astro-040312-132617.

Webb, N. A. and D. Barret (2007). Constraining the Equation of State of Supranuclear Dense Matter from XMM-Newton Observations of Neutron Stars in Globular Clusters. *ApJ*, **671**, pp. 727–733. doi:10.1086/522877.

Yagi, K. and N. Yunes (2013a). I-Love-Q relations in neutron stars and their applications to astrophysics, gravitational waves, and fundamental physics. *Phys. Rev. D*, **88**(2), 023009. doi:10.1103/PhysRevD.88.023009.

Yagi, K. and N. Yunes (2013b). I-Love-Q: Unexpected Universal Relations for Neutron Stars and Quark Stars. *Science*, **341**, pp. 365–368. doi:10.1126/science. 1236462.